Department of Civil, Chemical and Environmental Engineering
University of Genova, Italy

Flow control using a porous, compliant coating of feather-like actuators

A thesis submitted to the University of Genova for the degree of

DOCTOR OF PHILOSOPHY

by

Divya Venkataraman

February 2013

Università degli Studi di Genova
Dipartimento di Ingegneria del Civile, Chimica e Ambientale

Dottorato di ricerca in
Fluidodinamica e Processi dell'Ingegneria Ambientale
XXIV CICLO

Flow control using a porous, compliant coating of feather-like actuators

Divya Venkataraman

Supervisors:

Prof. Alessandro Bottaro - Università degli Studi di Genova

Prof. Rama Govindarajan - Tata Institute of Fundamental Research, Hyderabad, INDIA

Reviewer:

Prof. Emmanuel de Langre - LadHyX, Ecole Polytechnique, Palaiseau, FRANCE

University of Genova
Department of Civil, Chemical and Environmental Engineering
Doctor of Philosophy in Fluid dynamics & Processes of Environmental Engineering
XXIV Cycle

Coordinator:
Prof. Giovanna Vittori - Università degli Studi di Genova

Jury:
Prof. Rodolfo Repetto - Università degli Studi di Genova
Prof. Giorgio Rovero - Politecnico di Torino, Italy
Prof. Markus Uhlmann - Institut fr Hydromechanik, Germany
Prof. Marco Colombini - Università degli Studi di Genova
Prof. Luca Fiori - Università degli Studi di Trento, Italy

Final presentation:
March 19, 2013

Divya Venkataraman
Dipartimento di Ingegneria del Civile, Chimica e Ambientale
Universita degli Studi di Genova, via Montallegro 1
16145 Genova - Italia

Phone: +39 010 353 2560
E-mail: divya@dicat.unige.it

Abstract

A passive actuation technique, that entails covering the suction side of an aerofoil with a poro-elastic carpet, is investigated in this thesis. This technique is inspired from the covert or pop-up feathers used by some birds during landing and perching manoeuvres. In the first part of this thesis, numerical modeling of the coupled fluid-structure interaction problem is performed for a low Reynolds number regime, characteristic of micro aerial vehicles. The immersed boundary technique is employed, which offers the advantage of using Cartesian grids for complex geometries. By suitably selecting the characteristics of the carpet, to synchronise characteristic time scales of the fluid and the structural systems, significant drag reduction and/or lift enhancement can be achieved, associated with modifications of the length scales of the shed vortices and a mild intensification of their intensity. A parametric analysis shows that such a coating is able to affect the topology of the flow in the proximity of the rear of the aerofoil, by adapting spontaneously to the separated flow.

In the second part of this thesis, reduced order models are obtained for vortex-shedding, both from a smooth aerofoil as well as from an aerofoil coated with the feather-like actuators, based on the computations performed in the first part of this thesis. The models, derived using perturbation techniques, aid in our understanding of the physics of the fluid-structure interaction problem in the presence of such a poro-elastic coating. The reduced order models indicate the presence of distinct regimes that are dependent on the flow and coating characteristics. Besides, the outputs from these models are found to be capable of reconciling with the computational results, hence highlighting the advantages of using reduced-order models. In addition, results from prototype simulations for “simpler” flows (such as the flow over a flat plate with such a poro-elastic coating) are seen to relate with the results yielded by the reduced-order models. The models and the parameter studies performed thus provide insight into the selection of optimal coating parameters to enable flow control at low Reynolds numbers.

Acknowledgments

I am greatly indebted to a number of people for their help and support during the course of this research, and would like to express my gratitude toward all of them.

First, a very special acknowledgment goes to Professor Alessandro Bottaro who was a perfect supervisor during these four years, irrespective of whether I was in Genova or in India. His guidance, enthusiasm, encouragement and helpful nature have motivated me through all these years. His wide knowledge, consistent availability and patience have helped me in many ways in taking this work towards its objectives. I also wish to thank Professor Rama Govindarajan, who always ensured a very enriching atmosphere for research during the stay period in India for this collaborative Ph.D work. Her interesting suggestions were crucial in shaping the present work.

I wish to thank Dr. Julien Favier, for help with his flow solver code, and Dr. Joel Guerrero, for help with validation of simulation results. I would also like to thank the other members of my Ph.D committee and faculty at *DICCA*, (including but not limited to) Professors Giovanna Vittori, Paolo Blondeaux, Jan Pralits and Rodolfo Repetto, for their valuable feedback (particularly in the form of stimulating questions at the time of presentations) from time to time during the course of this research. I also take the opportunity here to thank Professors Paolo Blondeaux and Giovanni Besio for introducing me to the exciting area of perturbation methods and their applications to fluid mechanics, which has helped me tremendously in shaping a sizeable part of the work in this thesis.

I gratefully acknowledge the technical and administrative assistance provided by the staff at *DICCA*, *JNCASR* - Bangalore and *TIFR* - Hyderabad. I also thank all my colleagues/friends, both past and present, at all these places, for useful and interesting discussions as well as assistance, incidentally not always restricted to “technical” issues. This list is very long and can perhaps eternally go on, and so had to be deliberately left out !

I can not end without expressing my gratitude to my family and very close relatives, for their continued and unconditional support over the years. Without their encouragement, patience and guidance (in conceivably every possible form), this work would definitely not have been possible.

This research was financially supported by the University of Genova, Italy; the Jawaharlal Nehru Centre for Advanced Scientific Research (JNCASR), Bangalore, India; and the Tata Institute of Fundamental Research (TIFR), Hyderabad, India.

Contents

1 Passive flow control actuators and their applications 1

1.1 UAVs and MAVs 2

1.1.1 Unmanned aerial vehicles 2

1.1.2 Micro aerial vehicles 3

1.2 Flight in nature 4

1.3 Aerodynamics at low Reynolds numbers 6

1.4 Applications to flight technology 7

1.4.1 MAVs and UAVs 7

1.4.2 Conventional aircraft 8

1.5 Other applications 8

1.5.1 Wind-crop interaction and plant growth 8

1.5.2 Aerodynamics of sports balls 9

1.6 Overview of research: self-actuating movable flaps 10

1.7 Practical implementation of the control 12

1.8 Connections with non-linear dynamics 13

1.9 Organization 15

2 Numerical model for a coated aerofoil **17**

2.1 Background of the IB method 19

2.2 Boundary conditions on immersed bodies 19

2.3 Physical model & computational method for aerofoil 22

2.3.1 Fluid domain equations 22

2.3.2 Tuning of the IB parameters 24

2.3.3 Numerical resolution 25

2.4 Numerical convergence of the fluid model 27

2.5 Validity of boundary conditions 28

2.6 Validation of numerical method 29

2.7 Feather layer model 29

2.7.1 Coupling between fluid and structure 31

2.7.2 Dynamics of the compliant coating 33

2.7.3 Numerical resolution of the structure model 36

2.8 Summary of the two-way coupling 36

3 Simulation results: Flow control with coated aerofoils **39**

3.1 Aerofoil without control 39

3.2 Investigation of the control parameters 42

3.3 Aerofoil with control 45

3.4 Physical interpretation of the control 47

3.4.1 *Parametric study* 47

3.4.2 *Frequencies observed in the fluid-structure coupled system* 51

3.4.3 *Changes in flow field close to the aerofoil* 53

3.5 Conclusions 55

4 Reduced order model for vortex-shedding from smooth aerofoil 57

4.1 Characteristics of limit cycles 58

4.2 Characteristics of vortex-shedding from aerofoil 59

4.3 Development of reduced-order model 60

4.3.1 Condition for existence of Hopf bifurcations 60

4.3.2 Application to the case of vortex-shedding 63

4.4 Derivation of model parameters 66

4.4.1 Solution by the method of multiple scales 66

4.4.2 Model parameters from simulation results 71

4.4.3 Requirement of cubic or higher odd-order non-linearities 72

4.5 Comparison with simulation results 72

4.6 Parameter regimes for existence of limit cycles 76

4.7 Conclusions 79

5 Coupled reduced order model for aerofoil with poro-elastic coating 81

5.1 Linear reduced-order model with linear coupling: derivation of solution . . . 82

5.2 Structure and coupling parameters from simulation results 89

5.3 Overview of simulations 90

5.3.1 Prototype simulations: Case of flat plate 90

5.3.2 Case of symmetric aerofoil 102

5.4 Comparison with simulation results 107

5.5 Conclusions 113

6 Summary and Conclusions 115

6.1 Conclusions 116

6.1.1 Numerical modeling of flow control via a porous, compliant coating . 116

6.1.2 Reduced-order modeling for laminar flow control via a porous coating of compliant actuators 117

6.2 Thesis Contributions 117

6.3 Some Directions for Future Work 118

References 121

List of Figures

1.1 Left: Wasp III Small Unmanned Aircraft System, a small remote-controlled UAV that is powered by rechargeable lithium ion batteries and has a wingspan of 72.3 cm, empty weight of 430 g, range of 5 km and maximum speed of 65 kmph (Source - http://en.wikipedia.org/wiki/AeroVironment_Wasp_III). Right: RQ-4 Global Hawk, a “High Altitude Long Endurance”(HALE) conventional UAV that can fly as a surveillance aircraft at an altitude of approximately 19-20 km and at a speed of approximately 560 kmph. (Source - http://en.wikipedia.org/wiki/Northrop_Grumman_RQ-4_Global_Hawk). . . . 3

1.2 Left: The Delfly Micro, a very small remote-controlled aircraft with camera, weighing just 3 grams and measuring 10 cm (Source - http://www.delfly.nl/?site=DIII&menu=home&lang=en, website of Delfly project, TU Delft). Right: The dragonfly *Yellow-winged Darter*, inspiration behind the Delfly Micro (Source - http://en.wikipedia.org/wiki/Dragonfly). 4

1.3 Raising of coverts on birds wings, seen during landing or gliding. Left: Lesser underwing coverts fully deflected (red arrow) during a gliding perching sequence [5]. Right: Raising of compliant coverts on the wing of a Skua (Source - http://www.bionik.tu-berlin.de, website of Bionik group of Prof. I. Rechenberg, TU Berlin). 5

1.4 Dependence of the maximal lift (left) and the minimal drag (right), in terms of normalised coefficients, on Reynolds number for smooth fixed aerofoils [6]. 6

1.5 Differences between flow in a boundary layer (left panels) and in a canopy layer (right panels). Top panels: Wind profile and eddy structure; bottom panels: Spectrum of oscillations of the streamwise velocity [12]. 9

1.6 Comparison of drag dependence on Reynolds number for a golf ball and spheres coated with sand grains, where k is the height of roughness of the sand-grain and d is the ball diameter [14]. 10

1.7 Left: Lower half of a T-shirt printed using flocking technique; Right: Schematic of the flocking process - 1, 2 and 3 stand for the flock, the glue and the substrate respectively. (Source - http://en.wikipedia.org/wiki/Flocking_(texture)). 12

2.1 Schematic diagram of the computational domain showing the three boundaries immersed in the fluid in movement - solid aerofoil, compliant coating and buffer zone. 22

2.2 (a) Distribution of grid points over the whole computational domain; only one in every 10 lines is shown; the aerofoil is at the domain's centre, at the intersection of the horizontal and vertical black bands. (b) Detail of the grid in the vicinity of the aerofoil. 27

2.3 Spatial convergence of fluid solver. (a) Mean lift (bottom) and mean drag (top) coefficients as functions of domain size (in units of D^2), with mesh size fixed to 700x500. (b) Mean lift coefficient, together with the instantaneous maximum and minimum values during an oscillation cycle, as functions of the total number of grid points for a domain size fixed to 50Dx50D. 28

2.4 Comparison of the Fourier spectra of the drag coefficient (blue curve) with that of the inlet streamwise velocity (red curve), for the NACA0012 aerofoil at an angle of incidence of 22°. 29

2.5 Comparison of time-averaged values of lift coefficients for the NACA0012 aerofoil at various angles of attack, obtained from the fluid solver. 30

2.6 Comparison of the Fourier spectra of lift coefficients for the NACA0012 aerofoil at 10° angle of attack - the blue curve is from present computations while the red curve is obtained from FLUENT 30

2.7 Feather layer model. (a) Homogenized approach; the thickest lines are the reference beams, each of them being surrounded by control volumes. The position and velocity of individual elements in a control volume (shown by thin lines) is interpolated from the position and velocity of the reference beams. (b) Representation of the variable porosity (in terms of the packing density variable) and anisotropy (in terms of the orientation vector) of the layer - a darker shade stands for higher packing density. 31

2.8 Moments in the structure model. 34

2.9 Weakly-coupled algorithm for two-way fluid-structure interaction. 37

3.1 Dependence of the dimensionless coefficients of (a) time-averaged drag and (b) time-averaged lift, as the angle of attack of a static NACA0012 aerofoil is varied from 20° to 70°. The thick curves represent the mean values of drag and lift, while the dotted curves above and below these thick curves represent the maximum and minimum values of the instantaneous drag and lift coefficients in the course of the oscillations, respectively. 40

3.2 Time evolution of the drag (left) and lift (right) coefficients for angles of incidence equal to 22° (top), 45° (middle) and 70° (bottom). 41

3.3 Power spectra of the drag (left) and lift (right) signals for angles of attack equal to 22° (top), 45° (middle) and 70° (bottom), corresponding to the time signals shown in figure 3.2. Non-dimensional frequency is plotted along the horizontal axes. 43

3.4 Time evolution of the drag (left) and lift (right) coefficients for an aerofoil at angles of attack 22° (top), 45° (middle) and 70° (bottom) - comparison between the cases of aerofoil without control (solid, black lines) and aerofoil with control (blue, dashed lines). 48

3.5 Dependence of drag on structure frequency (determined by the rigidity moment K_r) for (a) 45°, and (b) 70°. The structure frequencies are selected to match frequencies observed in the flow. The thick curves represent the mean values of drag, while the dotted curves above and below these thick curves represent the maximum and minimum values of the instantaneous drag coefficients in the course of the oscillations. The arrows point to the optimum cases shown in figure 3.4. In each of these cases, the values of minimum, mean and maximum drag for the reference case (i.e. under uncontrolled conditions) is shown by the black vertical line with cyan dots on the extreme left. 49

3.6 Dependence of lift as the packing density ϕ is varied over an admissible range (in accordance with Howells (1998)) for (a) 22°, (b) 45°, and (c) 70°. The thick curves represent the mean values of lift, while the dotted curves above and below these thick curves represent the maximum and minimum values of the instantaneous lift coefficients in the course of the oscillations. The arrows point to the cases shown in figure 3.4. In each of these cases, the values of minimum, mean and maximum lift for the reference case (i.e. under uncontrolled conditions) is shown by the black vertical line with cyan dots on the extreme left. 50

3.7 Power spectra of the drag (left) and lift (right) signals for incidence angles equal to 22° (top), 45° (middle) and 70° (bottom) when the poro-elastic, compliant coating is used, corresponding to the time signals shown in figure 3.4 (blue, dashed lines). Non-dimensional frequency is plotted along the horizontal axes. 52

3.8 Time-averaged pressure field, depicted by isolines and colour plot for angles of attack equal to 45° (top) and 70° (bottom). The panel on the left-hand side shows the pressure field for a smooth aerofoil while that on the right-hand side is for a coated aerofoil. 53

3.9 Colour plot of instantaneous vorticity field for angles of attack equal to 22° (top) and 70° (bottom). Left-hand side and right-hand side panels depict uncontrolled and controlled cases respectively. It is interesting to note that, in the presence of the coating, the shed vortices are more closely spaced than in the corresponding uncontrolled cases. 54

4.1 Colour plot of instantaneous vortex pattern from an aerofoil at an incidence of 10°. 59

4.2 Time evolution of lift coefficient (left); Fourier spectrum of lift coefficient (right). 60

4.3 Limit cycles for cases 3 (blue curve) and 6 (red curve) of Table 4.1. The left sub-figure considers an initial condition lying within both the limit cycles, while the right sub-figure considers an initial condition lying outside both the limit cycles. 66

4.4 Comparison of model and simulation results of lift coefficient - the blue curve shows the simulation results while the red curve shows results from the model. The top and bottom sub-figures show comparisons in time and frequency domains respectively. 73

4.5 Convergence of numerical integration of the model equation from an initial condition **outside** the limit cycle. The top and bottom sub-figures show the time trace and the phase portrait, respectively. 74

4.6 Convergence of numerical integration of the model equation from an initial condition **inside** the limit cycle. The top and bottom sub-figures show the time trace and the phase portrait, respectively. 75

4.7 Dependence of the amplitude of limit cycle a_1 on the linear and cubic damping parameters, μ and α respectively, as given by equation (4.34), when the coefficient of restoring force ω is fixed to the value 5.8039 (as given by equation (4.43)). The star shows the parameters at which the reduced-order model yields the solution that matches with the computational results, as shown in figure 4.4. 76

4.8 Dependence of the frequency of limit cycle ω_s on the damping parameters when the coefficient of restoring force ω is fixed to the value given by equation (4.43). The top, middle and bottom panels show the dependence of ω_s on the linear and cubic damping coefficients μ and α, linear and quadratic damping coefficients μ and β, and, cubic and quadratic damping coefficients α and β, respectively, when β, α and μ are fixed to the values given by equation (4.43), in each of the cases. 78

5.1 Placement of the poro-elastic layer on the horizontal flat plate, depicted by the reference feathers (shown here by the horizontal, black lines towards the end of the top side of the flat plate). 91

5.2 Comparison of the time evolutions of the streamwise velocity for the horizontal flat plate without (black, dotted lines) and with (blue, solid lines) a poro-elastic coating on its top side (as shown in figure 5.1), at four streamwise locations over the flat plate and in its near wake, going from left to right. . . 92

5.3 Snapshots showing the time evolution of streamlines close to the coated flat plate, as shown by the schematic in figure 5.1. These four time instants are selected uniformly over one cycle of the time signal of lift coefficient. 93

5.4 Colour plot of instantaneous vortex-shedding from the poro-elastically coated horizontal flat plate, shown in figure 5.1. 94

5.5 (Top) Time evolution of the lift coefficient for the horizontal flat plate with a poro-elastic coating on its top side (as shown in figure 5.1); (bottom) Fourier spectrum of the lift coefficient shown in the top sub-figure. 95

5.6 (Top) Time evolution of the angular displacement of the reference feathers, corresponding to the case shown in figure 5.5. The blue curve shows the dynamics of cilium 1 while the black curve shows the dynamics of cilia 2, 3, and 4 (as shown in figure 5.1), all of which are seen to be identical; (bottom) Fourier spectrum of the angular displacement of cilium 1. 96

5.7 Comparison of the time evolutions of the streamwise velocity for the flat plate at an incidence of 10° without (black, dotted lines) and with (blue, solid lines) a poro-elastic coating over the end of its top side, at four streamwise locations over the flat plate and in its near wake, going from left to right. 98

5.8 (Top) Comparison of the time evolutions of the lift coefficient for the flat plate at an incidence of 10° without (black curve), and with (blue curve), a poro-elastic coating over the end of its top side; (bottom) comparison of the Fourier spectra of the lift coefficients shown in the top sub-figure - the colour codes are same as for the top sub-figure. 99

5.9 Comparison of the limit cycles for the lift coefficient for the flat plate at an incidence of 10° without (black curve), and with (blue curve), a poro-elastic coating over the end of its top side. 100

5.10 (Top) Time evolution of the angular displacement of the reference feathers, corresponding to the case shown in figure 5.8. The black, blue, red and pink curves show the dynamics of cilium 1, 2, 3 and 4, respectively; (bottom) Fourier spectra of the angular displacement of the reference feathers, shown in the top sub-figure - the colour codes are same as for the top sub-figure. . . 101

5.11 Comparison of the limit cycles for the lift coefficient for the aerofoil at an incidence of 10° without (black curve), and with (blue curve), a poro-elastic coating on its top side. 102

5.12 Time evolution of the lift coefficient for aerofoil at 10° angle of attack, with poro-elastic coating where the rigidity frequency ω_r is set equal to half the frequency of vortex-shedding, as shown in figure 4.2 (b). This figure shows three cases of placements of the poro-elastic layer on the suction side of the aerofoil: (a) last 30% of the suction side (green); (b) first 70% of the suction side (blue); and (c) first 50% of the suction side. 103

5.13 Fourier decomposition corresponding to the time signals shown in figure 5.12. This figure plots the amplitudes of the fundamental frequency and its super-harmonics for the coupled fluid-structure system. 104

5.14 Time evolution of the angular displacement of a reference feather near to the middle of the suction side for the cases shown in figure 5.12. 105

5.15 Fourier decomposition corresponding to the time signals shown in figure 5.14. 106

5.16 Time evolution of the angular displacement of a reference feather nearest to the trailing edge for the cases shown in figure 5.12. 106

5.17 Fourier decomposition corresponding to the time signals shown in figure 5.16. 107

5.18 Placement of the poro-elastic layer on the aerofoil, depicted by the position of the reference feathers (shown here by the thick, black lines near the leading edge of the aerofoil). 108

5.19 Colour plot of instantaneous vortex-shedding from a poro-elastically coated aerofoil at an incidence of 10°. 108

5.20 Comparison of model and simulation results of lift coefficient - the blue curve shows the simulation results while the red curve shows results from the model. 110

5.21 Convergence of numerical integration of the model equation from an initial condition **outside** the limit cycle. The top and bottom sub-figures show the time trace and the phase portrait, respectively. 111

5.22 Convergence of numerical integration of the model equation from an initial condition **inside** the limit cycle. The top and bottom sub-figures show the time trace and the phase portrait, respectively. 112

List of Tables

3.1 Parameters which have been varied in the course of the parametric search; the values provided here are those which guarantee the best control results. The normalization of the structure moments and the flow frequency is done w.r.t the mass of the reference beam M, half the length of the reference beam l_c and the time scale of the free-stream, which is the ratio between the aerofoil chord length D and the free-stream speed u_∞. 46

3.2 Parameters fixed throughout the course of the study. Here, length and diameter of a reference beam are non-dimensionalized w.r.t the aerofoil chord length D. 46

4.1 Dependence of limit cycle existence on the non-linearities in equation (4.1). . 65

Chapter 1

Passive flow control actuators and their applications

Introduction

The desire of mankind to venture into territories outside the “usual” terrestrial limits, for instance into the skies or within deep waters, can almost unambiguously be attributed as the prime motivation for designing mechanisms resembling those found in nature. Much later in human history, when locomotion outside the limitations of land slowly began to be perceived as a necessity than just a means of recreation, it was natural for man to start observing movement of flying or swimming creatures more minutely, and trying to see up to what extent they can be mimicked. It is thus not surprising that optimization of flight performance, by manipulating fluid flows, has been a very active research area for a number of years now.

In the last half century, when exploitation of nature and its resources has been progressively becoming a global concern, the focus of flight optimization can be particularly seen as instances of optimization of fuel use in commercial air transport, achieved by decreasing the drag and/or increasing the mean lift, delaying stall, noise reduction and/or even influencing the transition to turbulence [1]. Apart from the immediate implications of flight optimization in the commercial arena, these goals are also sought while designing unmanned aerial vehicles (UAVs) and micro aerial vehicles (MAVs). These are essentially aircraft, some of which are very small, that, owing to their design suitability, can accomplish several tasks that human-operated aircraft can not perform. These tasks are often referred to as 3-D ("dull, dirty and dangerous"). This chapter presents an aspect of mimicking flight in nature that has been applied extensively in various areas of human endeavour.

1.1 UAVs and MAVs

In this section, an introduction is given about UAVs and MAVs, their prime attributes and limitations, their applications and finally advantages of employing these, for specific missions.

1.1.1 Unmanned aerial vehicles

UAVs, or unmanned aerial vehicles, as the name suggests, are aircrafts without human pilots on board. Their flight is either controlled autonomously by computers in the vehicle, or under the remote control of a navigator, a pilot on the ground or in another vehicle. Historically, UAVs were simple aircraft controlled by pilots remotely, but autonomous control is being used over the recent past. They can typically travel at altitudes of around 600m with a range of up to 5 km (Wasp III), up to as high altitudes as 15-20 km and range of over 200 km (RQ-4 Global Hawk) (cf. figure 1.1).
UAVs are primarily deputed for military applications such as providing targets simulating enemy aircrafts and missiles to aerial and ground gunnery, battlefield intelligence, capability for high-risk combats. However, increasingly civil applications, such as firefighting and monitoring of pipelines, cargo transport and UAV-related research and development activities, are also coming under its purview.

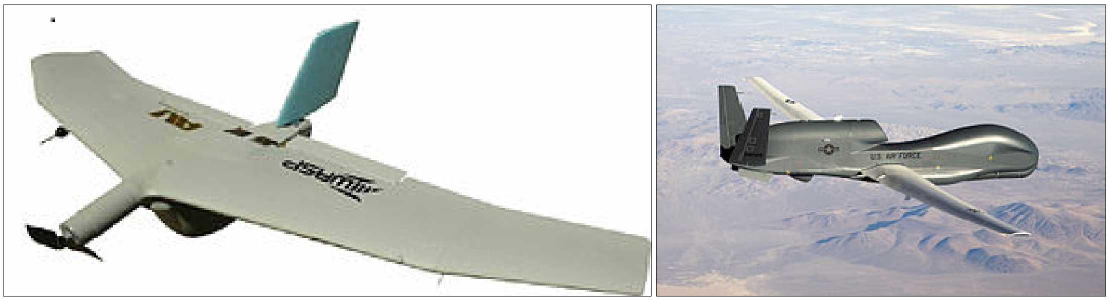

Figure 1.1: Left: Wasp III Small Unmanned Aircraft System, a small remote-controlled UAV that is powered by rechargeable lithium ion batteries and has a wingspan of 72.3 cm, empty weight of 430 g, range of 5 km and maximum speed of 65 kmph (Source - http://en.wikipedia.org/wiki/AeroVironment_Wasp_III). Right: RQ-4 Global Hawk, a “High Altitude Long Endurance”(HALE) conventional UAV that can fly as a surveillance aircraft at an altitude of approximately 19-20 km and at a speed of approximately 560 kmph. (Source - http://en.wikipedia.org/wiki/Northrop_Grumman_RQ-4_Global_Hawk).

1.1.2 Micro aerial vehicles

MAVs are a class of UAVs, that have a size restriction whose operation may not involve human intervention at all. Very recent MAVs can typically have wingspans as less as 15 centimetres and weights of just 100 g, with a payload consisting of a camera or some sensors, weighing only 20 g. MAVs can typically fly at low altitudes of around 100m, at a cruise speed of 50 kmph for 30-60 minutes. Research in MAV development is motivated by commercial as well as military purposes, with insect-sized aircraft reported recently, an example being the Delfly Micro that measures 10 cm and weighs 3 grams, which thus compares with the dimensions of a dragonfly (cf. figure 1.2).

The design of these machines became achievable in the last one-and-a-half to two decades, owing to advances in miniaturization in the areas of propulsion, aviation and electronics. MAVs are usually deputed for missions involving spying and surveillance in battlefields, rescue of hostages, fire as well as radio-activity detection, weather forecast - to name a few. However, their size limitations and other characteristics, like high manoeuvrability, high efficiency, and noise reduction, impose certain restrictions on their design. Some of these include the requirement of anti-collision detection systems and real-time data acquisition

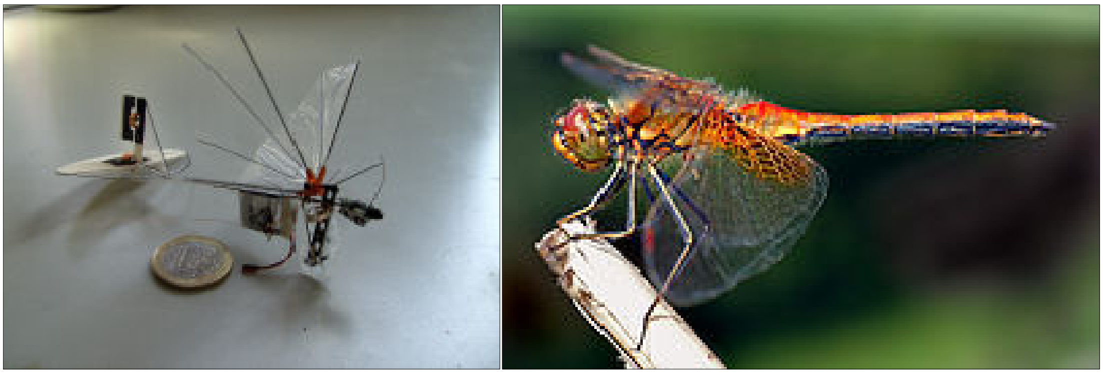

Figure 1.2: Left: The Delfly Micro, a very small remote-controlled aircraft with camera, weighing just 3 grams and measuring 10 cm (Source - http://www.delfly.nl/?site=DIII&menu=home&lang=en, website of Delfly project, TU Delft). Right: The dragonfly *Yellow-winged Darter*, inspiration behind the Delfly Micro (Source - http://en.wikipedia.org/wiki/Dragonfly).

systems to avoid easy detection, due to low-altitude and slow-speed cruising capabilities. All of these characteristics have immediate applications to various problems that can be tackled [2]. For instance, high manoeuvrability, like in insect flight, is desirable in applications like earthquake search-and-rescue operations or exploring a radioactivity-contaminated building. Issues like trade-off between size limitations and high efficiency becomes pertinent in the design of light MAVs with acceptable lifetimes powered by batteries. Finally, noise reduction is important in military operations, to ward off the threat of being detected by enemy detection systems. It must also be noted that good MAVs need not be necessarily obtained by reducing the dimensions of a good airplane. An important reason behind this fact is that the aerodynamics for small Reynolds numbers, at which MAVs usually operate, is qualitatively different from large Reynolds number aerodynamics for airplanes.

1.2 Flight in nature

Considering the amount of innovation that goes behind all these technological advances, it is particularly worthwhile to analyse and emulate efficient flying mechanisms observed in nature, in the form of birds and insects. These mechanisms smartly optimize unsteady aerodynamics to their advantage [3,4], having evolved and adapted over millions of years, and having stood the test of time. Further, these flight systems are particularly suitable for low Reynolds numbers, and even at very small length scales can offset the shortcomings of flows in these regimes. Finally, at these length scales, power supplies from biological constructs like muscles seem to be more robust compared to any engineered system vis-a-vis aspects such as weight and energy efficiency. Some of these mechanisms have already been applied in recent aircraft systems, such as vortex generators and slats/flaps on the leading edge, while many several other mechanisms and the physics associated with them are yet to be fully understood. It must however be noted that analysing which natural systems are most efficient need not necessarily yield a better understanding of effective biomimetics, because evolution is mostly perceived to progress in a non-linear manner.

Passive flow control : One such noteworthy instance of optimisation technique observed in nature is that of covert feathers over the wings of some birds, which “pop-up”automatically from the wings when the birds experience a drop in their flying abilities. This happens particularly during landing or gliding phases, when a high angle of attack is needed to produce sufficient aerodynamic lift (cf. figure 1.3). As an example, for perching manoeuvre during landing, there is evidence of coverts popping up and vibrating when birds employ high angles of attack.

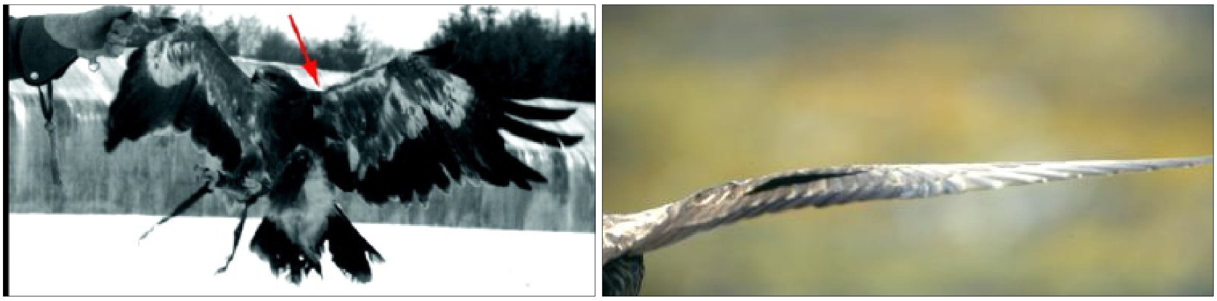

Figure 1.3: Raising of coverts on birds wings, seen during landing or gliding. Left: Lesser underwing coverts fully deflected (red arrow) during a gliding perching sequence [5]. Right: Raising of compliant coverts on the wing of a Skua (Source - http://www.bionik.tu-berlin.de, website of Bionik group of Prof. I. Rechenberg, TU Berlin).

These feathers, or passive actuators, adapt their movement to the local, instantaneous flow and control many undesirable physical phenomena that lead to a decrease in the aerodynamic performance. This has interesting applications for MAVs that operate at high angles of attack, though the Reynolds number regimes are much lower.

1.3 Aerodynamics at low Reynolds numbers

An interesting aspect of flight observed in nature is that it spans a wide range of chord-Reynolds numbers, starting from as low as about 1000 - for insects like houseflies or mosquitoes - to around 50,000 or more - for birds like eagles. The key to effectively implementing the envisaged passive controls on aerodynamic configurations, thus highly depends on the understanding of the physics occurring across this wide spectrum of Reynolds numbers. For example, in the low Reynolds number regime, of the order of 1000, viscous forces are very significant. As a consequence, there is increased drag, reduced lift-to-drag ratios and hence reduced propelling efficiency, in contrast to higher Reynolds numbers cases, such as in a conventional aircraft. This fact can be seen from the work of McMasters and Henderson [6], where the results on the variation of lift and drag for fixed aerofoils for a large Reynolds number range are presented (cf. figure 1.4).

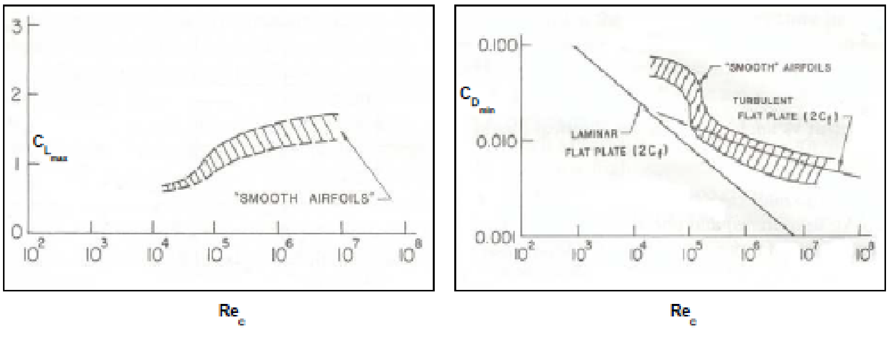

Figure 1.4: Dependence of the maximal lift (left) and the minimal drag (right), in terms of normalised coefficients, on Reynolds number for smooth fixed aerofoils [6].

Moreover, flows with low Reynolds numbers usually maintain laminarity, whereas higher

Reynolds number flows are often subject to transition to turbulence, whose prevention is itself a fluid-dynamic challenge in its own right [7,8]. One method to achieve this is by employing biomimetic rough skins to induce approximately optimal perturbations. These perturbations are capable of changing the mean velocity profiles at the highest order, owing to high amplification. It has also been found that the presence of flexible surface(s) on a body, which can excite itself into vibration, can also affect the separation and transition points of the flow.

Many natural flyers, on account of flying at relatively low Reynolds numbers, restrict themselves to maintaining laminar flow, which, in general, is less capable of handling adverse pressure gradients in the boundary layer and thus is more susceptible to separation, when compared to a turbulent boundary layer. To study the effect of covert feathers in a relatively simple set-up that is also closer to flight observed in nature, flow control in a laminar regime is considered as the scope of this thesis.

1.4 Applications to flight technology

1.4.1 MAVs and UAVs

The management of flow separation in low Reynolds number regime becomes crucial for designing MAVs and UAVs. In fact, aerodynamic and propulsion factors put severe constraints on MAVs, like narrow ranges of airspeed as well as angle of attack, rendering the vehicle more vulnerable to gust upset. Shape optimization (or morphing) techniques with the use of passive actuators or flaps, indeed seem to have the ability to generate aerodynamic forces and moments required to stabilize and manoeuvre MAVs, without penalizing their weight and energy constraints. In the recent past, the research and design of fixed-wing MAVs has focussed on low Reynolds number regimes, where a fixed wing has inferior performance compared to MAVs with flapping or rotary wings.

1.4.2 Conventional aircraft

In the design of aircraft, all of which travel at high Reynolds numbers, it is important to arrive at a trade-off between optimum lift and drag. While a larger wing is bound to yield higher lift and hence decrease the distance required for landing and take-off, it will also lead to a higher drag when the aircraft is cruising. To even out these differences and achieve optimum fuel economy (by optimising the lift-to-drag ratio), high-lift devices, such as flaps and slats, have been commonly used in aircraft design. However, these devices have to be *actively* controlled - for instance, flaps have to be lowered into the flow for extra lift. In this context, the use of movable flaps that are self-actuated can be a promising passive flow control technique. The use of such movable flaps has been experimentally tested on an aircraft with laminar wing [9].

1.5 Other applications

The study of flow past a layer of feather-like protrusions or in the presence of some roughness on aerodynamic surfaces is useful even outside the realm of aerospace and related applications. Instances of this range from studies on plant growth affected by wind-induced plant motion [10,11,12] to how some optimum roughness on the surface of sports balls can modify its performance [13].

1.5.1 Wind-crop interaction and plant growth

In the study of thick bundles of immersed vegetation and wind-exposed plants, the plant movement is coupled with the nearby fluid flow, and the movement of each individual plant, taken to be a one-dimensional oscillator, also accounts for interactions with its immediate neighbours, modeled by means of elastic contacts between the stems. The inclusion of elastic collisions between adjacent plants fundamentally modified the linear nature of the dynamics of canopy oscillations to one having non-linear characteristic, as well as its increase its resonant eigenfrequency, when it was exposed to one or more gusts of wind. These changes are believed to guard against phenomena such as stem lodging, which are known to affect the plant growth. Further, when two-way coupling is included in the model, a frequency lock-in mechanism is demonstrated, similar to vortex induced vibrations. Strong coupling has also been observed between wind and plants, by which the dynamics of wind is modified by the motion of plants (cf. figure 1.5).

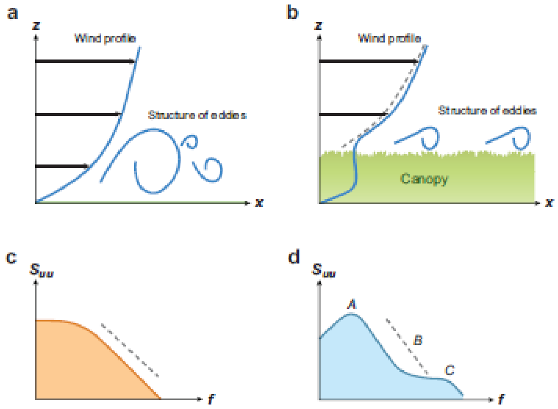

Figure 1.5: Differences between flow in a boundary layer (left panels) and in a canopy layer (right panels). Top panels: Wind profile and eddy structure; bottom panels: Spectrum of oscillations of the streamwise velocity [12].

1.5.2 Aerodynamics of sports balls

In cricket, fast bowlers swing the ball with the primary seam maintaining a small angle with the airflow. Under suitable conditions such as a prominent seam, the laminar boundary layer is bypassed by the seam into a turbulent one on one side of the ball which is kept rough, hence aiding in relatively late boundary-layer separation compared to the nonseam side which is kept polished. Such an asymmetry in boundary-layer separation results in an asymmetry in pressure distribution, producing the side force leading to the swing. Base-ball aerodynamics also follows similar principles. In the case of golf, the balls are covered with round dimples to lower the critical Reynolds number of transition to turbulence, without resulting in artificial thickening of the boundary layer (cf. figure 1.6).

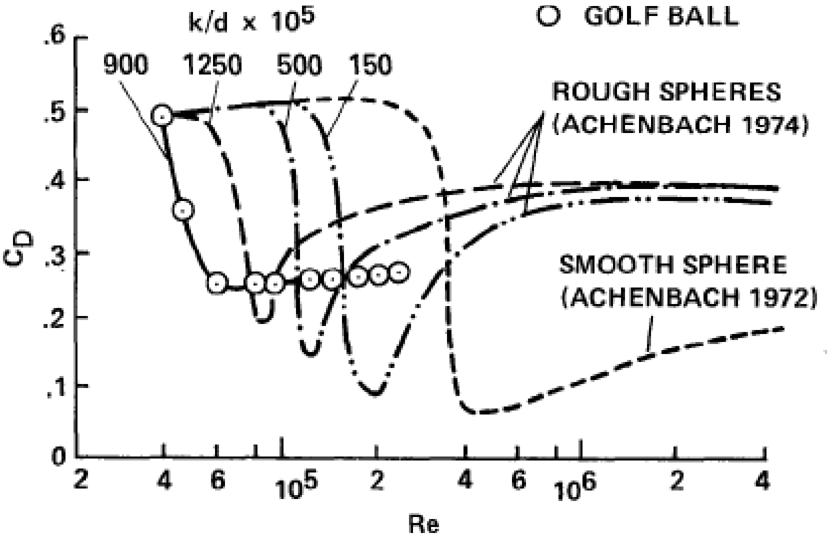

Figure 1.6: Comparison of drag dependence on Reynolds number for a golf ball and spheres coated with sand grains, where k is the height of roughness of the sand-grain and d is the ball diameter [14].

1.6 Overview of research: self-actuating movable flaps

Despite the difficulty of modern observation methods to keep an instant-by-instant account of the details of the fast motion of birds, the covert feathers are believed to control flow separation, by storing and then releasing energy in the boundary layer, according to the instantaneous fluid flow. This, in turn, is thought to affect the vortex shedding by trapping a vortex in front of the feathers, thus filling in the angle between the aerofoil and the feathers, and in turn, restricting the shed vortices to the hind part of the aerofoil [15]. Hence, there is a resultant delay in stall and a possible explanation to the efficient flight of birds under conditions of high angles of attack or in gusty winds. These feathers act as sensors to reverse flow (which is consequently followed by separation) and are activated automatically at the appropriate time. Thus, this feature of automatic activation, as opposed to active control techniques which require an energy input to come into action, provides industry with yet another reason to study ways to mimic this mechanism. Much experimental work [16,17,18,19,20] has been done in this area. For instance, a layer of such flexible structures over a given surface have been proved as feasible sensors for measuring wall shear stress in time as well as along the surface of the sensors with high resolution and accuracy. Moreover, the material used in such micro-pillars allowed these to be used as optical read-out sensors and was found to function very well over a wide range of temperature as well as have high impact strength. For SD8020 aerofoils, which are commonly used for MAV designs, use of a flap of an optimal length, near the middle of the suction side, produced almost 50% increase in lift at Reynolds numbers of around 40,000. Further, the breakdown of lift with increase in angle of attack was less drastic, when such self-activated movable flaps were used. The use of leading edge flaps was also seen to augment lift and decrease the drag at some angles greater than 20°, in addition to acting as transition devices at regimes of low Reynolds numbers. Consequently, these could prevent formation of separation bubbles and decreasing speeds at which stall occurred, during phases of manoeuvring and gliding. At higher Reynolds numbers of the order of 10^6, flaps closer to the trailing edge blocked the reverse flow from the trailing edge to peak of the suction, yielding delay in flow separation and a lift enhancement of more than 10%. It has also been shown experimentally that when surface hairs are longer as well as more closely spaced to each other, compared to those employed in sensory applications, these align with the direction of streamwise flow and induce damping in disturbances of high frequency that occur due to the passing of turbulent sweeps, and transfer of energy from smaller to larger scales. This consequently leads to streak stabilization in the streamwise direction, thus yielding turbulent drag reduction.

Computational work [21,22,23,24] has also been done simulating this behaviour - however, the Reynolds numbers at which these have been performed are typically at least one or two orders less than the regimes at which experimental work has been done. The results obtained indeed prove the effectiveness of a poroelastic coating over a surface. For instance, a substantial drop in the mean drag, lift and drag fluctuations, as well as a noteworthy increase in mean lift, has been observed [21,22,23]. Further, such a porous layer is also capable of reducing vortex-induced vibrations of certain flexible bodies by a factor of three or more [24].

1.7 Practical implementation of the control

The implementation of the envisaged control approach in UAVs and MAVs requires, for example, the use of a technique known as surface flocking, which is a process of permanently depositing many small natural or synthetic fibre particles onto a surface. The end result is a fuzzy surface that is velvety to the touch (cf. figure 1.7 (a)). Although flocking is an old technique, it was only recently realised that the process yields surfaces with excellent noise and vibration dampening qualities, leading to a wealth of applications, such as shock mounting brackets, sunroof tracks, seals and HVAC ducts. Nowadays, the flocking is usually done by the application of a high-voltage electric field. In a flocking machine, the ”flock” is given a negative charge whilst the substrate is earthed. Flock material flies vertically onto the substrate attaching to previously applied glue (cf. figure 1.7 (b)). A number of different substrates can be flocked including textiles, fabric, woven fabric, paper, PVC and other types of plastics, etc.

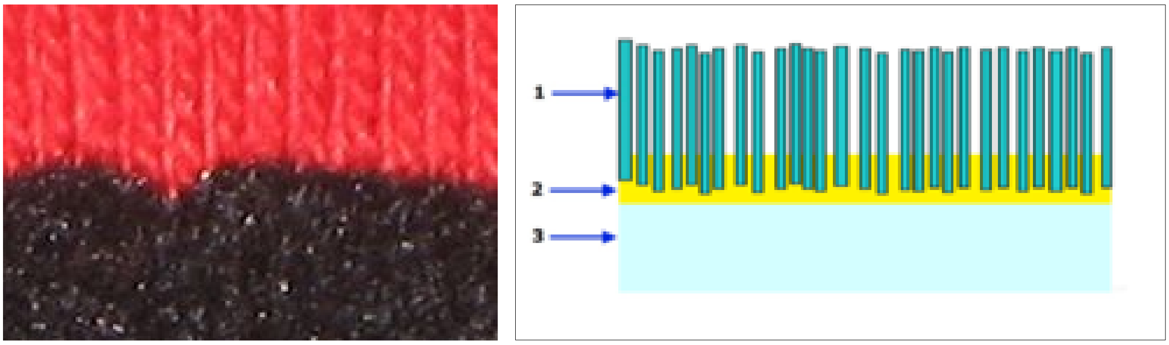

Figure 1.7: Left: Lower half of a T-shirt printed using flocking technique; Right: Schematic of the flocking process - 1, 2 and 3 stand for the flock, the glue and the substrate respectively. (Source - http://en.wikipedia.org/wiki/Flocking_(texture)).

The selection of the material constituting the flocks (its density and Young's modulus), the surface density of flocks, the flock's length and diameter, their particular placement on the surface, etc. represent parameters to be chosen appropriately, for example on the basis of Euler-Bernoulli slender beam theory. Supposing a beam/flock/fiber of cylindrical cross-section clamped on the surface at one end, and free to vibrate at the other, in the limit of large slenderness ratio s (where $s = 4h/d$, h flock length, and d flock cross-sectional diameter), i.e. for $s > 100$, the first wavenumber of vibration of the beam along its axis is $\lambda = 1.875$ [25]. The frequency of oscillation of the beam is $\omega = \lambda^2 E^{0.5}/(sh\rho^{0.5})$, with E the Young modulus (in Pascal) of individual structural elements, and ρ the density of the material forming the coating. The characteristic time scale of vibrations of the structural elements is finally given by $T_{beam} = 7.15\ h^2\rho^{0.5}/(dE^{0.5})$. To provide synchronisation of the coating and the fluid time scale, it is thus sufficient to choose the length of the flocks h, their diameter d, the density of the material ρ and its Young modulus E in such a way as to render T_{beam} comparable to the characteristic time scale of the fluid flow.

As an example, for the case of the shedding of flow structures behind an airfoil with a dominant frequency between 10 and 100 [Hz], it is appropriate to choose rubber fibres of length h of the order of one centimeter, with $h/d = 25$. In conditions of small strain the Young modulus of rubber is in the range $E = 10^7 - 10^8\ Pa$, and its density is approximately $\rho = 1100\ kg/m^3$, so that T_{beam} can vary between $1.9 - 6 \times 10^{-2}$ seconds.

1.8 Connections with non-linear dynamics

For flow over objects with blunt leading edges, such as many aerofoils (which are nothing but two-dimensional cross-sections of the wings of birds or even aeroplanes) at low Reynolds numbers at angles of attack of moderate magnitudes, the pressure gradients on their surfaces increase and lead to separated flow. This results in increase in the size of the wake and pressure losses therein, consequently resulting in the total drag being dominated by pressure drag. Hence such configurations can be considered as bluff bodies. Ever since Roshko [26] quantified the period of vortex-shedding behind a bluff body in 1955, this phenomenon has been widely investigated, both numerically as well as experimentally. Amongst all bluff bodies, the case of circular cylinder is most frequently investigated, primarily due to the simplicity in its geometry. Bishop and Hassan [27] did pioneering work to model such bluff body dynamics using a self-excited oscillator. Work in similar areas was done by many others, some of whom include Hartlen and Currie [28], Currie and Turnball [29], Skop and Griffin [30], Iwan and Blevins [31] - to name a few. The motivation behind such work was to extract reduced-order models for vortex-shedding, which could possibly also predict complex phenomena such as instabilities, vortex-induced vibrations (VIVs) and transition to turbulence. Again, the idea behind developing reduced-order models was to develop a theory for vortex-shedding and VIVs that was as *unified* as possible, from a relatively small set of time and resource-expensive computational or experimental data, especially for large real-life mechanical objects.

The basic idea behind making use of a self-excited oscillator to model vortex-shedding from a (stationary) bluff body was that for a given set of parameters - such as the Reynolds number, geometry of the body, thickness of the body or angle of incidence with the flow - the long time history of the oscillatory forces on the body are periodic and not dependent on initial conditions. Prototype self-excited oscillators include the Rayleigh and van der Pol oscillators, both of which have cubic non-linearities. These and small modifications thereof have been tested as reduced-order models for vortex-shedding behind cylinders by many authors.

Given a stationary bluff body, once the reduced-order model for vortex-shedding from it is extracted, this low-order dynamics can be coupled with some other dynamics (possibly even in a non-linear manner). This other part of dynamics can take the form of forced periodic oscillations of the body or even using flow-compliant structures on this body (as in the case of the work in this thesis), to understand the interaction between the various frequencies in the system and possibly control them by modifying the forcing.

1.9 Organization

This thesis demonstrates the effectiveness of using a passive flow control strategy (which has its roots in flight observed in nature) as outlined in §1.2, to improve aerodynamic performance of a symmetric aerofoil in a laminar flow regime. This passive actuation technique entails in covering the suction side of the aerofoil with a poro-elastic carpet. Numerical modeling of the coupled fluid-structure interaction problem is performed for a low Reynolds number regime, characteristic of micro aerial vehicles. This thesis also attempts to characterise the structural parameters that can yield optimal performance enhancement. This section presents a concise overview of the technical chapters contained in this thesis. A review of relevant literature is presented wherever necessary in the various chapters.

Chapter 2 presents the computational method to study the two-dimensional incompressible viscous unsteady flow around a symmetric aerofoil, coated with a poro-elastic layer of passive flow-compliant actuators. In order to simplify the computational study of flow over an aerofoil, the immersed boundary technique is employed, which offers the advantage of using Cartesian grids for complex geometries. Firstly, the particular formulation of the immersed boundary method used in this thesis is explained. Then, the characteristics of flow around an aerofoil, without any such coating, at angles of attack over a wide range, are studied and validated against results in literature. This is followed by an outline of the numerical procedure used to study the flow around the aerofoil *with* a poro-elastic coating, and the associated two-way fluid-structure interaction problem.

Chapter 3 presents the simulation results obtained from the numerical procedure outlined in Chapter 2. For the computations for aerofoil coated with compliant actuators, characteristics of such a carpet are selected to synchronise the characteristic time scales of the fluid and structural systems. After presenting details of this selection, modifications in flow characteristics, that can in turn be associated to changes in aerodynamic performance, have been examined. A parametric study of the major structural properties of the actuators is also presented, which helps in characterising ”optimal” structural parameters.

Chapter 4 further examines the simulation results from the previous chapter, specifically the characteristics of vortex-shedding. These properties are analysed both in the time and Fourier domains, to extract a reduced-order model for this phenomenon. The various parameters in this model are appropriately selected so that the results from this model match well with the computational results.

Next, to optimise the aerodynamic performance, the reduced-order model for the same aerofoil coated with a poro-elastic layer of compliant actuators, is obtained in Chapter 5. From this, an attempt is made to characterise what structure parameters should, as well as, should not be used for this passive flow control technique.

Chapter 6 lists the conclusions derived from the technical results in this thesis, and outlines perspectives and recommendations for improvements in future.

Chapter 2

Numerical model for a coated aerofoil

Introduction

In this chapter, the numerical procedure to study the two-dimensional incompressible viscous unsteady flow around a NACA0012 aerofoil, coated with a poro-elastic layer of flow-compliant actuators, is presented. Numerical modeling of the coupled fluid-structure interaction problem is performed for a low Reynolds number regime, characteristic of micro aerial vehicles. The immersed boundary method (referred to as IB method henceforth) is employed, which offers the advantage of using Cartesian grids for complex geometries. To begin with, characteristics of the flow around an aerofoil, without any coating of compliant feathers (henceforth referred to as “smooth”), at angles of attack over a wide range, is studied, and validated against results in literature. This is followed by an outline of the numerical procedure used to study the flow around the same aerofoil that is covered on the suction side with a poro-elastic carpet. The use of IB method is again very convenient to numerically capture the dynamics of the compliant feathers in the poro-elastic carpet, as against the conventional approaches of using dynamic structured or unstructured grids.

After giving a brief background of the IB method, its advantages over other approaches employing grids that possibly change with time, is outlined in section 2.1. In section 2.2, the particular IB method used in this thesis is described, accompanied by its physical motivation. This is followed by a description of the numerical procedure, convergence, correctness of boundary conditions and validation for a smooth aerofoil in sections 2.3, 2.4, 2.5 and 2.6 respectively. Section 2.7 presents the procedure for the two-way interaction between the fluid and structure systems, and the resulting dynamics of the structure system.

A homogenized model of feather coating is considered, as described in §2.7.1. The coating has the following key features which emulate the important properties of birds' feathers:

(i) Porosity: the fluid can flow through the layer of feathers.

(ii) Anisotropy: the fluid is oriented along a specific direction as it enters the layer.

(iii) Compliance: the layer can deform and adapt to the surrounding flow.

It should be noted that the design considerations of such passive actuators should also take into account the basic premise that these control elements, when not in use (or in situations of low or moderate angles of attack), should not have any negative impact on the quality of the flow past the aerofoil.

Here, the shape adaptation abilities of this porous, compliant coating is tested numerically in two dimensions and interpreted for separated flow on a symmetric aerofoil at a chord-based Reynolds number Re equal to 1100. The numerical method is based on Favier et al. (2009), which studies the effectiveness of a feather coating on a circular cylinder. However, since the present study is for a stream-lined body of an aerofoil, it becomes more important to resolve the flow structures close to the body, owing to the increased complexity of the shape.

Schematically, the computational domain is divided into three parts: the solid body or the aerofoil, the surrounding fluid in movement and a mixed fluid-solid part corresponding to the poro-elastic, compliant coating. The assumptions on state variables are that there is no mass exchange between the fluid and solid parts; and the temperature is constant at all times.

2.1 Background of the IB method

The method of immersed boundaries was first developed by Charles Peskin in the seventees to simulate cardiac mechanics and related blood flow. The noteworthy difference between this method and approaches used before for complex geometries was that the complete simulation was performed on a Cartesian grid which was non-conformal to the heart's boundary. To account for the forces on the boundary, a new formulation for imposing the effect of the immersed boundary on the flow was introduced. A more recent account of this work can be seen in Peskin (2002). Since this method first came into being, there have been many changes as well as improvements made to it, to include various ranges of governing physical parameters like the rigidity of the solid boundary and viscosity in the flow. Here, this technique includes all non-conformal grid methods to simulate viscous flows around immersed solid boundaries.

The advantages of the IB method become pertinent when it is compared with the methods of body-conformal, structured as well as unstructured, grids. Despite the measure by which an optimal cartesian grid scales with increasing Reynold's number as compared to body-conformal grids, the first advantage of the IB method is the absence of grid transformation terms in the governing equations. Secondly, it is more adaptive to line-iterative techniques, with a consequent reduction in computational costs. Further, it does not require iterative grid generation, even for complex moving boundaries, since it uses a stationary, non-deforming Cartesian grid and the equations are modified in the neighbourhood of the boundary.

In the following section, the Immersed Boundary formulation used in this thesis will be outlined.

2.2 Boundary conditions on immersed bodies

As mentioned before, there exist different methods depending on the nature of the immersed boundary - for instance, whether it is rigid or elastic. Peskin first developed it for elastic boundaries - specifically, for the muscle contraction in a beating heart. Since our focus is on an aerofoil, the immersed boundary method for rigid boundaries will be outlined. Before this, it is important to note that flows around rigid boundaries can not be considered as a limiting case of flows around elastic boundaries, because elastic constitutive laws become ill-posed in the rigid limit.

As indicated in Section 2.1, the fluid equations will need terms that account for forces on boundaries immersed in the fluid. From the papers of Fadlun et al. (2000) and Mittal & Iaccarino (2005), this volume force $\overrightarrow{F}(\overrightarrow{x}_s, t)$ due to an infinitesimal boundary element at position $\overrightarrow{x}_s$ at time t has the following expression:

$$\overrightarrow{F}(\overrightarrow{x}_s, t) = M\left\{\alpha \int_0^t [\overrightarrow{V}(\overrightarrow{x}_s, t^{'}) - \overrightarrow{U}(\overrightarrow{x}_s, t^{'})]dt^{'} + \beta[\overrightarrow{V}(\overrightarrow{x}_s, t) - \overrightarrow{U}(\overrightarrow{x}_s, t)]\right\} \tag{2.1}$$

where M is a smooth scalar field (for instance, like a hyperbolic function), with the dimension of density, and assumes the value one inside the body whose immersed boundary is under consideration, and zero outside the body in the fluid domain. This function will be referred to henceforth as the mask function. $\overrightarrow{V}(\overrightarrow{x}_s, t)$ is the velocity of the fluid desired at the boundary, imposed as a boundary condition, and $\overrightarrow{U}(\overrightarrow{x}_s, t)$ is the fluid velocity variable. α and β are positive constants with the dimensions of $time^{-2}$ and $time^{-1}$ respectively. The above quantity can be interpreted as a feedback to the velocity difference $\overrightarrow{V}(\overrightarrow{x}_s, t) - \overrightarrow{U}(\overrightarrow{x}_s, t)$ and behaves in such a manner so as to impose $\overrightarrow{U}(\overrightarrow{x}, t) = \overrightarrow{V}(\overrightarrow{x}, t)$ on the immersed boundary over a long period of time. Here $\overrightarrow{x}$ is the local coordinate of the infinitesimal boundary element being considered. In fact, the first term is the time average of the velocity difference over a time span beginning from the initial time to the present time, while the second term is the resistance offered by the boundary surface element to assume a velocity $\overrightarrow{U}(\overrightarrow{x}, t)$ different from $\overrightarrow{V}(\overrightarrow{x}, t)$. The parameters α and β are selected suitably so that the velocity difference $\overrightarrow{V}(\overrightarrow{x}_s, t) - \overrightarrow{U}(\overrightarrow{x}_s, t)$ within and on the immersed boundary is below a sufficiently small threshold value, and is thus considered zero for practical purposes.

The above force expression reduces the behaviour of the system to that of a damped harmonic oscillator. In fact, if we consider the incompressible Navier-Stokes' equations (in dimensional form) given by:

$$\rho[\frac{\partial\overrightarrow{U}}{\partial t}+(\overrightarrow{U}\cdot\bigtriangledown)\overrightarrow{U}]=-\bigtriangledown p+\mu\bigtriangledown^{2}\overrightarrow{U}+\overrightarrow{F};\bigtriangledown\cdot\overrightarrow{U}=0 \tag{2.2}$$

where $\overrightarrow{U}=(u,v)$ is the Eulerian velocity, p is the pressure, μ is the dynamic viscosity, ρ is the density, $\overrightarrow{F}$ is a volume force and retain only the instantaneous acceleration term and the force term and subtract the constant boundary velocity $\overrightarrow{V}$ from the velocity $\overrightarrow{U}$, then we get the following equation.

$$\frac{\partial\vec{q}}{\partial t}\approx-\overrightarrow{F}=-[\alpha\int_{0}^{t}\overrightarrow{q}(\overrightarrow{x}_{s},t^{'})dt^{'}+\beta\overrightarrow{q}(\overrightarrow{x}_{s},t)] \tag{2.3}$$

with $\overrightarrow{q}=\overrightarrow{V}-\overrightarrow{U}$. Equation (2.3) describes the dynamics of a damped harmonic oscillator with frequency $(1/2\pi)\sqrt{|\alpha|}$ and damping coefficient $-\beta/(2\sqrt{|\alpha|})$,i.e, the force $\overrightarrow{F}$ brings back $\overrightarrow{U}$ to $\overrightarrow{V}$ as the former becomes different from the latter on the boundary. The damping term of the force proportional to β helps the boundary velocity to converge to the target velocity by reducing oscillations around it - just like a mass attached to a spring perturbed from its equilibrium position behaves.

For an unsteady flow, it is known that $|\alpha|$ must be sufficiently large so that the restoring force can react with a frequency larger than any frequency in the flow, and the optimal values of the constants α and β can only be obtained empirically, as of now. However, some physical limitations can be imposed on the magnitude of these parameters. For instance, a very large α would in fact cause the restoring force term to become very large and the frequency of the oscillations to tend to infinity. An analogy drawn with a spring-mass system tells us that the spring breaks when the spring constant (which is analogous to the parameter α) is very large. On the contrary, a large β implies high damping and as a result, a force that is not that reactive. Some more insight on tuning these parameters is presented in sections 2.3.2 and 2.5.

2.3 Physical model & computational method for aerofoil

2.3.1 Fluid domain equations

The simulation of the unsteady flow around the NACA0012 aerofoil, which is symmetric about its mean camber line, is done by directly resolving the incompressible Navier-Stokes and continuity equations (cf. equation 2.2) on a Cartesian grid in a two-dimensional periodic domain by means of the immersed boundary method, as presented in §2.2. Now, $\overrightarrow{F}$ is a volume force accounting for the effects of boundaries immersed in the domain, namely, the aerofoil, the coating layer and a buffer zone. The buffer zone, located towards the end of the computational domain, plays the role of damping the unsteady structures in the aerofoil's wake, before they reach the end of the domain. Since here we are considering a domain with periodic boundary conditions, the buffer zone also enforces the periodic inflow-outflow condition on the velocity field (cf. figure 2.1).

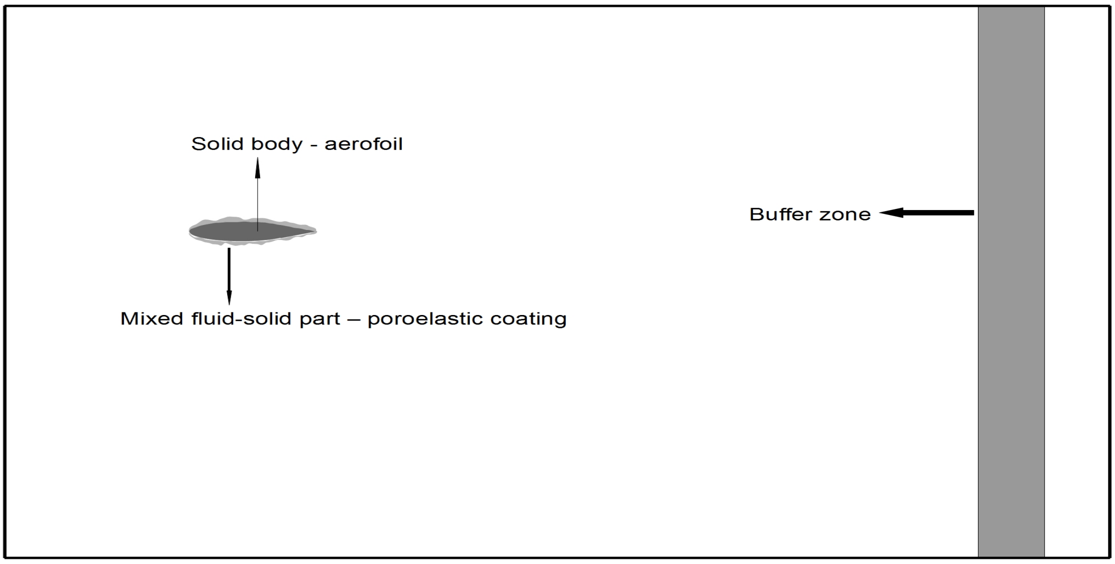

Figure 2.1: Schematic diagram of the computational domain showing the three boundaries immersed in the fluid in movement - solid aerofoil, compliant coating and buffer zone.

The total force $\overrightarrow{F}$ is thus decomposed as:

$$\overrightarrow{F} = \overrightarrow{F}^a + \overrightarrow{F}^b + \overrightarrow{F}^c. \tag{2.4}$$

where $\overrightarrow{F}^a$ and $\overrightarrow{F}^b$ are the forces that render the fluid velocities equal to the values desired on the boundaries of the aerofoil and the buffer layer, which are $\overrightarrow{0}$ and the free-stream velocity $\overrightarrow{U_\infty} = (u_\infty, 0)$, respectively. $\overrightarrow{F}^c$ is the force due to the compliant coating and will be described in section 2.7.1. Mathematically, $\overrightarrow{F}^a$ and $\overrightarrow{F}^b$ are given by:

$$\overrightarrow{F}^a = M^a \left\{ \alpha^a \int_0^t (\overrightarrow{0} - \overrightarrow{U}) dt + \beta^a (\overrightarrow{0} - \overrightarrow{U}) \right\}, \tag{2.5}$$

$$\overrightarrow{F}^b = M^b \left\{ \alpha^b \int_0^t (\overrightarrow{U_\infty} - \overrightarrow{U}) dt + \beta^b (\overrightarrow{U_\infty} - \overrightarrow{U}) \right\}. \tag{2.6}$$

This formulation of the immersed boundary method is referred to as *feedback forcing*, as outlined in §2.2.

The mask functions M^a and M^b involve tangent hyperbolic functions as defined below:

Definition of M^a:

A fixed set of equally spaced points is chosen on the upper boundary of the aerofoil. A similar set of points with their abscissae similar to the points on the upper boundary is chosen on the lower boundary of the aerofoil. In this thesis, we consider 400 points each on the upper and lower boundaries. This complete set of points is referred to as £ here. , i.e, £ consists of 800 points. A point $P \equiv (x, y)$ within a square neighbourhood around the aerofoil, of area equal to $4 \times D^2$ (D being the aerofoil chord length which is the characteristic length in the problem), is first transformed to lie on a line parallel to the aerofoil's central chord. This point now is called $P_r \equiv (x_r, y_r)$. If its abscissa x_r lies between the abscissae x_l and x_{l+1} of two points $A \equiv (x_l, y_{ext}(l))$ and $B \equiv (x_{l+1}, y_{ext}(l+1))$ respectively on the outer boundary of the aerofoil, the outer linear interpolant y^{ext}_{interp} of its ordinate y_r is calculated as follows:

$$y^{ext}_{interp}(y_r) = y_{ext}(l) + \left\{ \frac{y_{ext}(l+1) - y_{ext}(l)}{x_{l+1} - x_l} \right\} (x_r - x_l) \tag{2.7}$$

Similarly, if the abscissa x_r lies between the abscissae x_l and x_{l+1} of two points $A' \equiv (x_l, y_{int}(l))$ and $B' \equiv (x_{l+1}, y_{int}(l+1))$ respectively on the inner boundary of the aerofoil, the inner linear interpolant y^{int}_{interp} of y_r is calculated by:

$$y^{int}_{interp}(y_r) = y_{int}(l) + \left\{ \frac{y_{int}(l+1) - y_{int}(l)}{x_{l+1} - x_l} \right\} (x_r - x_l) \tag{2.8}$$

The mask function at P is now defined as:

$$M^a(x,y) = 0.5[tanh(\frac{200(y_r - y^{int}_{interp}(y_r))}{D}) + 1] \left\{ 1 - 0.5[tanh(\frac{200(y_r - y^{ext}_{interp}(y_r))}{D}) + 1] \right\} \tag{2.9}$$

Elsewhere, the value of this function is 0.

Definition of M^b:

This definition is dependent on the horizontal length L of the computational domain under consideration, and is given by:

$$M^b(x,y) = 0.5[tanh\left\{20(\frac{x}{L} - 0.8)\right\} + 1] + 0.5[tanh\left\{20(\frac{x}{L} - 0.95)\right\} + 1] \tag{2.10}$$

If this value is less than 10^{-2}, it is redefined to be 0. Elsewhere, the value of this function is 0.

These recipes ensure that M^a and M^b, as functions defined over the whole computational domain, smoothly vary from 0 to 1.

$\overrightarrow{F}^c$ is the force due to the compliant coating, to obtain which again multiplication by a scalar field M^c (similar to M above) is involved. Some of these details will be outlined in section 2.7.1.

2.3.2 Tuning of the IB parameters

The optimal set of parameters is selected after monitoring the behaviour of the oscillations of the IB forces. Parameters which yield forces that eventually have mean magnitude of the order of 10^{-3} or lesser are taken to be optimal. Further, parameters which gave damped oscillations about their stabilized magnitudes of means were selected, to simulate the behaviour of a damped oscillator which has a strong enough restoring force with optimal damping. Also, these parameters acted so that the pressure did not show non-physical oscillations. Some more restrictions on selecting the IB parameters for the buffer zone are outlined in §2.5

2.3.3 Numerical resolution

:

The Navier-Stokes equations (2.2) are first normalized using the following scales for the variables:

$$\vec{X'} = \frac{\vec{X}}{D}; \vec{U'} = \frac{\vec{U}}{u_\infty}; P' = \frac{P}{\rho(u_\infty)^2}; t' = \frac{t u_\infty}{D}; \vec{F'} = \frac{\vec{F}}{\dfrac{\rho(u_\infty)^2}{D}} \tag{2.11}$$

Henceforth, only the normalized equation will be used and the normalized variables therein will be denoted without the superscript $'$. The normalized equation thus reads as:

$$\frac{\partial \overrightarrow{U}}{\partial t} + (\overrightarrow{U} \cdot \bigtriangledown)\overrightarrow{U} = - \bigtriangledown p + \frac{1}{Re} \bigtriangledown^2 \overrightarrow{U} + \overrightarrow{F}; \bigtriangledown \cdot \overrightarrow{U} = 0 \tag{2.12}$$

where $Re = \dfrac{\rho u_\infty D}{\mu}$ is the Reynolds number of the flow, based on the free-stream velocity $\overrightarrow{U_\infty} = (u_\infty, 0)$ and the aerofoil chord length D.

The discretization is done on a staggered grid with the pressure defined in the cell midpoints, the horizontal components of the velocity and force placed on the vertical cell interfaces; and the vertical components of the velocity and force placed on the horizontal cell interfaces. To impose incompressibility, the divergence of the velocity field is initialized to zero.

These equations are solved by employing a projection approach, which relies on the following sequence of three steps:

1. Intermediate velocity field components $\overrightarrow{U}^* = (u^*, v^*)$ are calculated by updating the present values with the convective and viscous terms. The convective part is calculated us-

ing the explicit two-step Adams-Bashforth scheme while the viscous part is calculated using the semi-implicit Crank-Nicolson method. This is formulated as:

$$\overrightarrow{U}^{**} = \overrightarrow{U}^{n} + \Delta t \left\{ \underbrace{-1.5(\overrightarrow{U}^{n} \cdot \bigtriangledown)\overrightarrow{U}^{n} + 0.5(\overrightarrow{U}^{n-1} \cdot \bigtriangledown)\overrightarrow{U}^{n-1}}_{\textbf{convective part by explicit two-step scheme}} + \underbrace{\frac{1}{Re}(0.51 \bigtriangledown^{2} \overrightarrow{U}^{**} + 0.49 \bigtriangledown^{2} \overrightarrow{U}^{n})}_{\textbf{viscous part by semi-implicit scheme}} \right\} \tag{2.13}$$

thus yielding the intermediate velocity field $\overrightarrow{U}^{*}$ as:

$$\overrightarrow{U}^{*} = \overrightarrow{U}^{n} + \Delta t \left\{ -1.5(\overrightarrow{U}^{n} \cdot \bigtriangledown)\overrightarrow{U}^{n} + 0.5(\overrightarrow{U}^{n-1} \cdot \bigtriangledown)\overrightarrow{U}^{n-1} + 0.49\frac{1}{Re} \bigtriangledown^{2} \overrightarrow{U}^{n} \right\} \tag{2.14}$$

where $\overrightarrow{U}^{*}$ is in fact $(I - 0.51\frac{\Delta t}{Re}\bigtriangledown^{2})\overrightarrow{U}^{**}$. The spatial derivatives involved here are computed using centered differences for a non-uniform mesh.

2. The Laplacian of the pressure field at the next time step is calculated by imposing the incompressibility condition on the velocity field. That is, using the pressure-correction equation:

$$\frac{\overrightarrow{U}^{rhs} - \overrightarrow{U}^{*}}{\Delta t} = -\nabla p^{n+1} + \overrightarrow{F}^{n} \tag{2.15}$$

where $\overrightarrow{U}^{rhs} = (I - 0.51\frac{\Delta t}{Re}\bigtriangledown^{2})\overrightarrow{U}^{n+1}$. The divergence of (2.15) yields:

$$\Delta p^{n+1} = \frac{\nabla.\overrightarrow{U^{*}}}{\Delta t} + \nabla.\overrightarrow{F}^{n} \tag{2.16}$$

The pressure field at the next time step is calculated using the conjugate gradient method for the Poisson equation. It should be noted that since periodic boundary conditions are used, the conjugate gradient method for the pressure-Poisson solver can be safely used.

3. Finally the velocity field at the (n+1)th time-step is calculated after correcting the pressure as shown below:

$$\overrightarrow{U}^{n+1} = (I - 0.51\frac{\Delta t}{Re}\bigtriangledown^{2})^{-1} \left\{ \overrightarrow{U}^{*} - \Delta t(\nabla p^{n+1}) + \Delta t(F^{n}) \right\} \tag{2.17}$$

The aerodynamic performance is measured in terms of the non-dimensional time-averaged drag and lift coefficients derived from the instantaneous drag and lift coefficients, obtained by integrating the horizontal and vertical components of the total force over the aerofoil. That is, they are given respectively by:

$$(C_d)^n = \frac{\iint (F^n)_x(x,y)dxdy}{0.5\rho D(u_\infty)^2} \tag{2.18}$$

$$(C_l)^n = \frac{\iint (F^n)_y(x,y)dxdy}{0.5\rho D(u_\infty)^2} \tag{2.19}$$

2.4 Numerical convergence of the fluid model

Since a Cartesian grid is used for the computations, which is non-conformal to the shape of the aerofoil, the mesh is concentrated near the aerofoil, to resolve the wake near it, and sparse far away from it (cf. figure 2.2).

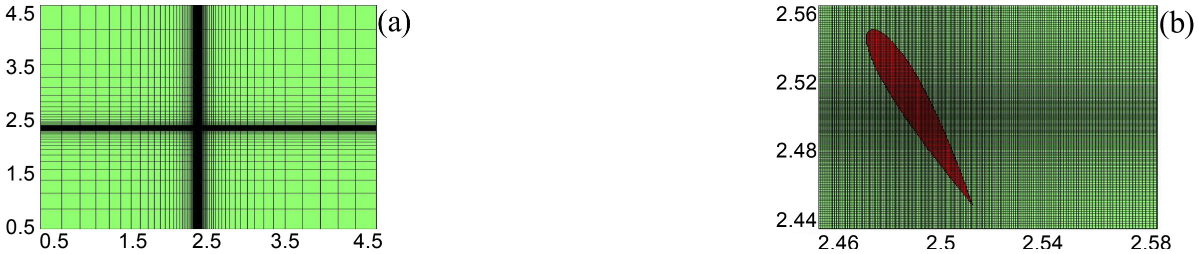

Figure 2.2: (a) Distribution of grid points over the whole computational domain; only one in every 10 lines is shown; the aerofoil is at the domain's centre, at the intersection of the horizontal and vertical black bands. (b) Detail of the grid in the vicinity of the aerofoil.

At $Re = 1100$, given a fixed grid size, it is seen that whereas for a relatively small angle of attack, a domain with dimensions $60D \times 30D$ gives grid-converged results, for angles of attack of around 40° going to high angles of around 70°, a domain with transverse length of $50D$ or more (possibly, as big as $80D$) is required. Once an optimal domain is decided upon, grids with a number of cells ranging from 500×300 to 1000×600 cells are tested to decide on the optimal grid. For instance, at 70°, the domain $50D \times 50D$ with 700×500 cells has been found to provide grid-converged average lift and drag coefficients (cf. figure 2.3).

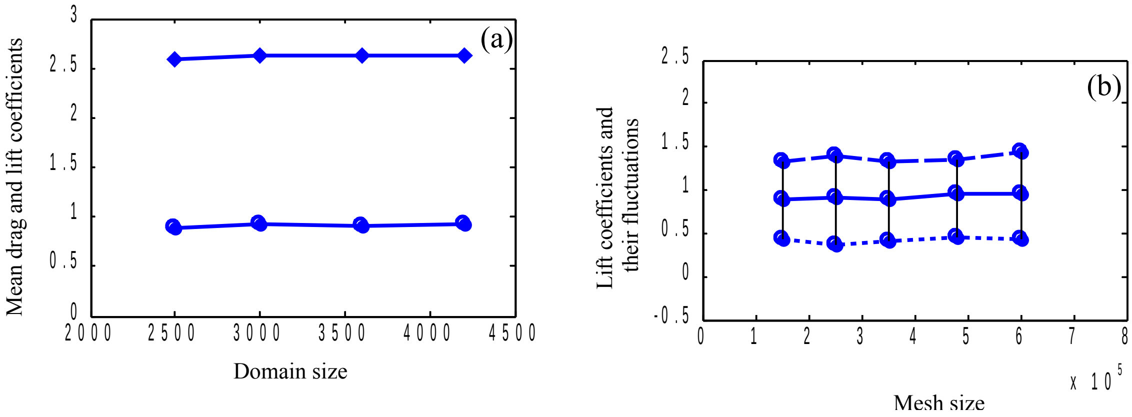

Figure 2.3: Spatial convergence of fluid solver. (a) Mean lift (bottom) and mean drag (top) coefficients as functions of domain size (in units of D^2), with mesh size fixed to 700x500. (b) Mean lift coefficient, together with the instantaneous maximum and minimum values during an oscillation cycle, as functions of the total number of grid points for a domain size fixed to 50Dx50D.

2.5 Validity of boundary conditions

In all the simulations using periodic boundary conditions in this thesis, the forcing from the buffer zone at the end of the computational domain (cf. fig. 2.1), induced by means of the IB parameters α^b and β^b (cf. eqn. 2.6), ensured that no dominant frequencies enter the inflow owing to such periodicity. For any given simulation, this fact has been ascertained by examining the frequency spectrum of the inflow streamwise velocity and comparing it with the frequency spectrum of some typical spatially-integrated quantity like the drag coefficient. It has been ensured that the amplitude of such inflow frequencies is typically at least one order less than that of the dominant frequencies in the flow, an instance of which is shown in fig. 2.4.

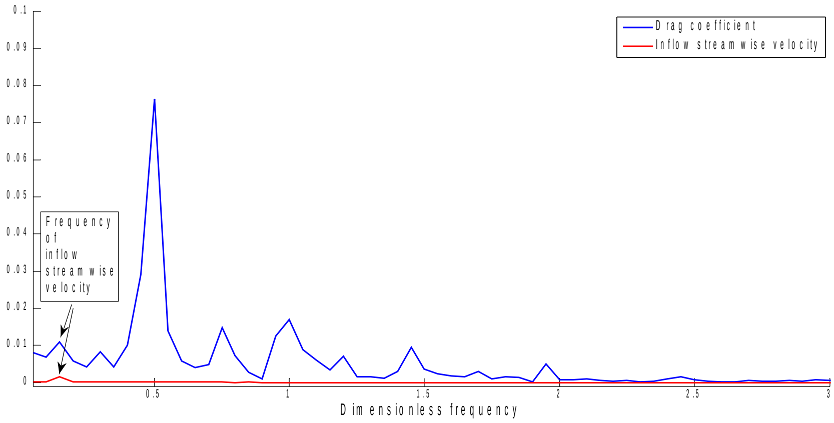

Figure 2.4: Comparison of the Fourier spectra of the drag coefficient (blue curve) with that of the inlet streamwise velocity (red curve), for the NACA0012 aerofoil at an angle of incidence of 22°.

2.6 Validation of numerical method

To validate the immersed boundary technique, which also uses a non-uniform mesh here, the time-averaged lift coefficients were computed for various angles of attack ranging from 20° to 70°. They showed good comparison with the results of Soueid et al. (2009) (cf. fig. 2.5). In addition, the results compared well with results from the commercial computational fluid dynamics software FLUENT not only in the time domain but also in the frequency domain (cf. fig. 2.6).

2.7 Feather layer model

Since the porous, compliant coating is meant to mimic a dense cluster of feathers (which is infeasible to model owing to very large number of degrees of freedom), a discrete number of reference beams, homogeneously spread over the layer, is chosen to approximate the anisotropic compliant coating of variable porosity. Each reference beam is a rigid circular cylinder, surrounded symmetrically by a control volume (cf. figure 2.7(a)). The dynamics

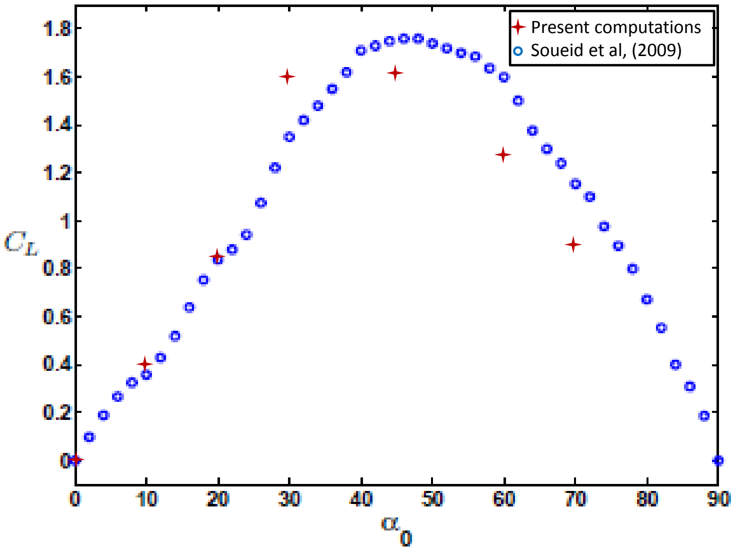

Figure 2.5: Comparison of time-averaged values of lift coefficients for the NACA0012 aerofoil at various angles of attack, obtained from the fluid solver.

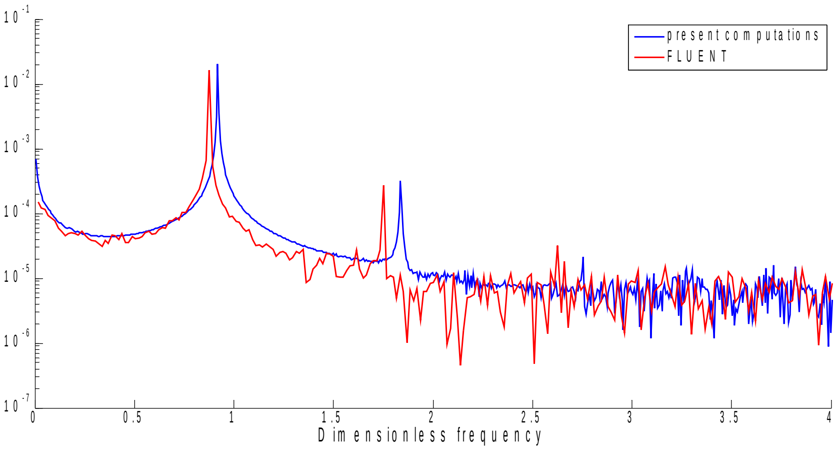

Figure 2.6: Comparison of the Fourier spectra of lift coefficients for the NACA0012 aerofoil at 10° angle of attack - the blue curve is from present computations while the red curve is obtained from FLUENT

of the reference beams, which are modelled as being connected to each other by non-linear dampers and springs, is solved by a set of non-linear dynamical equilibrium equations (which will be indicated in §2.7.2). The coupling between the fluid and structure is outlined next.

2.7.1 Coupling between fluid and structure

The interaction between the fluid and the coating is estimated as the drag force past a cluster of long thin cylinders. This force per unit volume $\overrightarrow{F}^c$ is split into the two components tangential and normal to each such thin cylinder, of magnitudes F_t^c and F_n^c, respectively. To approximate these, two variables are defined, namely the packing density ϕ, which captures the variable porosity of the coating, and the unit orientation vector $\overrightarrow{d}$ of each feather in the control volumes, which measures the anisotropic nature of the layer (cf. figure 2.7(b)). The packing density is defined by $\phi = \frac{V_{feather}}{V_{layer}}$, or the ratio of the volume occupied by the feathers over the total sampling volume. Hence, it varies continuously with time between 0 and 1 within the coating.

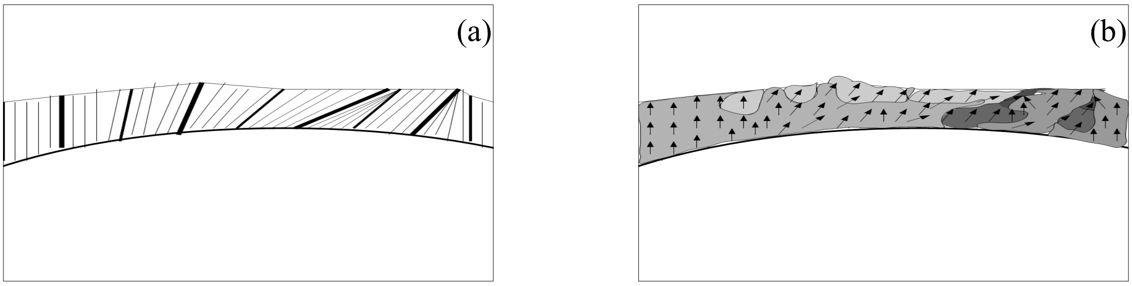

Figure 2.7: Feather layer model. (a) Homogenized approach; the thickest lines are the reference beams, each of them being surrounded by control volumes. The position and velocity of individual elements in a control volume (shown by thin lines) is interpolated from the position and velocity of the reference beams. (b) Representation of the variable porosity (in terms of the packing density variable) and anisotropy (in terms of the orientation vector) of the layer - a darker shade stands for higher packing density.

For each point P in the fluid lying in some control volume of the coating, there corresponds a velocity $\overrightarrow{U}^c$ relative to the velocity $\overrightarrow{V}^c$ of the feather on which P lies. This is given by

$\overrightarrow{U}^c = \overrightarrow{U} - \overrightarrow{V}^c$, where $\overrightarrow{U}$ is the fluid velocity at P. The projection of this relative velocity in the direction along the unit orientation vector $\overrightarrow{d}$ gives the tangential component with magnitude U_t^c, while the projection perpendicular to $\overrightarrow{d}$ gives the normal component, with magnitude U_n^c. Reynolds numbers corresponding to these tangential and normal components are defined as $Re_t^c = \frac{U_t^c d_c}{\nu}$ and $Re_n^c = \frac{U_n^c d_c}{\nu}$ respectively, where the length scale d_c is the diameter of the covert feather (i.e. of each thin cylinder).

The hypothesis is made that F_n^c is a function of ϕ and Re_n^c only, under the assumption that Re_n^c is not greater than 180. Making use of the model by Koch & Ladd (1997), which proposes a linear approximation in terms of Re_n^c, we get:

$$\frac{\mathcal{F}_n^c}{\mu U_n^c} = c_0(\phi) + c_1(\phi) Re_n^c, \tag{2.20}$$

where $\mathcal{F}_n^c$ is the normal force per feather per unit length. The coefficient $c_0(\phi)$ is the Stokes' drag approximated using Brinkman's law at the Stokes flow limit, while $c_1(\phi)$ is the inertial drag in the larger-than-zero Re_n^c case and is estimated from the values assumed by the ratio $\frac{c_1}{c_0}$ for different values of ϕ, as done by Koch and Ladd. Thus, $F_n^c = \dfrac{4\phi}{\pi d_c^2} \mathcal{F}_n^c$.

As for the tangential component $\frac{F_t^c}{\mu U_t^c}$, a formula is derived (based on Favier et al. (2009)) for the case of steady axisymmetric flow in the Stokes regime between concentric cylinders. By using Stokes equations in cylindrical coordinates and assuming that $\dfrac{\partial}{\partial z} = \dfrac{\partial}{\partial \theta} = \dfrac{\partial}{\partial t}$, $u_r = u_\theta = 0$, one obtains:

$$\frac{-F_t^c}{\mu} = \frac{\partial^2 u(r)}{\partial r^2} + \frac{1}{r}\frac{\partial u(r)}{\partial r} \tag{2.21}$$

with the boundary conditions $u(r_1) = 0$ and $\dfrac{\partial u}{\partial r}|_{r=r_2} = 0$, where $r_1 = \dfrac{d_c}{2}$ and $r_2 - r_1$ is the distance between two cylinders in the cluster. Taking $\phi = \dfrac{\partial u}{\partial r}$, this equation becomes:

$$\phi^{'}(r) + \frac{1}{r}\phi(r) + \frac{F_t^c}{\mu} = 0 \tag{2.22}$$

which, alongwith the boundary condition $\dfrac{\partial u}{\partial r}|_{r=r_2} = 0$, yields the solution:

$$\phi(r) = \frac{F_t^c}{2\mu}(\frac{r_2^2}{r} - r) \tag{2.23}$$

Using $\phi = \dfrac{\partial u}{\partial r}$ and the boundary condition $u(r_1) = 0$, one obtains:

$$u(r) = \frac{F_t^c}{4\mu}(2r_2^2 ln\frac{r}{r_1} + r_1^2 - r^2) \tag{2.24}$$

We now consider the incoming velocity with value U_t^c and the mass flux J of the flow through the space between the cylinders given by $\rho\pi(r_2^2 - r_1^2)U_t^c(1-\phi)$, where it should be recalled that $\phi = \dfrac{r_1^2}{r_2^2}$. J is also given by $\rho \int_0^{2\pi} d\theta \int_{r_1}^{r_2} u(r) r dr$. Equating these two values of J, one gets:

$$\frac{F_t^c}{\mu U_t^c} = \frac{4}{d_c^2}\frac{8\phi(1-\phi)}{\{\phi - 1 + [2/(\phi-1)]ln\phi - 2\}}. \tag{2.25}$$

These force components, which are obtained for each grid point in the control volumes are transferred to the frame of the reference beams, by integration over each control volume.

It should be noted that the normal and tangential components of the force are respectively dependent on the normal and tangential velocity components, which in turn are dependent on the angles made by each of the reference beams with the aerofoil surface, and vice-versa. As a consequence, depending on whether the normal or tangential force contributions is greater, the feathers have a tendency to either favour or oppose alignment with the free-stream flow. In this model, the condition is imposed on the reference beams that they should never make a 90° or an obtuse angle to the free-stream flow.

2.7.2 Dynamics of the compliant coating

The forces in action are taken to be concentrated on N reference beams. The motion of such thin rigid circular-cylindrical beams, hinged to the aerofoil surface, of length l and diameter d_c, are found in terms of the angular displacement about their equilibrium angle θ_{eq}, denoted by $\theta(1), ..., \theta(N)$. All angles involved in the structure model are defined with respect to the positive horizontal axis. The different moments that are considered in the model are now illustrated (cf. figure 2.8).

Rigidity: Each reference beam can oscillate within a sector$[\theta_{min}, \theta_{max}]$ around its equilibrium angle θ_{eq}, its angular frequency being controlled by the rigidity parameter K_r (having

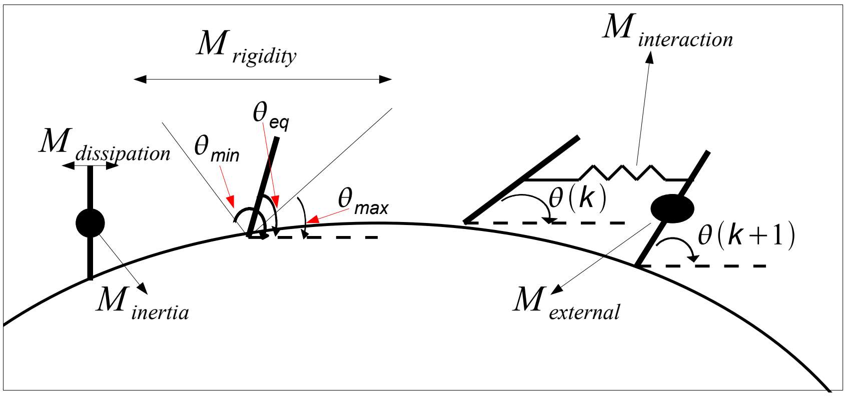

Figure 2.8: Moments in the structure model.

dimensions $[M][L]^2[T]^{-2}$). The rigidity moment is then given by:

$$M_{rigidity}(k) = -K_r f_1[\theta(k)]. \tag{2.26}$$

where $f_1[\theta(k)] = (T[\theta(k)] - T(\theta_{eq}))/T^{'}(\theta_{eq})$, with $T(\theta) = tan\left\{\frac{\pi}{(\theta_{max} - \theta_{min})}\theta - \frac{\pi(\theta_{max} + \theta_{min})}{2(\theta_{max} - \theta_{min})}\right\}$. It is to be noted that f_1 is always an increasing function of θ, which vanishes at θ_{eq}. As a consequence, the magnitude of the rigidity moment is greater when it is farther away from θ_{eq} and close to zero in the neighbourhood of θ_{eq} (displaying a linear trend in θ with slope 1), exactly like the restoring force in a spring-mass system.

Interaction: Each reference beam is linked to its adjacent beams by non-linear springs of stiffness K_i (having same dimensions as K_r), with progressive increase in the interaction moment as two adjacent beams approach one another. This feature is modelled in the expression for the interaction moment given by:

$$M_{interaction}(k) = -K_i f_2[\theta(k)]. \tag{2.27}$$

where the non-linear function $f_2[\theta(k)] = \dfrac{tan\{2lsin[\frac{(\theta(k) - \theta(k+1))}{2}]\frac{\pi}{2}\}}{hcos\{\frac{(\theta(k) + \theta(k+1))}{2}\}}$, with h as the distance between two adjacent beams and l the beam's length.

Dissipation: This takes into account the energy dissipation due to plastic deformation of each beam and friction between adjacent feathers, and is given by:

$$M_{dissipation}(k) = -K_d \dot{\theta}(k). \tag{2.28}$$

where K_d is the dissipation parameter (having dimensions $[M][L]^2[T]^{-1}$) that controls the magnitude of the energy lost.
Inertia: This moment is by virtue of the total mass M of all the feathers present in the control volume surrounding a reference beam, and is given by:

$$M_{inertia}(k) = M(\frac{l}{2})^2 \ddot{\theta}(k). \tag{2.29}$$

External force from fluid: This force is obtained by integrating the volume force F^c over the control volume surrounding each reference beam, $V_{control}(k)$. It is given by:

$$M_{external} = \frac{l}{2} F_{ext}(k) = \frac{l}{2} \int_{V_{control}(k)} \|F^c_n\| dV. \tag{2.30}$$

because the tangential component F^c_t of the external force exerts no moment.

The dynamic equilibrium of the system of all reference beams is found by balancing the above moments for each element. Thus, the equation for each reference beam (in dimensional form) is:

$$M l_c^2 \ddot{\theta} + K_r f_1(\theta) + K_i f_2(\theta) + K_d \dot{\theta} = l_c F_{ext}. \tag{2.31}$$

To compare the frequencies present in the structure with those in the flow, characteristic frequencies corresponding to the rigidity, interaction and dissipation moments are defined by $\omega_r = \sqrt{K_r/M l_c^2}$, $\omega_i = \sqrt{K_i/M l_c^2}$ and $\omega_d = K_d/M l_c^2$ respectively (Doaré et al. (2004)). To limit the number of independent parameters, the structure model is taken to be dominated by rigidity effects. The equation is thus made dimensionless by using $t_c^* = t\omega_r$ and $\mu_{ext} = F_{ext}/(M l_c \omega_r^2)$, to yield:

$$\ddot{\theta} + \gamma \dot{\theta} + f_1(\theta) + \kappa f_2(\theta) = \mu_{ext}. \tag{2.32}$$

Here the parameters γ and κ are defined as ω_d/ω_r and ω_i^2/ω_r^2 respectively, and measure the relative importance of each moment involved in the structure model.

2.7.3 Numerical resolution of the structure model

The non-dimensional governing equation (2.31) is solved for each reference beam by using an explicit four-step Runge-Kutta method. Since the mass of the beams considered is not too small, use of an explicit method (as opposed to an implicit method) does not cause numerical oscillations, that consequently delay the achievement of the final equilibrium. Between two iterations in the whole fluid-structure interaction model, the dynamics of the coating is calculated explicitly at each temporal sub-iteration.
The aerodynamic performance is measured again in terms of instantaneous as well as time-averaged drag and lift forces (cf. equations 2.18 and 2.19), which now also incorporate the force due to the structure on the fluid F^c.

2.8 Summary of the two-way coupling

Since this fluid-structure interaction problem requires the simultaneous solution of the equations of both the structure and the flow, a weakly-coupled partitioned solver is used, as summarized below:
(a) With the fluid velocity and pressure initialized to the free-stream velocity and zero respectively, a direct numerical simulation of the unsteady incompressible Navier-Stokes equations is performed, using the feedback forcing formulation of the immersed boundary method, as discussed in sections 2.3.1 and 2.3.3.
(b) The configuration of the reference beams is initialized to the equilibrium angle about which they oscillate while their velocities are initialized to zero. Control volumes around each reference beam and their velocities are defined based on these, and are interpolated to the reference frame of the grid in the fluid domain. The normal and tangential components of the fluid-structure forcing are calculated, based on the fluid velocities in step (a) and velocities at each grid point in the control volumes (cf. §2.7.1). The total force at each grid point with index (i, j), denoted by $F^c_{i,j}$, is now transferred to the frame of each reference

beam (indexed by k) and denoted there by F_k^c, by integrating it over the corresponding control volumes and multiplying by a smooth hyperbolic scalar field M^c (which has the value 1 on the coating and is zero elsewhere).
(c) The dynamics of each reference beam is solved (cf. §2.7.2).
(d) With the positions and velocities of each reference beam found in step (c), the positions and velocities at each grid point of the corresponding control volume are interpolated. With these values and the fluid velocities in step (a), the normal and tangential components of the structure-fluid forcing are found. The total force is evaluated by their resultant multiplied by M^c (cf. §2.3.1). The algorithm is depicted in a flowchart in figure 2.9.

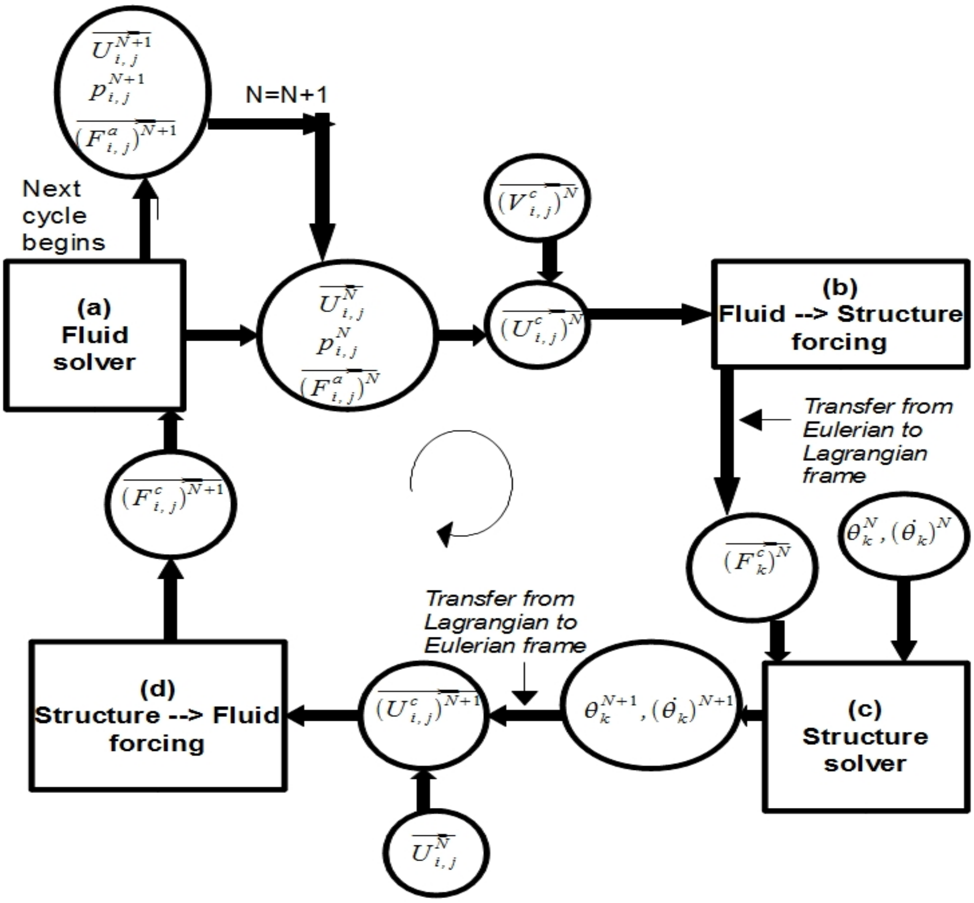
$\overline{U^{N+1}_{i,j}}$
$p^{N+1}_{i,j}$
$\overline{(F^{a}_{i,j})^{N+1}}$
N=N+1
Next cycle begins
(a) Fluid solver
$\overline{U^{N}_{i,j}}$
$p^{N}_{i,j}$
$\overline{(F^{a}_{i,j})^{N}}$
$\overline{(V^{c}_{i,j})^{N}}$
$\overline{(U^{c}_{i,j})^{N}}$
(b) Fluid --> Structure forcing
Transfer from Eulerian to Lagrangian frame
$\overline{(F^{c}_{k})^{N}}$
$\theta^{N}_{k}, (\dot{\theta}_{k})^{N}$
(c) Structure solver
$\theta^{N+1}_{k}, (\dot{\theta}_{k})^{N+1}$
Transfer from Lagrangian to Eulerian frame
$\overline{(U^{c}_{i,j})^{N+1}}$
$\overline{U^{N}_{i,j}}$
(d) Structure --> Fluid forcing
$\overline{(F^{c}_{i,j})^{N+1}}$

Figure 2.9: Weakly-coupled algorithm for two-way fluid-structure interaction.

Summary

A computational problem on the passive flow control over a NACA0012 aerofoil, using a poro-elastic layer of compliant actuators, has been formulated. This problem has been dealt with by the immersed boundary technique, wherein the feedback forcing formulation has been used to treat the fluid part (in a Eulerian framework). On the other hand, the force between the fluid and the structure parts (the latter simplified by a discrete set of elements) has been evaluated as the drag force due to flow past a cluster of randomly-oriented, long, thin cylinders. Finally, the discrete set of reference elements for the structure has been modelled as non-linear spring-mass systems (in a Lagrangian framework). A weakly-coupled partitioned solver puts together all these different components of the problem. This study has been an extension of the model for a circular cylinder (developed by Favier et al. (2009)), to a complex configuration of a NACA0012 aerofoil.

The results for flow in a low-Reynolds number regime, over the smooth aerofoil, have been validated with results available in literature. The circumstances under which the present use of periodic boundary conditions is valid, have also been established.

In the next chapter, results for the complete fluid-structure interaction problem are presented. Further, the modifications in flow fields, due to the presence of the poro-elastic layer, have been interpreted.

Chapter 3

Simulation results: Flow control with coated aerofoils

Introduction

In this chapter, the results, obtained from the numerical procedure outlined in the last chapter, are presented. For the computations for aerofoil coated with compliant actuators, the characteristics of such a carpet have been selected so as to synchronize characteristic time scales of the fluid and the structural systems. Details of such a selection are presented. Further, modifications in flow characteristics, such as the pressure and vorticity fields, which are associated to changes in aerodynamic performance, have been examined. A parametric analysis of the major structural properties of the actuators is also presented, which helps in characterizing “optimal ”structure parameters.

3.1 Aerofoil without control

In order to examine the effectiveness of the poro-elastic coating, the angle of attack at which the lift-to-drag ratio starts to decrease drastically for a smooth aerofoil at incidence, should be determined. For this, computations for angles of attack ranging from 20° to 70° are carried out. These computations are carried out as a special case where the poro-elastic layer is set to be inactive, i.e, there is no force from fluid-to-structure and vice-versa. It is observed that, unlike characteristic stall angles observed in several experiments at high Reynolds numbers, the lift coefficient steadily decreases after around 40°–45° angle of attack (cf. figures 2.5 and 3.1(b)). Besides, the drag continues to increase along with increased fluctuations around this point (cf. figure 3.1(a)).

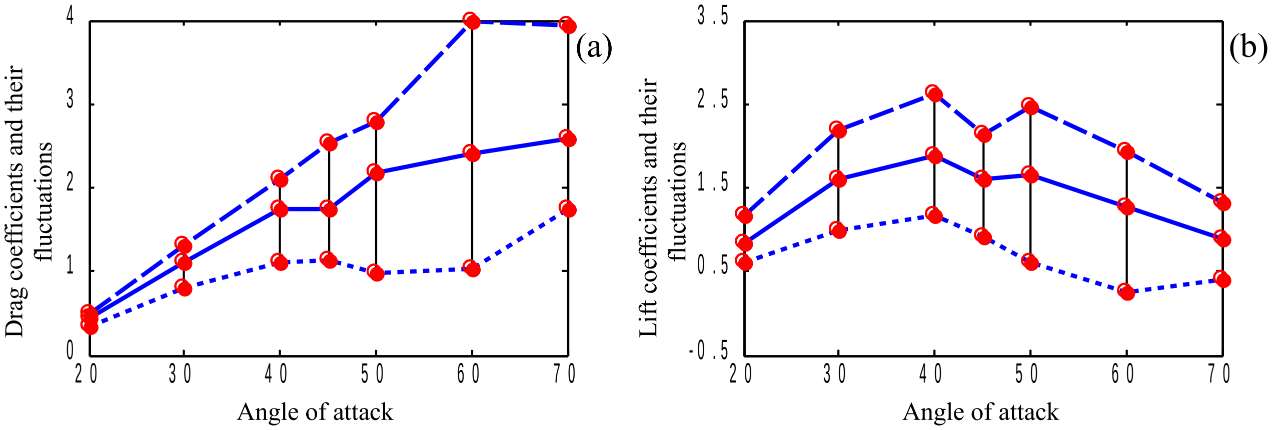

Figure 3.1: Dependence of the dimensionless coefficients of (a) time-averaged drag and (b) time-averaged lift, as the angle of attack of a static NACA0012 aerofoil is varied from 20° to 70°. The thick curves represent the mean values of drag and lift, while the dotted curves above and below these thick curves represent the maximum and minimum values of the instantaneous drag and lift coefficients in the course of the oscillations, respectively.

To determine the effectiveness of the feathers in optimizing the lift-to-drag ratio over the entire range of angles, we will consider the physics at the angles of 22°, 45° and 70°. For this, the signals of the drag and lift coefficients, plotted against time (non-dimensionalized by the free-stream speed and the chord length), are first examined (cf. figure 3.2). It is to be noted that the simulations conducted in this study are characterized by rather large angles of attack, in order to consider cases of perching manoeuvre (and also owing to the fact that due to a low-Re regime, the angle at which the lift starts to decrease is fairly large at around 45°). Further, the use of long simulation times for such cases can be used to assess the *initial* aerofoil performance during a perching manoeuvre of a bird.

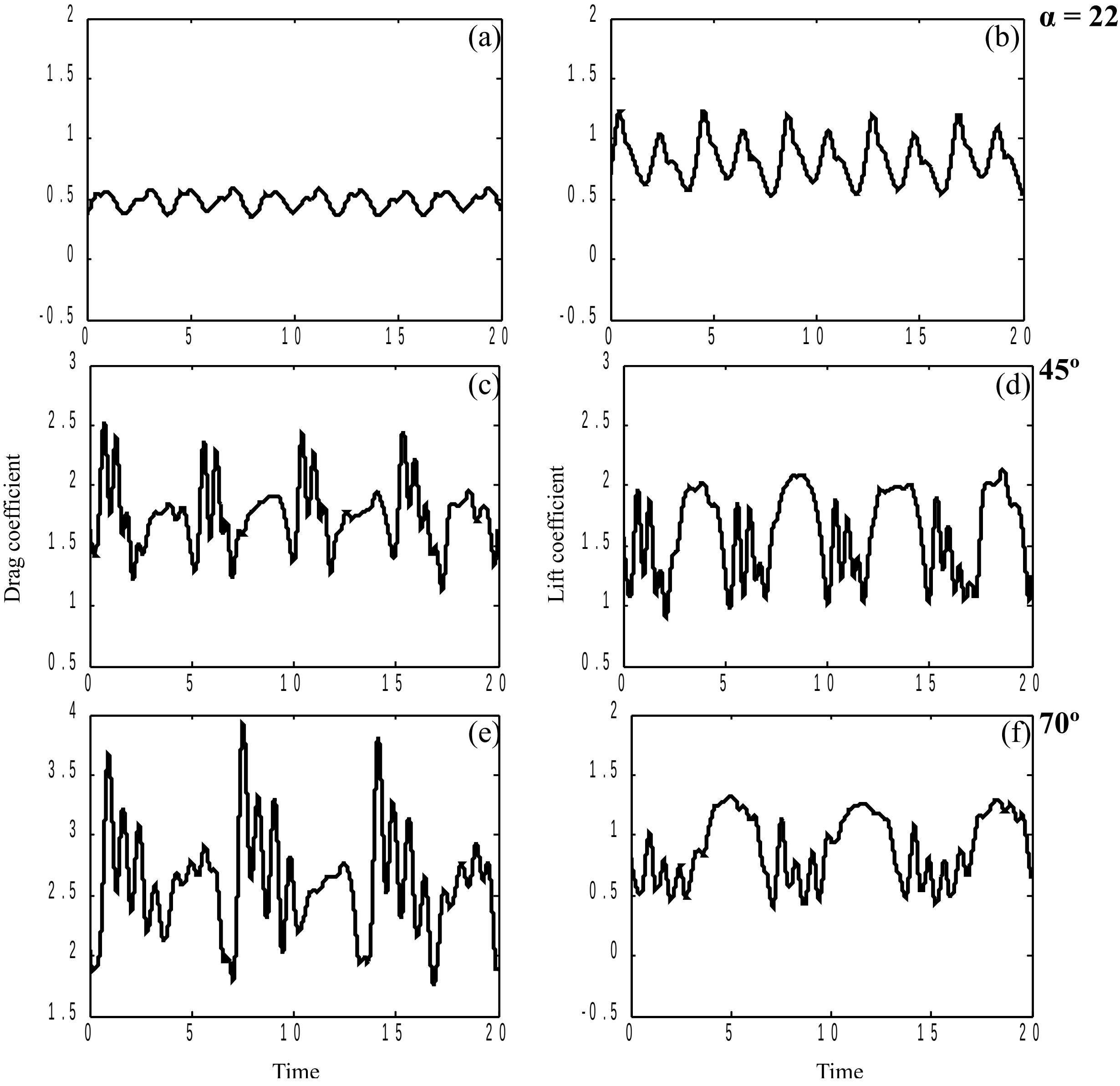

Figure 3.2: Time evolution of the drag (left) and lift (right) coefficients for angles of incidence equal to 22° (top), 45° (middle) and 70° (bottom).

To analyse the release of energy stored in the poro-elastic coating into the boundary layer, which is believed to depend on a frequency synchronisation effect, a Fourier analysis is done for each of these signals. Typically for a small angle of attack, like 22°, a characteristic frequency is observed in the power spectrum. On the contrary, for higher angles of attack, like 45° and 70°, this is not so. Further, for these angles, although the frequencies having non-zero contribution in the power spectra of both the drag and lift signals are the same, the amplitudes corresponding to them in these two signals are different (cf. figure 3.3). Some physical insight into these observations will be provided in §3.4.

3.2 Investigation of the control parameters

The parameter space: We first summarize the parameters involved in this model. There are three coefficients describing the intrinsic properties of the coating material, namely the rigidity coefficient K_r, the interaction coefficient K_i and the dissipation coefficient K_d, as outlined in §2.7.2. We also have the parameters corresponding to the equilibrium angle θ_{eq}, the minimum and the maximum angles θ_{min} and θ_{max}, by which each reference element can deflect. Then, there are the parameters giving the physical dimensions of each reference beam, which is a thin circular cylinder – namely the mass m, the length l and its diameter d_c. Finally, we have the parameters that describe the concentration as well as the relative placement of the coating on the aerofoil, namely the packing density ϕ, the number of reference beams N used to approximate the whole layer; and the coordinates of the points on the aerofoil between which the coating is defined.

Choice of a suitable parameter subset: As indicated in §2.7.2, rigidity effects are taken to predominate the structure model. This assumption helps in choosing a few crucial parameters out of the large parameter space outlined in the previous paragraph. The parameters which are fixed for the whole investigation include N, l, d_c and m. Also, the location of the coating is fixed to 70% of the suction side of the aerofoil, a little away from the leading edge (cf. Table 3.2). The aerofoil is kept smooth close to the trailing edge, because in the case

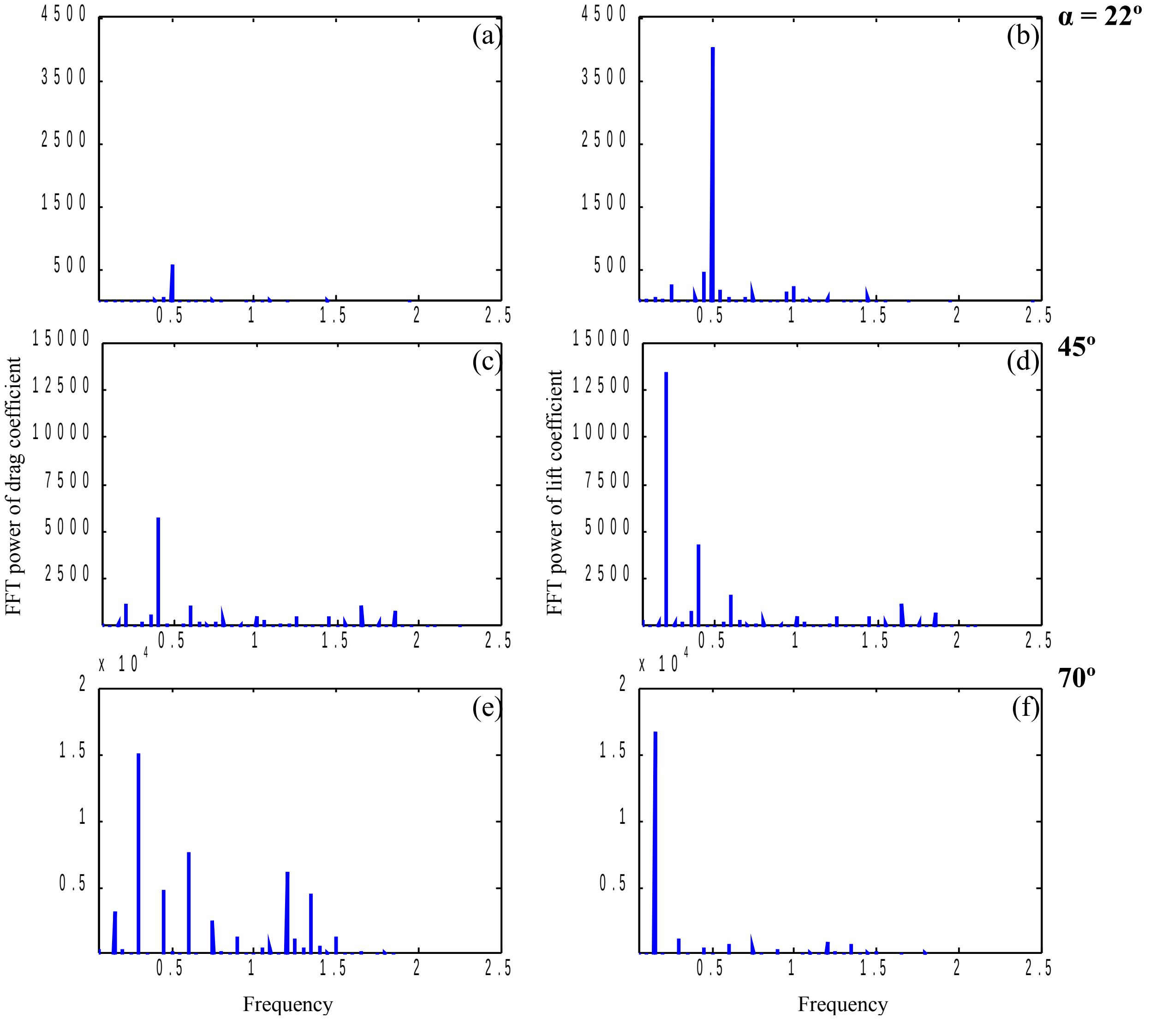

Figure 3.3: Power spectra of the drag (left) and lift (right) signals for angles of attack equal to 22° (top), 45° (middle) and 70° (bottom), corresponding to the time signals shown in figure 3.2. Non-dimensional frequency is plotted along the horizontal axes.

of 22°, the trailing edge vortices were observed to orient the feathers close to the trailing edge almost orthogonally to the flow, which led to some drop in aerodynamic performance. The fixing of the location and extent of the coating, along with fixed N, sets the distance h between two adjacent reference beams, which figures in the definition of the interaction moment (cf. equation 2.26). Next, for this fixed h, l is taken equal to 8.5% of the aerofoil chord length, to effectively model non-bending feathers. Further, l, apart from appearing in the definition of the moment due to the force from the fluid, also figures in the moments due to interaction and inertia (which are taken to be less significant than other terms). The bristles' diameter d_c appears in the definition of the normal and tangential components of the force between the fluid and the structure. As mentioned by Favier et al. (2009), this model is in accordance to those developed by Koch & Ladd (1997) and Howells (1998), which are valid only for moderate normal and tangential Reynolds numbers Re_n^h and Re_t^h (defined in §2.7.1). Here d_c is fixed such that both Re_n^h and Re_t^h do not exceed the value of 10. Finally m, which figures only in the small contribution from the moment due to inertia, is fixed to a suitable value equal to 12 (non-dimensionalized with respect to the mass of the fluid trapped within a control volume surrounding a reference feather).

The parameters which were extensively studied are K_r and ϕ. K_r was tuned according to the dominant frequencies observed in the uncontrolled flow, which correspond to the frequencies of vortex shedding, as seen from the power spectra of the drag and lift signals for the smooth aerofoil. For each of the values of K_r, K_d was fixed according to the following linear stability analysis performed for the equation for coating's dynamics (eqn. (2.31)), considering zero external forcing from the fluid, about the equilibrium angle θ_{eq} (Favier et al. (2009)):

We obtain the following differential equation in terms of the "small" perturbation angle $\theta^{'}$:

$$\ddot{\theta}' + \gamma\dot{\theta}' + \{(f_1)^{'}(\theta_{eq})\}\theta^{'} + \kappa f_2(\theta_{eq} + \theta^{'}) = 0. \tag{3.1}$$

This equation can be further simplified using the properties of f_1 and f_2 that $(f_1)^{'}(\theta_{eq}) = 1$ (i.e, the restoring force owing to rigidity shows a linear trend near the equilibrium angle), and $f_2(\theta_{eq} + \theta^{'}) = 0$ (i.e, force between neighbouring reference beams can be neglected near the equilibrium angle as they do not touch each other), respectively. Now, assuming that the perturbation θ' behaves as $e^{i\omega_c^* t_c^*}$, where ω_c^* is non-dimensional characteristic frequency of the structure model and t_c^* is non-dimensional time variable (both normalized using the rigidity frequency ω_r), we obtain a quadratic equation for ω_c^* with roots:

$$\omega_c^* = \frac{i\gamma \pm \sqrt{(4-\gamma^2)}}{2} \tag{3.2}$$

Fixing γ equal to 0.05, so that there is a small contribution from the dissipation term compared to other terms, we get $i\omega_c^* t_c^* = (-0.025 \pm 0.999i)t_c^*$. The real part of this equation indicates that the system is asymptotically stable due to negative growth rate. Further, for this value of γ, considering the real part of the value of ω_c^* (which is ± 0.999), we get that the dimensional characteristic frequency ω_c is approximately equal to the rigidity frequency ω_r, in line with our hypothesis of the dominance of rigidity term.

Next, K_i was fixed to satisfy the identity $\omega_d < \omega_i < \omega_r$, where ω_r, ω_i and ω_d have been defined before in §2.7.2. Further, to have favourable comparison of $\frac{\mathcal{F}_n^c}{\mu U_n^c}$ and $\frac{\mathcal{F}_t^c}{\mu U_t^c}$ to the theoretical model of Howells (1998), ϕ was chosen to lie roughly in the range $[0.001, 0.01]$. With the parameters chosen as above, now the values for θ_{eq}, θ_{min} and θ_{max} need to be tuned. As for the parameter θ_{eq}, in the case of the angle of attack of 22°, $\theta_{eq} = 0$ (i.e. the initial orientation of the reference beams being parallel to the free-stream) was seen to yield better aerodynamic performance. Hence, for the other angles of attack of 45° and 70°, this configuration was fixed. Finally, for each of these angles of attack, the angular sector $[\theta_{min}, \theta_{max}]$ was chosen to have as high compliance as possible, although always restricting the dynamics of the beams to acute positive angles.

3.3 Aerofoil with control

To control flow separation, it is necessary to optimize the release of energy stored in the boundary layer, at appropriate instants of time. Thus, the idea behind finding the right physical and structural parameters for the poro-elastic coating is to synchronize the vortex shedding and the structures' time scales, to try and trigger a near-resonant response capable of affecting profoundly the physics of this coupled problem. In the light of the fact that the rigidity forces are taken to be predominant, this problem boils down to finding the rigidity parameter K_r, for which the corresponding structure frequency ω_r has a major contribution in the power spectra of the drag or lift signals. Effective non-dimensional control parameters are provided in Tables 3.1 and 3.2.

Angle of attack, α (degrees)	Rigidity moment, K_r	Interaction moment, K_i	Dissipation moment, K_d	Packing density, ϕ	Angular sector of movement, $[\theta_{min}, \theta_{max}]$ (degrees)	Flow frequency, ω_{fluid}
22	8.9905	0.2034	0.0909	0.0085	[-60,21]	0.4772
45	6.8002	0.2034	0.079	0.0022	[-60,60]	0.4151
70	8.9905	0.2034	0.0909	0.0085	[-60,60]	0.4772

Table 3.1: Parameters which have been varied in the course of the parametric search; the values provided here are those which guarantee the best control results. The normalization of the structure moments and the flow frequency is done w.r.t the mass of the reference beam M, half the length of the reference beam l_c and the time scale of the free-stream, which is the ratio between the aerofoil chord length D and the free-stream speed u_∞.

Mass of reference beam, M	12
Length of reference beam, l	8.5×10^{-2}
Diameter of reference beam, d_c	2×10^{-3}
Equilibrium angle/ Initial orientation of reference beams, θ_{eq} (degrees)	0
Extent of the coating	70% of suction side, starting 0.1 units of length after the leading edge and ending 0.2 units before the trailing edge.
Number of reference beams used, N	8

Table 3.2: Parameters fixed throughout the course of the study. Here, length and diameter of a reference beam are non-dimensionalized w.r.t the aerofoil chord length D.

With the parameter K_r so chosen and other parameters fixed as described in the previous

paragraph, we get enhanced performance for all the three angles of attack of 22°, 45° and 70°. Specifically, we get 34.36% and 7.5% mean lift increase for 22° and 70° respectively; and 8.92% and 4.92% mean drag reduction for 45° and 70° respectively. In addition, we obtain 35.47%, 10.46% and 9.71% reduction in drag fluctuations for 22°, 45° and 70° respectively; and 7.15% reduction in lift fluctuations for 22° (cf. fig 3.4).
Some physical insight into why we get these improvements due to changes in the local flow field, is provided in §3.4.

3.4 Physical interpretation of the control

3.4.1 *Parametric study*

A parametric analysis is done of the change in aerodynamic performance, first by varying the rigidity moment K_r while keeping the packing density ϕ fixed and then by varying ϕ while K_r is fixed at an optimum value. All the other parameters are chosen in accordance with §3.2. Although these plots never show regular trends for any of the angles of attack considered, it has been observed that the performance was enhanced (as outlined in §3.3) when K_r was such that the dimensionless rigidity frequency was close to 0.4, over other values of K_r. For instance,

(i) when the angle of attack is 22°, since there was only one frequency, equal to 0.4772, observed in the power spectra of drag and lift signals (cf. figures 3.3 (a) & 3.3 (b)), only control elements with this rigidity frequency were tested, over an extensive range of packing density (cf. figure 3.6 (a));

(ii) in the case of incidence equal to 45°, control elements with rigidity frequency equal to 0.4151 (with a suitable packing density) were seen to produce larger drag reduction, while the mean lift remained roughly unchanged (cf. figures 3.5 (a) and 3.6 (b));

(iii) for an angle of 70°, control elements with rigidity frequency equal to 0.4772 (and a suitable packing density) produced higher drag reduction as well as lift enhancement (cf.

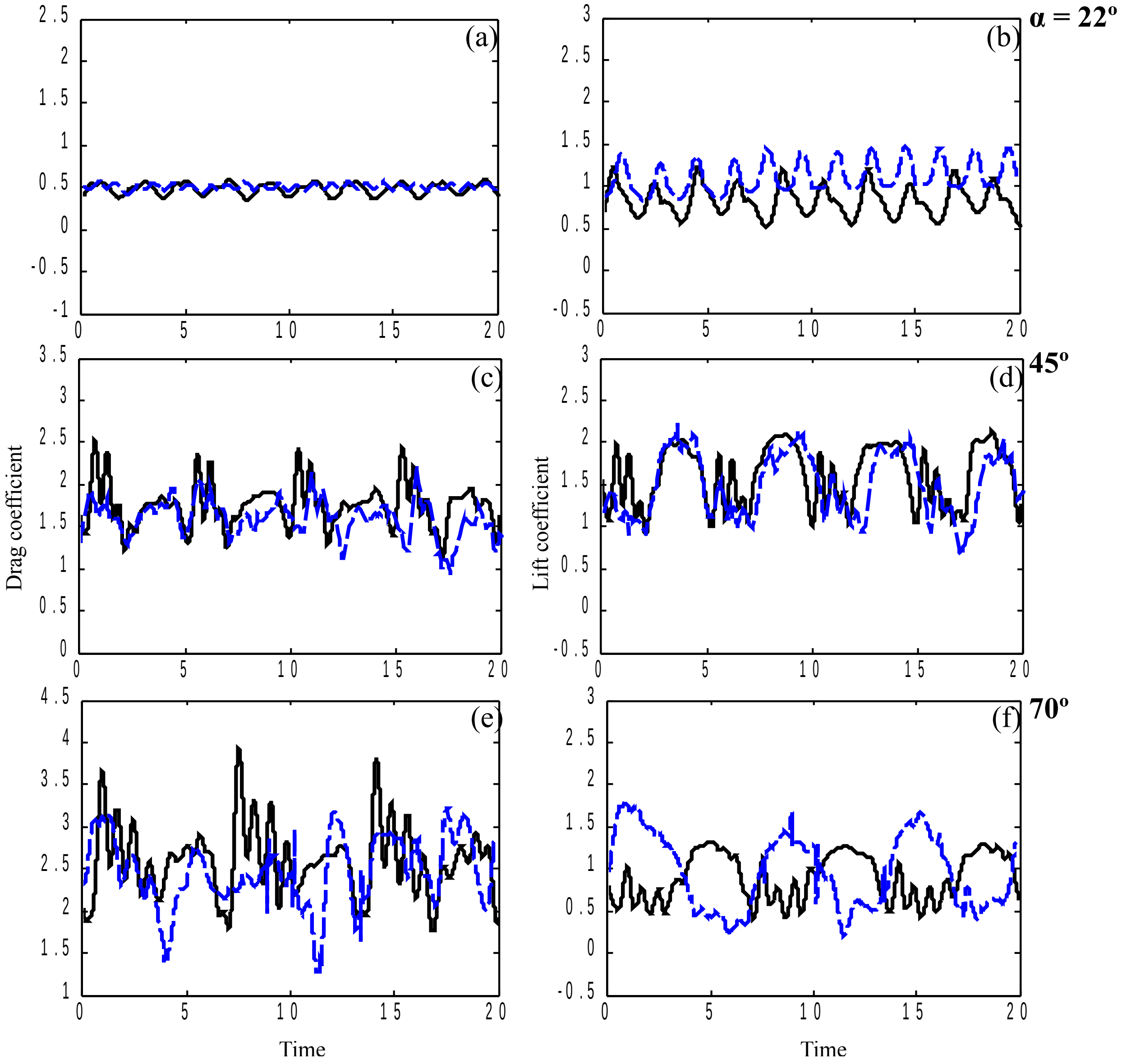

Figure 3.4: Time evolution of the drag (left) and lift (right) coefficients for an aerofoil at angles of attack 22° (top), 45° (middle) and 70° (bottom) - comparison between the cases of aerofoil without control (solid, black lines) and aerofoil with control (blue, dashed lines).

figures 3.5 (b) and 3.6 (c)) .

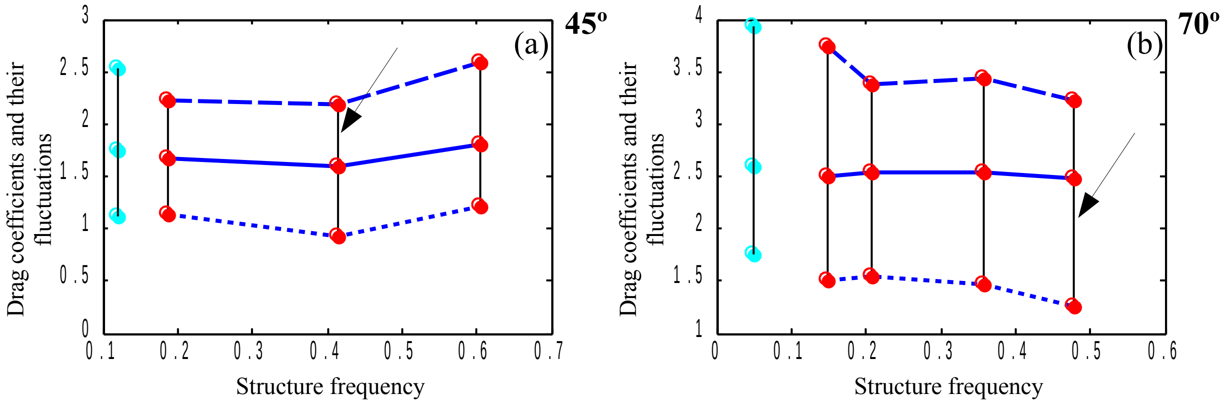

Figure 3.5: Dependence of drag on structure frequency (determined by the rigidity moment K_r) for (a) 45°, and (b) 70°. The structure frequencies are selected to match frequencies observed in the flow. The thick curves represent the mean values of drag, while the dotted curves above and below these thick curves represent the maximum and minimum values of the instantaneous drag coefficients in the course of the oscillations. The arrows point to the optimum cases shown in figure 3.4. In each of these cases, the values of minimum, mean and maximum drag for the reference case (i.e. under uncontrolled conditions) is shown by the black vertical line with cyan dots on the extreme left.

So the range of flow frequencies between 0.4 and 0.5 are probably significant to the flow (vis-a-vis the Reynolds number 1100), more than its dependence on the angle of attack. This possibly indicates that for controlling the flow at this Reynolds number, the natural structural frequency should always lie in this range of values.

From the extensive parametric study, as summarized in figures 3.5 and 3.6, it can be seen that it is very important to choose the right control parameters and some other choice is likely to yield sub-optimal results, and possibly even increase in drag and/or decrease in lift accompanied with unfavourable oscillations.

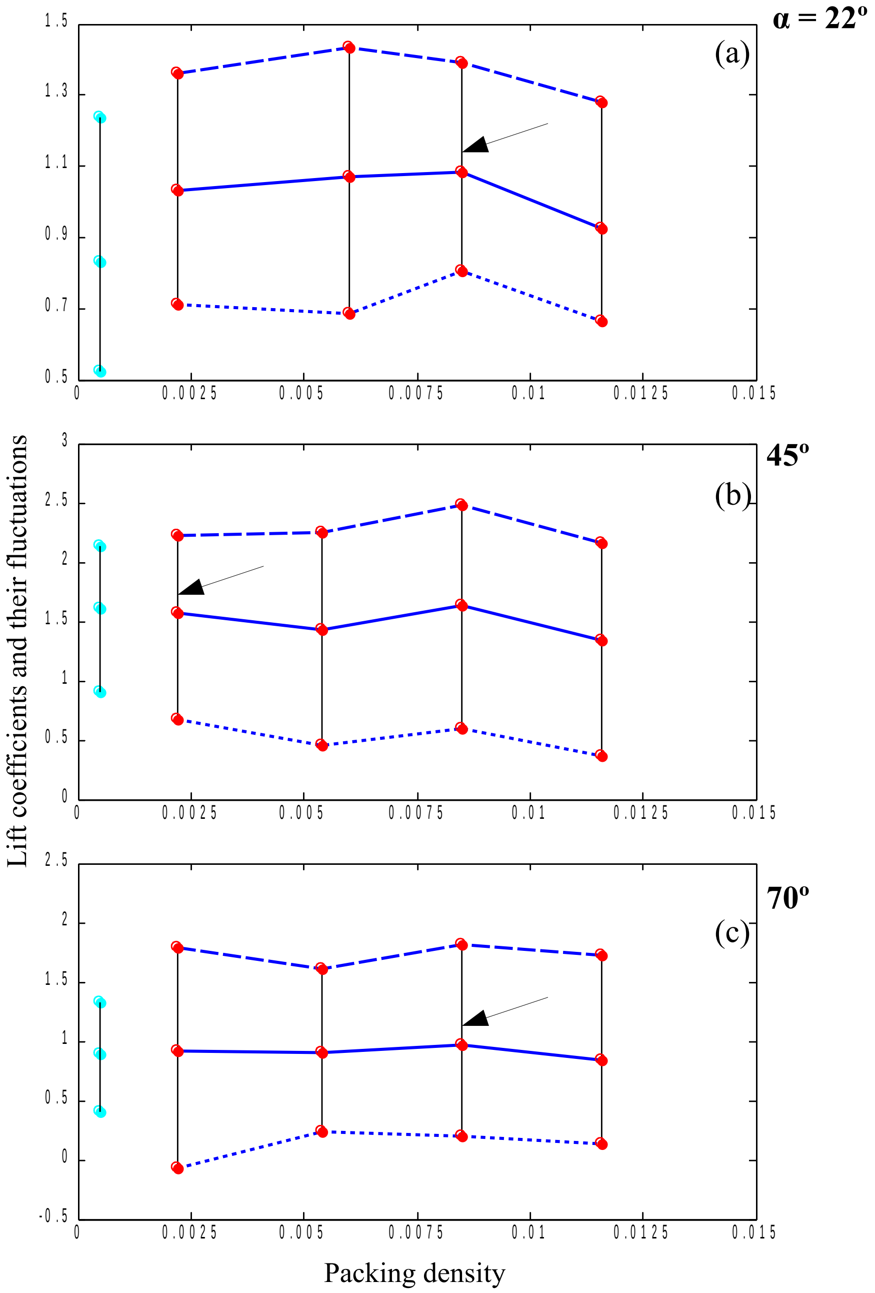

Figure 3.6: Dependence of lift as the packing density ϕ is varied over an admissible range (in accordance with Howells (1998)) for (a) 22°, (b) 45°, and (c) 70°. The thick curves represent the mean values of lift, while the dotted curves above and below these thick curves represent the maximum and minimum values of the instantaneous lift coefficients in the course of the oscillations. The arrows point to the cases shown in figure 3.4. In each of these cases, the values of minimum, mean and maximum lift for the reference case (i.e. under uncontrolled conditions) is shown by the black vertical line with cyan dots on the extreme left.

3.4.2 *Frequencies observed in the fluid-structure coupled system*

To see the effects of the control on the flow field, it is important to first analyse the frequencies in the flow for an aerodynamic body with control vis-a-vis the same aerodynamic body without any control. To do this, again a Fourier analysis is done of the controlled signals shown in figure 3.4 (depicted by blue, dashed lines).

The following observations are made for each of the cases:

In the case of an angle of attack of 22°,

(i) the dominant frequencies in the drag and lift spectra under controlled conditions are generally larger than for a smooth aerofoil;

(ii) in the spectrum of the drag signal (cf. figure 3.7 (a)), there are clusters of frequencies - comprising several frequency components close to each other and in the vicinity of a frequency with maximum amplitude. The dominant frequency (which is close to 1.2 here) is within the last such cluster. However in the lift power spectrum, such frequency clusters are absent and further, only one frequency is observed (cf. figure 3.7 (b)).

In the cases of angles 45° and 70°:

(i) the spectra of controlled drag signals show energy spread over a large frequency range (cf. figures 3.7 (c) and 3.7 (e)), as opposed to what was seen in the uncontrolled cases (cf. figures 3.3 (c) and 3.3 (e)). In the case of 45°, the range of frequencies measured is centered around the value of 0.4, which was observed to dominate in the spectrum of the uncontrolled drag signal. In the case of 70°, frequencies with values 0.303 and 0.454 are observed, each of which are close to frequencies seen in the spectrum of the uncontrolled drag signal (i.e. 0.3 and 0.45 respectively);

(ii) the spectra of controlled lift signals (cf. figures 3.7 (d) and 3.7 (f)) show one dominant frequency in each of these cases - i.e. 0.198 and 0.1515 respectively (both being close to 0.2 and 0.1477 seen in the respective spectra of lift signals in uncontrolled conditions).

Thus, these observations appear to point to a frequency lock-in, or synchronization mechanism, as outlined in Py et al. (2006).

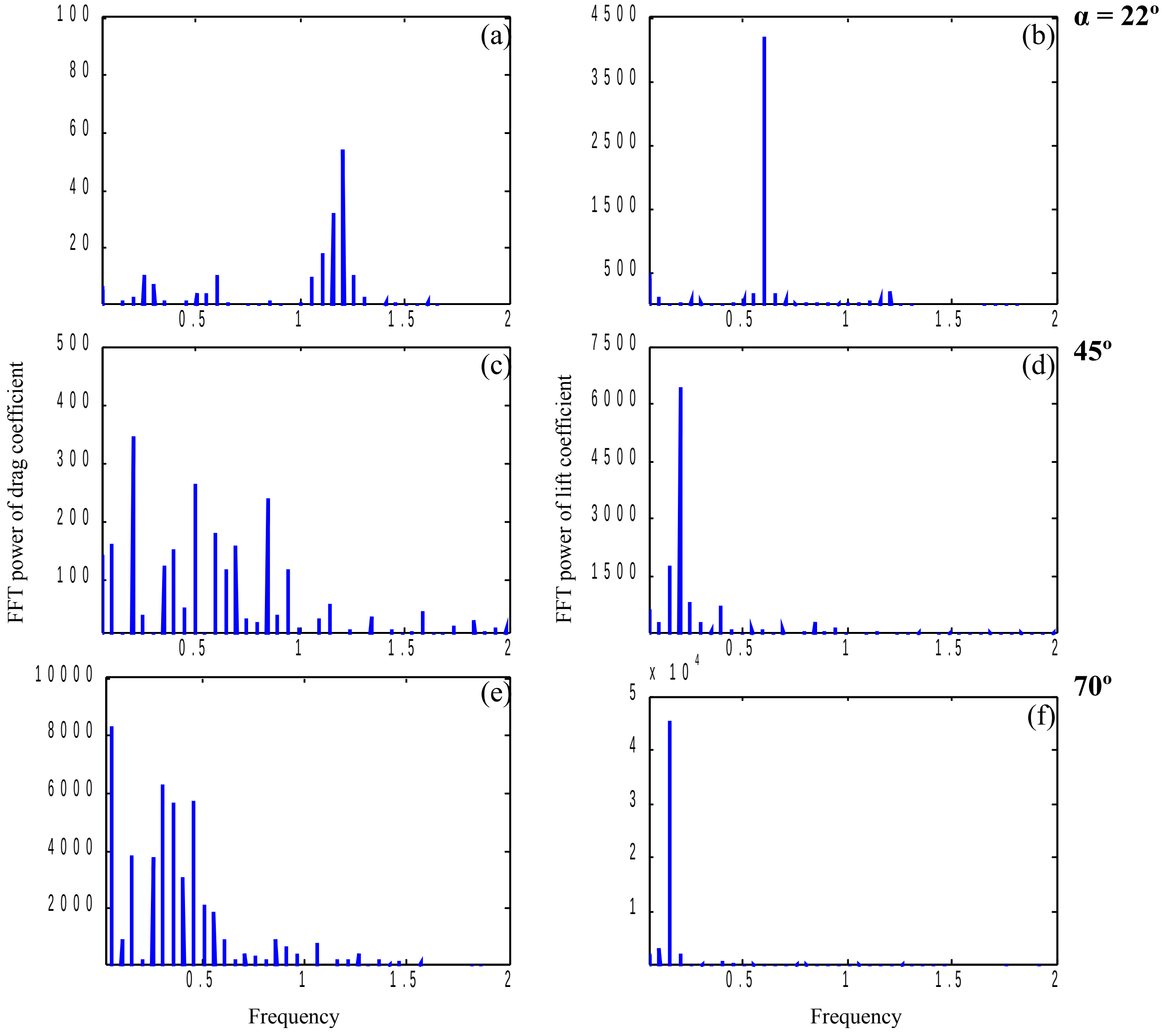

Figure 3.7: Power spectra of the drag (left) and lift (right) signals for incidence angles equal to 22° (top), 45° (middle) and 70° (bottom) when the poro-elastic, compliant coating is used, corresponding to the time signals shown in figure 3.4 (blue, dashed lines). Non-dimensional frequency is plotted along the horizontal axes.

3.4.3 *Changes in flow field close to the aerofoil*

Going beyond analysing new frequencies in the flow, we try to associate some physical implications to these by examining the flow fields (taken here to be in terms of the pressure, vorticity and wake profile) over suitable time windows, when the controlled flow, in each of the cases, has reached a statistically steady state. These time windows are precisely the ones over which the evolution of the instantaneous drag and lift coefficients are shown in figure 3.4.

(i) From the time-averaged pressure plots (cf. figure 3.8), we get information on the effect of the coating on the mean pressure field.

In the case of an incidence equal to 45°, there is a smaller mean pressure gradient as well

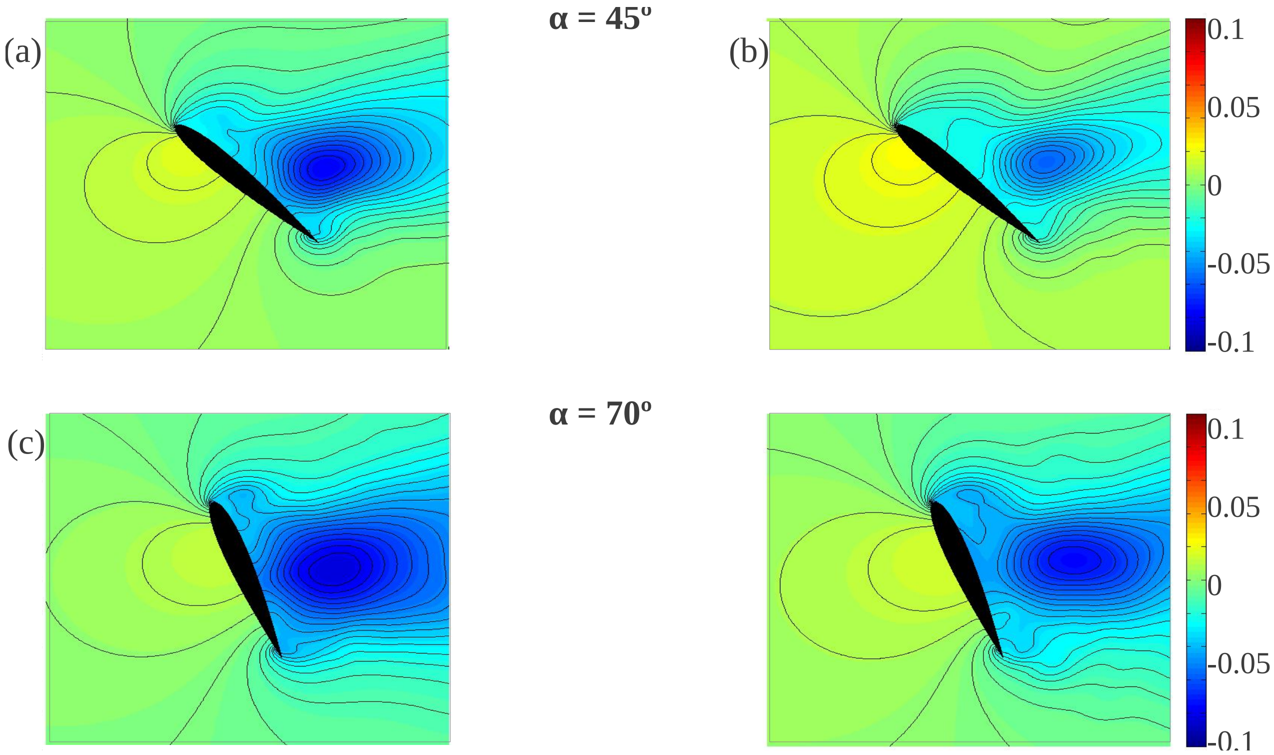

Figure 3.8: Time-averaged pressure field, depicted by isolines and colour plot for angles of attack equal to 45° (top) and 70° (bottom). The panel on the left-hand side shows the pressure field for a smooth aerofoil while that on the right-hand side is for a coated aerofoil.

as a smaller magnitude of overall mean pressure on the suction side, which contributes to reduced mean pressure drag and its fluctuations (cf. figures 3.8 (a) and (b)). This is also observed in the case of 70°, however to a lesser extent (cf. figures 3.8 (c) and (d)). In both these cases, it can also be seen that the poro-elastic layer pushes the vortex (shown by the dark blue “core”) farther away from the suction side, hence showing a modification in the vortex shedding process.

(ii) Once the vortex shedding process reaches a steady state, the vorticity field at any given instant also tells about the noteworthy contribution of the control elements.

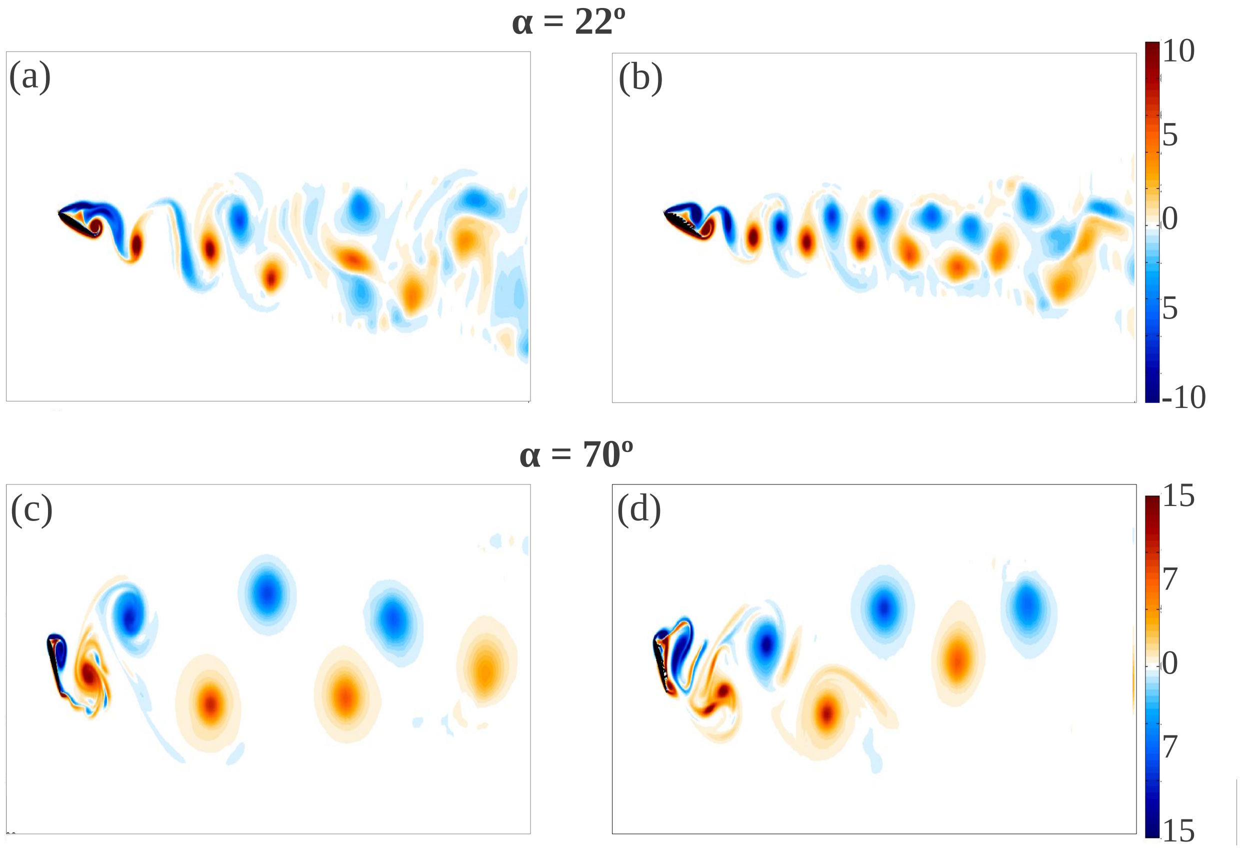

Figure 3.9: Colour plot of instantaneous vorticity field for angles of attack equal to 22° (top) and 70° (bottom). Left-hand side and right-hand side panels depict uncontrolled and controlled cases respectively. It is interesting to note that, in the presence of the coating, the shed vortices are more closely spaced than in the corresponding uncontrolled cases.

Particularly for an angle of 22° there is an increase in the intensity of the shed vortices as well as an appreciable increase in the Strouhal number (cf. figure 3.9 (a) and (b)). Some increase in the vortex intensity can also be seen for an incidence of 70° (cf. figure 3.9 (c) and (d)). This can be related to a change in the circulation around the aerofoil which in turn explains an appreciable variation in lift in both cases. Further, in the case of 22°, one also sees a noticeable regularization in the vortex shedding phenomenon and a shortening of the length scales of the vortices. In all cases it appears that the time-mean wake is narrower in the vertical direction whenever the bristles are present on the upper surface of the aerofoil, and this has a clear consequence on the integral momentum budget and, more particularly, on the drag force experienced by the aerofoil.

3.5 Conclusions

The passive control of flow on a symmetric aerofoil using a dense poro-elastic coating has been numerically studied, as a two-way coupled fluid-structure interaction problem. It is found by a numerical parametric analysis that such a coating - owing to its properties of being porous, compliant and anisotropic - is able to affect the topology of the flow in the proximity of the rear of the aerofoil, by adapting spontaneously to the separated flow. The coating modifies the vortex shedding process and also positively influences the pressure distribution, hence changing the drag and lift forces as well as their fluctuations. This is achieved by a synchronization of the oscillations of the structures onto a frequency which is comparable to the natural frequency of the fluid system.

For a very low Reynolds number flow, sets of efficient control parameters have been found over 20° to 70° range of angles of attack, where the complete behaviour from the increase to the subsequent drop of the lift coefficient with the incidence angle is observed. This wide spectrum of angles of attack is effectively captured by three angles - 22° (representing the “before-stall ”regime), 45° (representing the “near-stall ”regime) and 70° (representing the “after-stall ”regime). For instance, these passive actuators, with the right kind of properties, are capable of producing a high lift enhancement of more than 30% (for 22°) and a moderate lift increase of around 8% (for 70°); a noteworthy drag reduction of around 9% (for 45°) and a moderate drag reduction of around 5% (for 70°). In addition the drag and lift fluctuations also see positive impact.

The next two chapters proceed towards characterizing the structural properties of the poroelastic carpet, that can yield desired flow characteristics, hence leading to desired aerodynamic performance enhancement. This is achieved by examining the modifications introduced in the flow over a flat plate, which is a simpler configuration than an airfoil.

Chapter 4

Reduced order model for vortex-shedding from smooth aerofoil

Introduction

The objective of this chapter is to derive a reduced-order model for the vortex-shedding behind a symmetric aerofoil at an angle of attack to the free stream in a laminar flow regime. The derivation of such a model is a crucial preliminary step in characterizing the structural parameters of the poro-elastic layer of feathers used to coat a part of the aerofoil as in previous chapters, to obtain the desired modifications in the aerofoil's aerodynamic performance. This chapter addresses the case of the smooth aerofoil, whereas the effect of the coating will be studied in the next chapter.

To extract a reduced-order model for the phenomenon of shedding of vortices, the characteristics of vortex-shedding behind the aerofoil are analysed. Some signature of these characteristics is in fact contained in a quantity obtained by globally integrating over the computational domain - such as the lift and drag for this aerofoil. Hence, a reduced-order model will be derived for the non-dimensional lift coefficient of the aerofoil. Once the low-order model is known, the various parameters in it are appropriately selected so that results from this model match well with the computational results.

This chapter begins with an overview of some facts on non-linear dynamics in §4.1, that are used to develop the low-order model for the smooth aerofoil. In §4.2, characteristics of the time evolution of the aerofoil's (non-dimensional) lift coefficient, that go into formulating the low-order model, are highlighted. §4.3 details the development of the reduced-order model while §4.4 derives its parameters, so that the model results match with computational results. §4.5 compares the simulation results with those from the model. Finally, §4.6 presents results on some regimes of model parameters for which existence of limit cycles for the developed reduced-order model is guaranteed.

4.1 Characteristics of limit cycles

This section will highlight the characteristics of the system under consideration, particularly in the context of its similarities with non-linear dynamical systems exhibiting limit cycles:

(i) Under the reasonable assumption that the equation modeling vortex-shedding behind an aerofoil is *autonomous* (i.e, it does not depend explicitly on time), it is important to note that only those autonomous equations which have negative linear damping and positive non-linear damping are capable of producing limit cycles, since limit cycles are produced from an interplay between linear and non-linear damping terms. Thus, if there is negative linear damping in the system (which allows small perturbations to grow), then there must be at least one counter-acting positive non-linear damping term (which will push large perturbations back to the equilibrium state). This point will also be detailed in §4.3.1.

(ii) Once the flow parameters, such as the Reynolds number and the shape of the body around which the flow is occurring (in the present case, determined the parameters of the aerofoil and its angle of attack), are fixed, the long time history of the vortex-shedding from the body is periodic in the Reynolds number range of our consideration (cf. figure 4.2(a)) and independent of initial conditions. Such a system is said to be a *self-excited oscillator.*

(iii) A two-dimensional autonomous dynamical system representing a self-excited oscillator, such as the vortex-shedding behind an aerofoil (as will be illustrated in the next few sections), exhibits a Hopf bifurcation as one of its parameters that varies across a critical value. The variation of this parameter across such a critical value is often marked by the creation or annihilation of a limit cycle, which in fact appear in the system being studied. An illustration of this phenomenon, for the case of a two-dimensional dynamical system, will be presented in §4.3.1.

4.2 Characteristics of vortex-shedding from aerofoil

In order to derive the reduced-order model for vortex-shedding behind an aerofoil, the aerofoil is taken to be at an angle of attack of 10°, with streamwise Neumann outflow boundary condition at the end of the computational domain. The selection of this boundary condition ensures that no extraneous frequency enters the domain inlet (as also illustrated §2.5). A snapshot of the vortex pattern, after it has reached its steady-state, is shown in Figure 4.1.

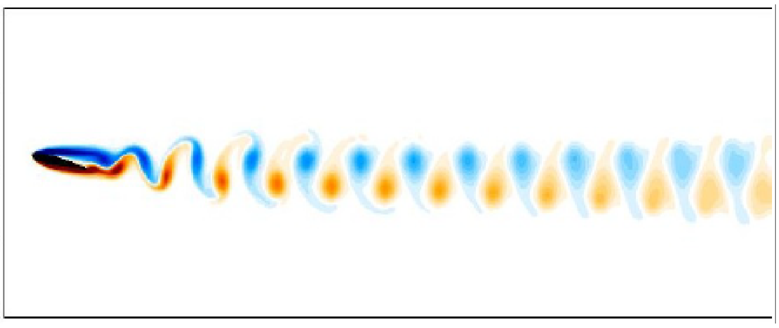

Figure 4.1: Colour plot of instantaneous vortex pattern from an aerofoil at an incidence of 10°.

To develop a low-order model for such vortex-shedding, the computational results for the time evolution of the unsteady (non-dimensional) lift coefficient and its Fourier spectrum will be considered. The characteristics of the lift coefficient for this configuration, in time and frequency domains, is shown in Figure 4.2.

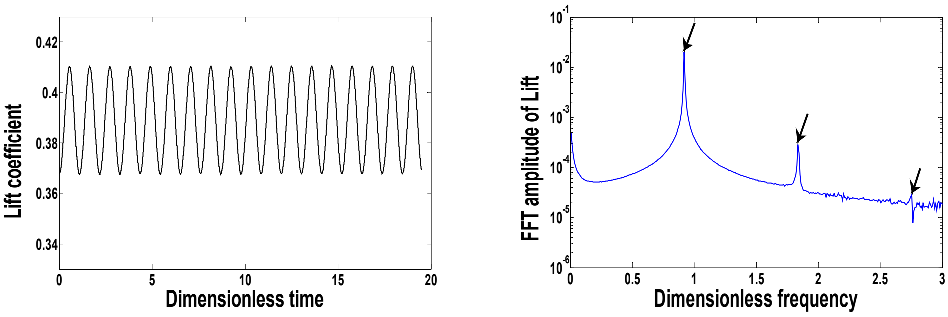

Figure 4.2: Time evolution of lift coefficient (left); Fourier spectrum of lift coefficient (right).

It can be seen from Figure 4.2(b) that after a peak at the fundamental frequency ω_s (which is in fact the frequency of vortex-shedding), there is a peak with substantial amplitude at $2\omega_s$ (followed by a smaller peak at $3\omega_s$). Such super-harmonics, where there is a larger peak at twice that of the vortex-shedding frequency, are in marked contrast to those shown by the oscillatory lift force on a stationary rigid cylinder, which shows a larger peak at three times the frequency of vortex-shedding, at Reynolds numbers of the same order as considered in this thesis [32,33]. To account for these super-harmonics of flow frequencies in the case of the aerofoil, a non-linear model consisting of at least one quadratic non-linearity must be considered.

However, an equation consisting of non-linearities of order at most two, and no higher-order non-linearities (such as cubic or higher), does not model a self-excited oscillator, since for each new initial condition, the dynamics settles down to a new closed orbit (hence showing the non-existence of a limit cycle). This point will be detailed more in §4.4.3.

4.3 Development of reduced-order model

4.3.1 Condition for existence of Hopf bifurcations

Considering that a third-order non-linearity is required in the model equation for producing a limit cycle, a *necessary* (but not *sufficient*) condition for the existence of a limit cycle is derived [34]. For this, a generic constant coefficient non-linear ordinary differential equation, with all possible quadratic and cubic non-linearities, is taken:

$$\frac{d^2x}{dt^2} + x = c\frac{dx}{dt} + \alpha_1 x^2 + \alpha_2 x\frac{dx}{dt} + \alpha_3(\frac{dx}{dt})^2 + \beta_1 x^3 + \beta_2 x^2\frac{dx}{dt} + \beta_3 x(\frac{dx}{dt})^2 + \beta_4(\frac{dx}{dt})^3 \quad (4.1)$$

where c is the coefficient of linear damping, α_i for $i = 1, 2, 3$, and β_j for $j = 1, 2, 3, 4$ are the coefficients of quadratic and cubic non-linear damping terms, respectively. It should be noted that the origin is a fixed point of this equation. The necessary condition for the existence of a limit cycle is expected to impose certain restrictions on these coefficients. For deriving this criterion, Lindstedt's method [35,36] is used, in which the basic idea is to find solutions which are periodic for *all* time, by considering the frequency as an unknown, and solving for it by imposing the requirement that the solution does not contain any secular terms. For this, firstly, the variable x is scaled to lie within a small neighbourhood around the origin, i.e, x is taken to be ϵy, where $\epsilon << 1$ and $y \sim O(1)$ is the transformed variable. Substituting this in equation (4.1) yields the following equation in terms of the variable y:

$$\frac{d^2y}{dt^2} + y = c\frac{dy}{dt} + \epsilon[\alpha_1 y^2 + \alpha_2 y\frac{dy}{dt} + \alpha_3(\frac{dy}{dt})^2] + \epsilon^2[\beta_1 y^3 + \beta_2 y^2\frac{dy}{dt} + \beta_3 y(\frac{dy}{dt})^2 + \beta_4(\frac{dy}{dt})^3] \quad (4.2)$$

To understand the relative importance of linear and non-linear damping terms, the following is done. Expanding c and y in power series in ϵ, given by $c = c_0 + c_1\epsilon + c_2\epsilon^2 + O(\epsilon^3)$ and $y = y_0 + y_1\epsilon + y_2\epsilon^2 + O(\epsilon^3)$ respectively, substituting in equation (4.2), and separating coefficients of like powers of ϵ, we get the equation at $O(1)$ to be $\frac{d^2y_0}{dt^2} + y_0 = c_0\frac{dy_0}{dt}$. Since it is known that the basic state is periodic, c_0 is set to 0 to be consistent with this. Hence, the solution y to the $O(\epsilon^0)$ approximation, y_0, is $A\cos t + B\sin t$ (where A and B are arbitrary constants determined by initial conditions). Further, the equation at $O(\epsilon)$ is given by $\frac{d^2y_1}{dt^2} + y_1 = c_1\frac{dy_0}{dt} + \alpha_1 y_0^2 + \alpha_2 y_0\frac{dy_0}{dt} + \alpha_3(\frac{dy_0}{dt})^2$. To avoid secular terms (i.e, terms growing without bound) in the $O(\epsilon)$ approximation to the solution y, c_1 must be 0. This is because the general solution for y_1 is $C\cos t + D\sin t$ (where C and D are arbitrary constants). If a term such as $c_1\frac{dy_0}{dt}$ is present, the particular solution for y_1 will have to be of the form $t(E\cos t + F\sin t)$ (where E and F are constants to be determined), making y_1 unbounded. The unboundedness of y_1 is not allowed since we have assumed in the beginning that a limit cycle exists.

Thus, the coefficient of linear damping c is scaled to $O(\epsilon^2)$, and is fixed as $c = \epsilon^2\mu$. Hence equation (4.2) now takes the form:

$$\frac{d^2y}{dt^2} + y = \epsilon[\alpha_1 y^2 + \alpha_2 y\frac{dy}{dt} + \alpha_3(\frac{dy}{dt})^2] + \epsilon^2[\mu\frac{dy}{dt} + \beta_1 y^3 + \beta_2 y^2\frac{dy}{dt} + \beta_3 y(\frac{dy}{dt})^2 + \beta_4(\frac{dy}{dt})^3] \quad (4.3)$$

To employ Lindstedt's method, the time variable is stretched and the new time variable is set as $\tau = \omega t$, where ω and $y(\tau)$ are expanded as:

$$\omega = \omega_0 + \epsilon\omega_1 + \epsilon^2\omega_2 + O(\epsilon^3); \quad y(\tau) = y_0(\tau) + \epsilon y_1(\tau) + \epsilon^2 y_2(\tau) + O(\epsilon^3) \quad (4.4)$$

It is to be noted that $\omega_0 = 1$, because when $\epsilon = 0$ the solution to equation (4.3) has a frequency of 1.

Using equation (4.4) in equation (4.3) and collecting terms proportional to $\epsilon^0(=1)$, ϵ and ϵ^2 yields the following three equations:

$$\frac{d^2y_0}{d\tau^2} + y_0 = 0; \quad (4.5)$$

$$\frac{d^2y_1}{d\tau^2} + y_1 = -2\omega_1\frac{d^2y_0}{d\tau^2} + \alpha_1 y_0^2 + \alpha_2 y_0\frac{dy_0}{d\tau} + \alpha_3(\frac{dy_0}{d\tau})^2; \quad (4.6)$$

$$\begin{aligned}\frac{d^2y_2}{d\tau^2} + y_2 = &- 2\omega_1\frac{d^2y_1}{d\tau^2} - (\omega_1^2 + 2\omega_2)\frac{d^2y_0}{d\tau^2} + 2\alpha_1 y_0 y_1 + \alpha_2\left\{y_0\frac{dy_1}{d\tau} + y_1\frac{dy_0}{d\tau} + \omega_1 y_0\frac{dy_0}{d\tau}\right\}\\ &+ \alpha_3\left\{2\frac{dy_0}{d\tau}\frac{dy_1}{d\tau} + 2\omega_1(\frac{dy_0}{d\tau})^2\right\} + \mu\frac{dy_0}{d\tau} + \beta_1 y_0^3 + \beta_2 y_0^2\frac{dy_0}{d\tau} + \beta_3 y_0(\frac{dy_0}{d\tau})^2 + \beta_4(\frac{dy_0}{d\tau})^3\end{aligned} \quad (4.7)$$

Taking the solution of equation (4.5) as $y_0(\tau) = A\cos\tau$, substituting in equation (4.6) yields the coefficient of the secular term $-2\omega_1\frac{d^2y_0}{d\tau^2}$ as $2\omega_1 A$. Thus, for the vanishing of secular terms (whose significance has been explained before equation (4.3) in this section), $\omega_1 = 0$ is needed, which gives the solution of y_1 as:

$$y_1(\tau) = \frac{A^2}{2}(\alpha_1 + \alpha_3) + \frac{A^2}{6}(\alpha_3 - \alpha_1)\cos 2\tau + \frac{A^2}{6}\alpha_2\sin 2\tau \quad (4.8)$$

Using these expressions in equation (4.7) and imposing that the coefficients of both $\sin\tau$ and $\cos\tau$ (which are obtained by collecting the appropriate parts in all the terms but the first one, in the right hand side of equation (4.7)) must vanish for no secular terms (as outlined before equation (4.3) in this section), one arrives at the following expressions for the amplitude A and frequency ω_2 respectively:

$$A = 2\sqrt{\frac{-\mu}{\alpha_2(\alpha_1+\alpha_3)+\beta_2+3\beta_4}}; \tag{4.9}$$

$$\omega_2 = \frac{\mu(10\alpha_1^2+\alpha_2^2+10\alpha_1\alpha_3+4\alpha_3^2+9\beta_1+3\beta_3)}{6\alpha_1\alpha_2+6\alpha_2\alpha_3+6\beta_2+18\beta_4} \tag{4.10}$$

It can be seen that a limit cycle for the generic dynamical system (4.1) will exist if the expression (4.9) for the amplitude A is real. For this, the linear damping coefficient μ and the quantity $\alpha_2(\alpha_1+\alpha_3)+\beta_2+3\beta_4$ must have opposite signs. Considering a situation where $\alpha_2(\alpha_1+\alpha_3)+\beta_2+3\beta_4$ is fixed, as μ varies from a positive to a negative real number, or vice-versa, a limit cycle is either born or annihilated. This is exactly the situation of a *Hopf bifurcation.* Further, system (4.1) always has a fixed point at the origin which is stable for $\mu < 0$ (case of positive linear damping) and unstable for $\mu > 0$ (case of negative linear damping). Also, in any of the cases of possible values of the coefficients of this system, exactly one from the fixed point or the limit cycle can be unstable. This is owing to the two-dimensional nature of the phase space, because trajectories which depart away the origin must approach the limit cycle and continue to stay on it forever, and conversely, trajectories that leave from the limit cycle will eventually collapse to the origin.

4.3.2 Application to the case of vortex-shedding

Since the characteristics for aerofoil vortex shedding are dependent only on the flow Reynolds number and the aerofoil's angle of attack, and not on the initial conditions, this system can be expected to exhibit a stable limit cycle. Hence from the analysis in the previous paragraph, the system has an unstable fixed point at the origin, which is possible only for $\mu > 0$ - i.e, case of negative linear damping. Based on the analysis in the previous paragraph, it is possible to deduce which non-linear terms must be present in the generic system (4.1) to yield limit cycles, independent of initial conditions.

As outlined towards the end of §4.2, in the case of vortex shedding from rigid stationary cylinders, the dominance of the third super-harmonic of the fundamental frequency over the second indicates the presence of only cubic non-linearities in the low-order model equation and no quadratic non-linearities, as studied in the past [32,33]. More generally, several authors have written about reduced-order models for vortex-shedding, particularly behind cylinders, which are standard examples of bluff bodies. While Bishop and Hassan [27] did pioneering work to model the forces over a cylinder owing to vortex-shedding using a self-excited oscillator, Hartlen and Currie [28], and Currie and Turnbull [29], formulated a model based on the Rayleigh oscillator for the forces on rigid cylinders restrained by springs in the streamwise direction but free to oscillate in the cross-flow direction, represented as:

$$\frac{d^2x}{dt^2} + x = \frac{dx}{dt} - (\frac{dx}{dt})^3 \tag{4.11}$$

Skop and Griffin [30] later used a van der Pol-like oscillator, given as:

$$\frac{d^2x}{dt^2} + x = \frac{dx}{dt} - x^2\frac{dx}{dt} \tag{4.12}$$

Nayfeh et al [37] investigated both the above wake-oscillator models to represent the lift force on a stationary cylinder. Based on an analysis of the phase differences between the first and third frequency harmonics, they arrived at the conclusion that the van der Pol oscillator (given by equation (4.12)) accurately captures the lift coefficient in the steady as well as transient states. To better approximate such phase differences between different harmonics, Akhtar et al [38] later refined this model by adding a Duffing-type of cubic non-linearity to the van der Pol oscillator model and obtained:

$$\frac{d^2x}{dt^2} + x = \frac{dx}{dt} - x^2\frac{dx}{dt} - x^3 \tag{4.13}$$

It must be noted that all the three models represented by equations (4.11), (4.12) and (4.13) satisfy the necessary condition for the existence of a limit cycle (given by equation (4.9)), thus indicating that limit cycles *can* indeed exist for all these cases. The fact that limit cycles indeed exist for these cases is proved by means of other techniques.

In the case of the aerofoil, to simplify our analysis of how the non-linearities of different orders interact with each other, exactly one of the terms of quadratic and cubic non-linearities will be taken to be non-zero. From equation (4.9), it can be seen that the coefficients β_1 and β_3 (corresponding to the non-linear terms x^3 and $x\dot{x}^2$) do not play any role for the amplitude A to be real. In fact, if exactly one of α_1, α_2 or α_3 is non-zero, and precisely one of β_1 or β_3 is non-zero (with β_2 and β_4 being zero), then equation (4.9) yields that A is infinite, thus violating the necessary condition for the existence of a limit cycle. Hence, the two non-linear terms x^3 and $x\dot{x}^2$ will be taken to be absent. The dependence of the existence of limit cycle on the coefficients α_1, α_2, α_3, β_2 and β_4 is summarised in the following table (with the linear damping coefficient μ fixed to 1):

Case	α_1	α_2	α_3	β_2	β_4	**Existence of limit cycle**
1	1	0	0	-1	0	No
2	1	0	0	0	-1	No
3	0	1	0	-1	0	Yes
4	0	1	0	0	-1	Limit cycle exists only for initial conditions with $\dot{x}$ negative or zero.
5	0	0	1	-1	0	No
6	0	0	1	0	-1	Yes

Table 4.1: Dependence of limit cycle existence on the non-linearities in equation (4.1).

From this table, it can be seen that only cases 3 and 6 yield limit cycles. A further comparative analysis of the phase portraits (i.e plots of $\dot{x}$ versus x), is presented in Figure 4.3.

It can be seen from this figure that the convergence to a limit cycle is faster in case 6, in which the non-linearities involved are $\dot{x}^2$ and $\dot{x}^3$. Our physical system is one where the limit cycle is attained fairly quickly, i.e. within a few oscillation time scales. Hence the equation taken to model the system under consideration is:

$$\frac{d^2x}{dt^2} + x = \frac{dx}{dt} + (\frac{dx}{dt})^2 - (\frac{dx}{dt})^3 \qquad (4.14)$$

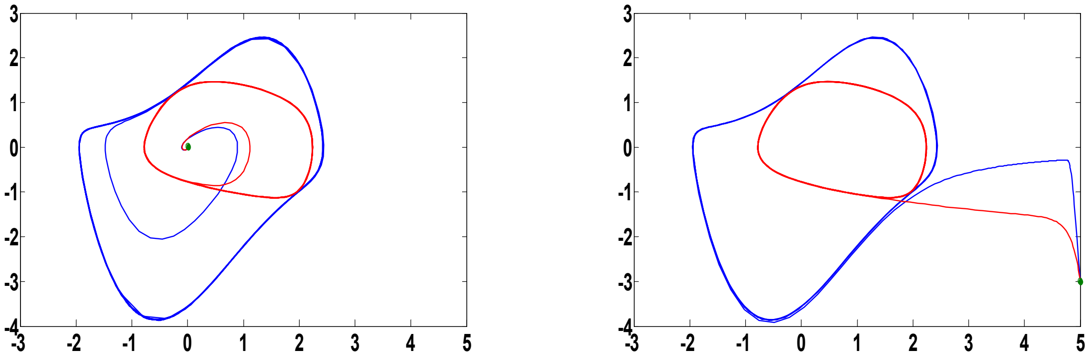

Figure 4.3: Limit cycles for cases 3 (blue curve) and 6 (red curve) of Table 4.1. The left sub-figure considers an initial condition lying within both the limit cycles, while the right sub-figure considers an initial condition lying outside both the limit cycles.

4.4 Derivation of model parameters

4.4.1 Solution by the method of multiple scales

Denoting the variable being modeled as C_L, the non-dimensional lift coefficient, the model equation, with all its unknown parameters, can be written as:

$$(\frac{d^2}{dt^2} + \omega^2)C_L = \mu\frac{d}{dt}C_L - \alpha(\frac{d}{dt}C_L)^3 + \beta(\frac{d}{dt}C_L)^2 + \omega^2 L_{mean} \tag{4.15}$$

where the parameters μ, α and β are all positive. The presence of an extra constant $\omega^2 L_{mean}$ here is to account for the fact that the mean lift coefficient C_L for an aerofoil is non-zero. To determine the parameters ω^2, μ, α and β, the analytical form of the solution for equation (4.15) is determined, which in turn is dependent on these parameters. Once the closed-form solution is known, it is matched with the simulation results (for instance, like the one showed in figure 4.2) to determine these model parameters.

Equation (4.15) will be solved by the method of multiple scales. The idea behind this method is to construct uniformly valid approximations to the solutions of perturbation problems, for small as well as large values of the independent variable. This method is pertinent in many typical perturbation problems, where solutions derived using simple perturbation expansions are meaningful only for initial short intervals of time, with the errors progressively increasing in magnitude as time progresses. This happens due to the appearance of secular terms in the solution [35,39]. This problem is eliminated in the method of multiple scales by introducing fast and slow scale variables for one independent variable (such as time t), and subsequently treating these variables as the new independent variables. This resulting additional freedom from the new independent variables is used to remove secular terms (which lead to the blow-up of solutions), by putting *solvability constraints* on the approximate solution. This procedure will be outlined in detail for solving the problem under consideration.

We consider the problem when the damping and nonlinearities are weak; that is, we take μ, α and β to be of $O(\delta)$, where $\delta << 1$ is a bookkeeping parameter. The method of multiple scales is used to determine a second-order approximate solution in δ for the lift coefficient. To achieve this, equation (4.15) is first transformed into a complex-valued first-order equation by means of the mapping $C_L(t) = \zeta(t) + \bar{\zeta}(t)$ subject to the constraint $\dot{C_L}(t) = \iota\omega[\zeta(t) - \bar{\zeta}(t)]$. This constraint means that the amplitude of $C_L(t)$ does not change with time, which is natural to impose since the objective is to arrive at a model for the steady-state vortex-shedding. Solving for ζ and $\bar{\zeta}$ yields:

$$\zeta(t) = \frac{1}{2}(C_L(t) - \frac{\iota}{\omega}\dot{C_L}(t));\ \bar{\zeta}(t) = \frac{1}{2}(C_L(t) + \frac{\iota}{\omega}\dot{C_L}(t)). \tag{4.16}$$

Differentiating the first of equations (4.16) to obtain $\ddot{C_L}(t)$ in terms of ζ, and substituting these expressions for C_L, $\dot{C_L}$ and $\ddot{C_L}$ in equation (4.15), one obtains the following first-order equation in complex variables:

$$\dot{\zeta} = \iota\omega\zeta - \frac{\iota}{2}\omega L_{mean} + \frac{\delta}{2}\mu(\zeta - \bar{\zeta}) + \frac{\delta}{2}\alpha\omega^2(\zeta^3 - 3\zeta^2\bar{\zeta} + 3\zeta\bar{\zeta}^2 - \bar{\zeta}^3) + \frac{\delta}{2}\beta\iota\omega(\zeta^2 - 2\zeta\bar{\zeta} + \bar{\zeta}^2) \tag{4.17}$$

Now, introducing the fast, slow and slower time scales given by $T_0 = t$, $T_1 = \delta t$, and $T_2 = \delta^2 t$, respectively, ζ is expanded as:

$$\zeta = \Sigma_{j=0}^{2}\delta^j\zeta_j(T_0, T_1, T_2) + O(\delta^3) \tag{4.18}$$

In terms of these three time scales, the time derivative $\frac{d}{dt}$ is given by $D_0 + \delta D_1 + \delta^2 D_2$, where $D_j = \frac{\partial}{\partial T_j}$. Substituting this expression for ζ, along with the analogous expression for $\bar{\zeta}$, in equation (4.17) and separating coefficients of powers of $\delta^0 (= 1)$, δ^1, and δ^2 yields:

$$D_0\zeta_0 - \iota\omega\zeta_0 = -\frac{\iota}{2}\omega L_{mean} \tag{4.19}$$

$$D_0\zeta_1 - \iota\omega\zeta_1 = -D_1\zeta_0 + \frac{\mu}{2}(\zeta_0 - \bar{\zeta}_0) + \frac{\alpha}{2}\omega^2(\zeta_0^3 - 3\zeta_0^2\bar{\zeta}_0 + 3\zeta_0\bar{\zeta}_0^2 - \bar{\zeta}_0^3) + \frac{\beta}{2}\iota\omega(\zeta_0^2 - 2\zeta_0\bar{\zeta}_0 + \bar{\zeta}_0^2) \tag{4.20}$$

$$\begin{aligned} D_0\zeta_2 - \iota\omega\zeta_2 = {} & -D_2\zeta_0 - D_1\zeta_1 + \frac{\mu}{2}(\zeta_1 - \bar{\zeta}_1) + \frac{3\alpha}{2}\omega^2(\zeta_0^2\zeta_1 - \zeta_0^2\bar{\zeta}_1 + \bar{\zeta}_0^2\zeta_1 - \bar{\zeta}_0^2\bar{\zeta}_1 - 2\zeta_0\bar{\zeta}_0\zeta_1 + 2\zeta_0\bar{\zeta}_0\bar{\zeta}_1) \\ & + \beta\iota\omega(\zeta_0\zeta_1 - \zeta_0\bar{\zeta}_1 - \bar{\zeta}_0\zeta_1 + \bar{\zeta}_0\bar{\zeta}_1) \end{aligned} \tag{4.21}$$

The solution for equation (4.19) is given by $\zeta_0(T_0, T_1, T_2) = A(T_1, T_2)\exp(\iota\omega T_0) + \dfrac{L_{mean}}{2}$, which on substitution in equation (4.20) yields:

$$\begin{aligned} D_0\zeta_1 - \iota\omega\zeta_1 = {} & \left\{\frac{\mu}{2}A - \frac{3\alpha}{2}\omega^2 A^2\bar{A} - \frac{\partial A}{\partial T_1}\right\}\exp(\iota\omega T_0) + \frac{\beta}{2}\iota\omega A^2\exp(2\iota\omega T_0) + \frac{\alpha}{2}\omega^2 A^3\exp(3\iota\omega T_0) \\ & + \left\{\frac{3\alpha}{2}\omega^2\bar{A}^2 A - \frac{\mu}{2}\bar{A}\right\}\exp(-\iota\omega T_0) + \frac{\beta}{2}\iota\omega\bar{A}^2\exp(-2\iota\omega T_0) - \frac{\alpha}{2}\omega^2\bar{A}^3\exp(-3\iota\omega T_0) \\ & - \beta\iota\omega A\bar{A} \end{aligned} \tag{4.22}$$

Eliminating the terms proportional to $\exp(\iota\omega T_0)$ that lead to secular terms in the solution for ζ (as explained in §4.3.1), the first solvability condition is obtained:

$$\frac{\partial A}{\partial T_1} = \frac{\mu}{2}A - \frac{3\alpha}{2}\omega^2 A^2\bar{A} \tag{4.23}$$

Thus, the solution for equation (4.22) becomes:

$$\begin{aligned} \zeta_1(T_0, T_1, T_2) = \beta A\bar{A} + \frac{\beta}{2}A^2\exp(2\iota\omega T_0) - \frac{\iota}{4}\alpha\omega A^3\exp(3\iota\omega T_0) + \left\{\frac{-\iota}{4\omega}\mu\bar{A} + \frac{3\iota}{4}\alpha\omega\bar{A}^2 A\right\}\exp(-\iota\omega T_0) \\ - \frac{\beta}{6}\bar{A}^2\exp(-2\iota\omega T_0) - \frac{\iota}{8}\alpha\omega\bar{A}^3\exp(-3\iota\omega T_0) \end{aligned} \tag{4.24}$$

Substitution of ζ_0 and ζ_1 in equation (4.21), and elimination of secular terms (as done for equation (4.22)) results in the second solvability condition:

$$\frac{\partial A}{\partial T_2} = -\frac{\iota}{8\omega}\mu^2 A + \left\{\frac{3}{4}\iota\mu\alpha\omega - \frac{2}{3}\iota\beta^2\omega\right\}A^2\bar{A} - \frac{27}{16}\iota\alpha^2\omega^3 A^3\bar{A}^2 \tag{4.25}$$

Also, from ζ_0 and ζ_1, the final solution is obtained:

$$\begin{aligned}\zeta(T_0,T_1,T_2) = {} & \frac{L_{mean}}{2} + A\exp(\iota\omega T_0) + \delta[\beta A\bar{A} \ + \frac{\beta}{2}A^2\exp(2\iota\omega T_0) \ - \ \frac{\iota}{4}\alpha\omega A^3\exp(3\iota\omega T_0) \\ & + \left\{\frac{-\iota}{4\omega}\mu\bar{A} + \frac{3\iota}{4}\alpha\omega\bar{A}^2A\right\}\exp(-\iota\omega T_0) - \frac{\beta}{6}\bar{A}^2\exp(-2\iota\omega T_0) - \frac{\iota}{8}\alpha\omega\bar{A}^3\exp(-3\iota\omega T_0)] \\ & + O(\delta^2)\end{aligned} \tag{4.26}$$

Thus $C_L(t)$, after neglecting terms of $O(\delta^2)$, is given by:

$$\begin{aligned}C_L(t) = {} & L_{mean} + A\exp(\iota\omega t) + \bar{A}\exp(-\iota\omega t) + \delta[2\beta A\bar{A} + \ \left\{\frac{\iota}{4\omega}\mu A - \frac{3\iota}{4}\alpha\omega A^2\bar{A}\right\}\exp(\iota\omega t) \\ & + \frac{\beta}{3}A^2\exp(2\iota\omega t) - \frac{\iota}{8}\alpha\omega A^3\exp(3\iota\omega t) + \left\{\frac{-\iota}{4\omega}\mu\bar{A} + \frac{3\iota}{4}\alpha\omega\bar{A}^2A\right\}\exp(-\iota\omega t) + \frac{\beta}{3}\bar{A}^2\exp(-2\iota\omega t) \\ & + \frac{\iota}{8}\alpha\omega\bar{A}^3\exp(-3\iota\omega t)]\end{aligned} \tag{4.27}$$

Also, combining the two solvability conditions from equations (4.23) and (4.25), one obtains:

$$\begin{aligned}\frac{dA}{dt} & = \delta\frac{\partial A}{\partial T_1} + \delta^2\frac{\partial A}{\partial T_2} \\ & = \delta\left\{\frac{\mu}{2}A - \frac{3\alpha}{2}\omega^2A^2\bar{A}\right\} + \delta^2\left\{-\frac{\iota}{8\omega}\mu^2A + [\frac{3}{4}\iota\mu\alpha\omega - \frac{2}{3}\iota\beta^2\omega]A^2\bar{A} - \frac{27}{16}\iota\alpha^2\omega^3A^3\bar{A}^2\right\}\end{aligned} \tag{4.28}$$

Using the polar transformation $A(t) = \frac{1}{2}a(t)\exp(\iota\gamma(t))$ in equation (4.27), the following expression is obtained for $C_L(t)$:

$$\begin{aligned}C_L(t) = L_{mean} + a(t)\cos[\omega t + \gamma(t)] \ + [\frac{\delta\beta}{2}a^2(t) + \left\{-\frac{\delta\mu}{4\omega}a(t) + \frac{3}{16}\delta\alpha\omega a^3(t)\right\}\sin[\omega t + \gamma(t)] \\ + \frac{\delta\beta}{6}a^2(t)\cos(2[\omega t + \gamma(t)]) + \frac{\delta\alpha}{32}\omega a^3(t)\sin(3[\omega t + \gamma(t)])\end{aligned} \tag{4.29}$$

This can further be simplified to:

$$\begin{aligned}C_L(t) = L_{mean} + \frac{\delta\beta}{2}a^2(t) + a(t)\sqrt{1 + [\frac{3}{16}\delta\alpha\omega a^2(t) - \frac{\delta\mu}{4\omega}]^2} \ \sin[\omega t + \gamma(t) + \eta] \\ + \frac{\delta\beta}{6}a^2(t)\cos(2[\omega t + \gamma(t)]) + \frac{\delta\alpha}{32}\omega a^3(t)\sin(3[\omega t + \gamma(t)])\end{aligned} \tag{4.30}$$

where $\eta(t) = \tan^{-1}\left\{\dfrac{16\omega}{\delta(3\alpha\omega^2 a^2(t) - 4\mu)}\right\}$. Using the polar transformation in equation (4.28) results in the following modulation equations:

$$\dot{a}(t) = \frac{\delta}{2}\{\frac{\mu}{2}a(t) - \frac{3}{8}\alpha\omega^2 a^3(t)\} \tag{4.31}$$

$$\dot{\gamma}(t) = -\delta^2\{\frac{\mu^2}{8\omega} + \frac{3}{16}\mu\alpha\omega a^2(t) - \frac{\beta^2}{6}\omega a^2(t) - \frac{27}{256}\alpha^2\omega^3 a^4(t)\} \tag{4.32}$$

Under the initial assumption that the amplitude of $C_L(t)$ does not change with time, equation (4.31) can be solved under steady-state conditions (i.e, $\dot{a}(t) = 0$). This results in two possible values of a, namely 0 and $\dfrac{2}{\omega}\sqrt{\dfrac{\mu}{3\alpha}}$. Ruling out the possibility of $a = 0$, the non-zero value of a forces the phase angle η to be $\dfrac{\pi}{2}$, and also forces the value of $\dot{\gamma}(t)$ to be $-\delta^2\{\dfrac{\mu^2}{16\omega} - \dfrac{2\beta^2\mu}{9\alpha\omega}\}$. Further, equation (4.30) now simplifies to:

$$C_L(t) = a_0 + a_1\cos(\omega_s t) + a_2\cos(2\omega_s t) + a_3\sin(3\omega_s t) \tag{4.33}$$

where:

$$a_0 = L_{mean} + \frac{2(\delta\beta)(\delta\mu)}{3(\delta\alpha)\omega^2} = L_{mean} + \frac{2\delta\beta\mu}{3\alpha\omega^2} \tag{4.34}$$

$$a_1 = \sqrt{\frac{4(\delta\mu)}{3(\delta\alpha)\omega^2}} = \sqrt{\frac{4\mu}{3\alpha\omega^2}} \tag{4.35}$$

$$a_2 = \frac{2(\delta\beta)(\delta\mu)}{9(\delta\alpha)\omega^2} = \frac{2\delta\beta\mu}{9\alpha\omega^2} \tag{4.36}$$

$$a_3 = \sqrt{\frac{(\delta\mu)^3}{432(\delta\alpha)\omega^4}} = \delta\sqrt{\frac{\mu^3}{432\alpha\omega^4}} \tag{4.37}$$

$$\omega_s = \omega - \frac{(\delta\mu)^2}{16\omega} - \frac{2(\delta\beta)^2(\delta\mu)}{9(\delta\alpha)\omega} = \omega - \frac{(\delta\mu)^2}{16\omega} - \frac{2(\delta\beta)^2\mu}{9\alpha\omega} \tag{4.38}$$

It must be noted that equations (4.34) and (4.38) yield $a_0 \sim L_{mean}$ and $\omega_s \sim \omega$, respectively. Further a_2 and a_3 are both of $O(\delta)$, while a_1 is of $O(1)$. These observations mean that the time evolution of the lift coefficient has a sufficiently large *primary* component with an average approximately equal to L_{mean} and frequency ω_s approximately equal to the frequency ω of the *restoring force* in the dynamical system.

4.4.2 Model parameters from simulation results

In the previous subsection, given the model parameters ω, μ, α and β, the form of the limit cycle of the non-linear system (4.15) was derived. Conversely, when the computational results are known - i.e, the characteristics of the limit cycle are known in terms of the quantities a_0, a_1, a_2, a_3 and ω_s are known, the model parameters can be calculated using equations (4.34)-(4.38) to arrive at the best possible fit for the numerical data. These parameters are given as:

$$\omega = \frac{a_1^2 a_3 \omega_s}{a_1^2 a_3 - 36a_3^3 - 6a_2^2 a_3} \tag{4.39}$$

$$\delta\mu = \frac{24 a_1 a_3^2 \omega_s}{a_1^2 a_3 - 36a_3^3 - 6a_2^2 a_3} \tag{4.40}$$

$$\delta\alpha = \frac{32(a_1^2 a_3 - 36a_3^3 - 6a_2^2 a_3)}{a_1^5 \omega_s} \tag{4.41}$$

$$\delta\beta = \frac{6a_2}{a_1^2} \tag{4.42}$$

It should be noted that all the linear and nonlinear damping parameters are of $O(\delta)$, as was the original assumption (mentioned before equation (4.16)) for solving this problem. Further, the sign of β is always positive, since it involves only products and quotients of amplitudes. This implies that in our system, there is always negative quadratic damping. Further, the signs of μ and α are identical, and dependent on the sign of the term $a_1^2 a_3 - 36a_3^3 - 6a_2^2 a_3$, since the terms $24a_1 a_3^2 \omega_s$ and $a_1^5 \omega_s$ are always positive. If $a_1^2 a_3 - 36a_3^3 - 6a_2^2 a_3$ is positive, then, according to equation (4.15), there will be negative linear damping and positive cubic damping, a configuration which leads to the existence of a limit cycle, provided cubic damping is dominant over quadratic damping. This is an instance where energy pumped in the form of small disturbances from equilibrium are allowed to grow due to the characteristics of linear damping, while large disturbances are pushed back to equilibrium because of non-linear damping. However, if $a_1^2 a_3 - 36a_3^3 - 6a_2^2 a_3$ is negative, then there will be positive linear damping and negative non-linear damping (both cubic as well as quadratic), a case in which a limit cycle can not exist. In other words, a system with a limit cycle that exhibits exactly one fundamental frequency and its super-harmonics, and for which $a_1^2a_3 - 36a_3^3 - 6a_2^2a_3$ is negative, would not be well represented by the reduced-order model presented above.

4.4.3 Requirement of cubic or higher odd-order non-linearities

As remarked in §4.2, if a generic equation with all three quadratic non-linearities, and no higher order non-linearities (such as cubic and higher), is solved by the method of multiple scales (as presented in §4.4.1), the amplitude of the fundamental frequency in the solution is seen to be dependent on the initial condition. Thus, it is not possible for such an equation to have a limit cycle. This observation indicates that some cubic or higher order non-linearity is required in the model for a limit cycle to exist.

4.5 Comparison with simulation results

From Figure 4.1(b) which shows the Fourier spectrum of the lift coefficient, one gets the following values for the fundamental frequency ω_s, amplitudes corresponding to the fundamental frequency a_1, to twice the fundamental frequency a_2, and to three times the fundamental frequency a_3:

$$\omega_s = 2\pi \times 0.9222 = 5.7944 \;\; ; \;\; a_1 = 0.02119 \;\; ; \;\; a_2 = 3.46 \times 10^{-4} \;\; ; \;\; a_3 = 1.9 \times 10^{-5}. \tag{4.43}$$

Substituting these values in equations (4.39) to (4.42), we get the following values of the model parameters for equation (4.15):

$$\omega = 5.8039 \;\; ; \delta\mu = 0.1249 \;\; ; \delta\alpha = 11.0102 \;\; ; \delta\beta = 4.6234. \tag{4.44}$$

Again substituting these parameters in the model equation (4.15) and by numerically solving it, we can compare this solution with the simulation results, as done in Figure (4.4).
It can be seen that the simulation results and results from the model agree very well with each other, both in time as well as frequency domains.

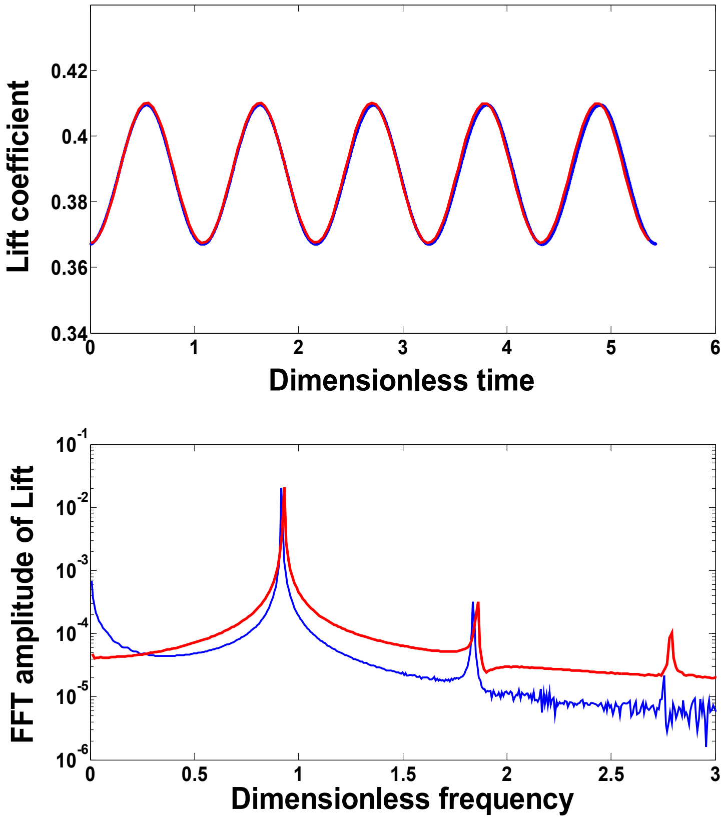

Figure 4.4: Comparison of model and simulation results of lift coefficient - the blue curve shows the simulation results while the red curve shows results from the model. The top and bottom sub-figures show comparisons in time and frequency domains respectively.

Further, figures 4.5 and 4.6 show two typical cases of initial conditions, outside and inside the (unique) limit cycle respectively.

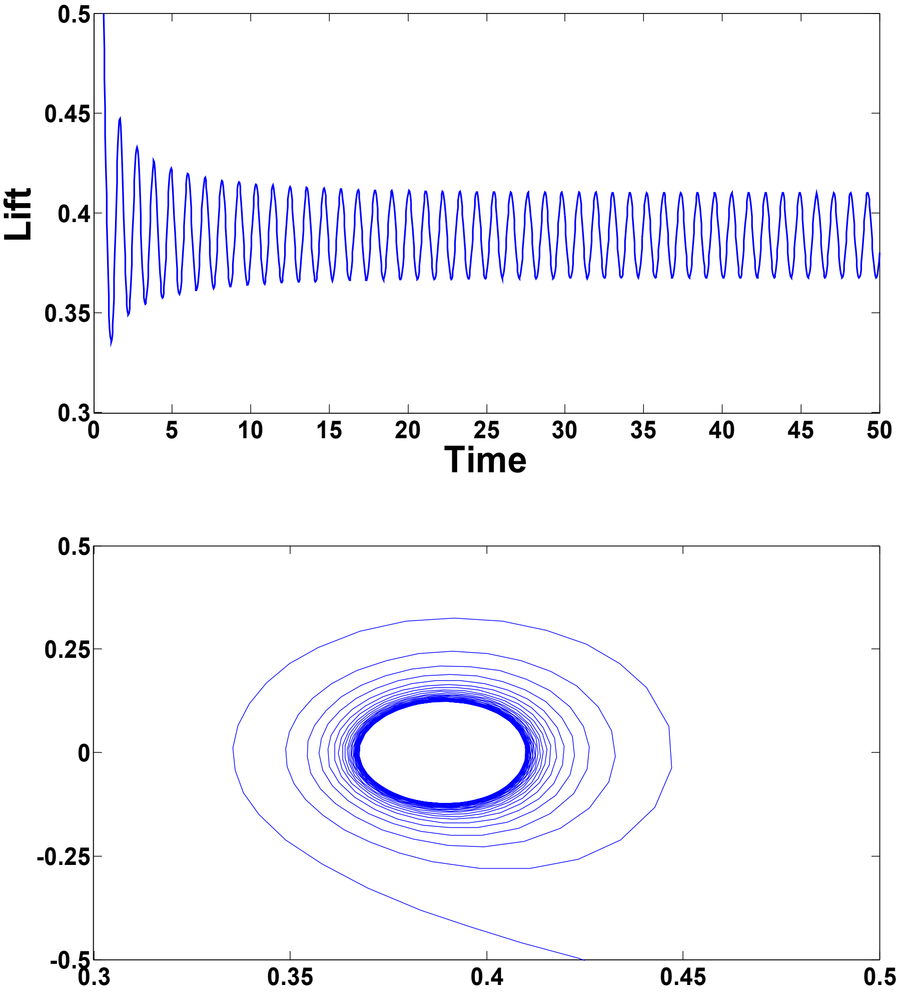

Figure 4.5: Convergence of numerical integration of the model equation from an initial condition **outside** the limit cycle. The top and bottom sub-figures show the time trace and the phase portrait, respectively.

It can be seen that in figure 4.5, beginning from a large initial condition far away from the limit cycle, the trajectory ultimately narrows and converges to the limit cycle.

In the case of figure 4.6, a small initial condition gradually expands and reaches the limit cycle as a steady state. Hence the steady-state solution is indeed independent of the initial

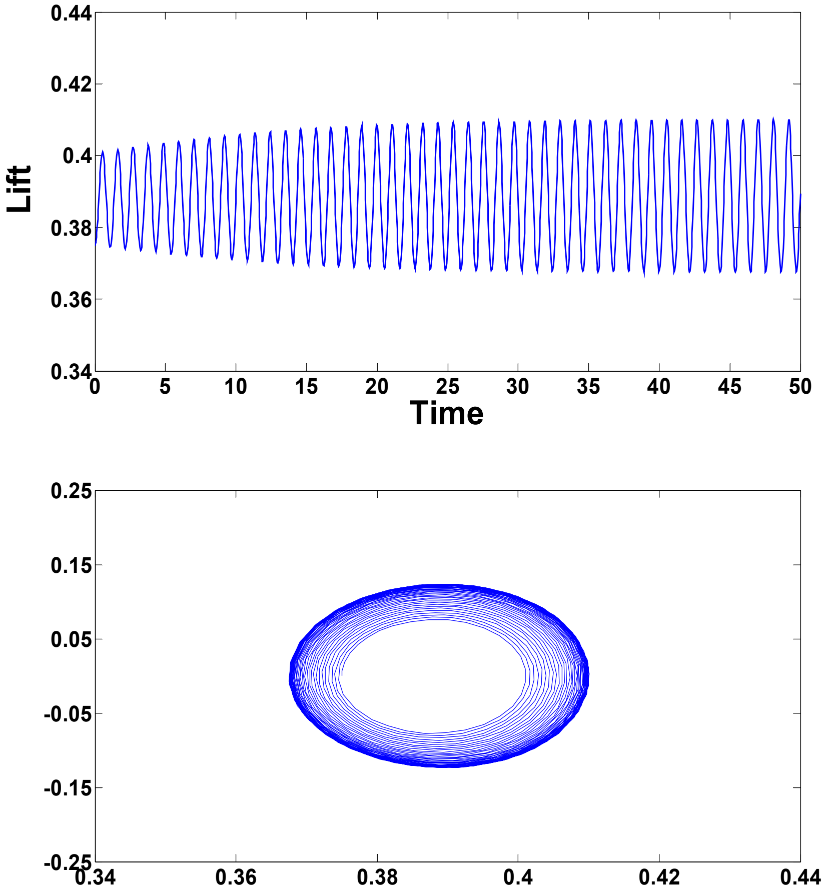

Figure 4.6: Convergence of numerical integration of the model equation from an initial condition **inside** the limit cycle. The top and bottom sub-figures show the time trace and the phase portrait, respectively.

conditions.

All of these results indicate the effectiveness of the reduced-order model for vortex-shedding behind a (smooth) aerofoil.

4.6 Parameter regimes for existence of limit cycles

From the closed-form solution derived for the limit cycle of the dynamical system (4.15), as given by equations (4.33) to (4.38), it is also possible to segregate values of model parameters for which limit cycles exist or for which their characteristics possibly change. In this thesis, the space which is analysed for regimes of limit cycle existence is three dimensional and parametrized by the three damping parameters - μ (linear), α (cubic) and β (quadratic). It must be noted that the analytical expression (4.33) for the limit cycle is meaningful only when its amplitude a_1, and will change if frequency ω_s changes its sign.

As outlined in the beginning of §4.4.1, since μ and α are positive, the expression for the amplitude a_1, given by (4.35) (which shows that a_1 is dependent only on μ and α, for a fixed ω), yields that it is always positive. Figure 4.7 shows contour isolines of the amplitude a_1 when μ and α are varied. As predicted by formula (4.35), the sizes of limit cycles scale proportionately to $\frac{\mu}{\alpha}$. Further, for an increase in a_1 (which is the size of the limit cycle), it can be seen that, eventually, the effect of increase in μ dominates that of increase in α. Hence the size of the limit cycle increases at the rate of $\sqrt{\mu}$.

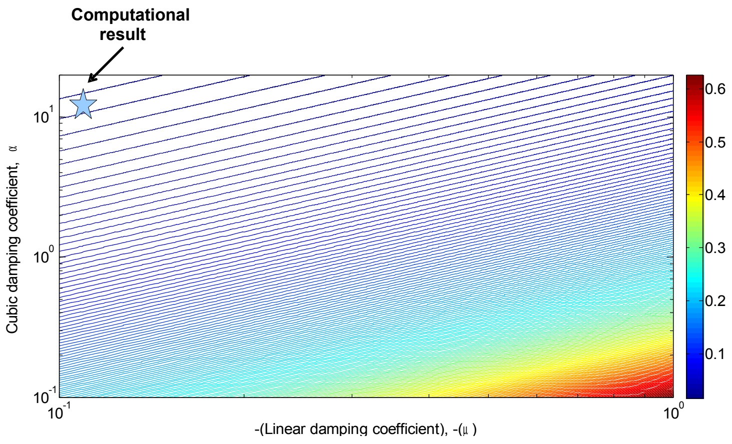

Figure 4.7: Dependence of the amplitude of limit cycle a_1 on the linear and cubic damping parameters, μ and α respectively, as given by equation (4.34), when the coefficient of restoring force ω is fixed to the value 5.8039 (as given by equation (4.43)). The star shows the parameters at which the reduced-order model yields the solution that matches with the computational results, as shown in figure 4.4.

As opposed to the case of the size of the limit cycle, wherein a_1 is always positive, it is possible to have positive values of μ, α and β for which the frequency ω_s is negative. An illustration of this feature is given in figure 4.8, where the three dimensional parameter space of μ, α and β is segregated into spaces where limit cycles can change their characteristics (shown by dotted lines dividing the parameter space into two parts, with the arrow pointing in the direction of the part where ω_s is positive). As illustrated before in figure 4.7, the stars in each of these panels show the parameters with which the reduced-order model yields the solution that matches with the computational results (shown in figure 4.4).

From the top panel of figure 4.8, it can be seen that for μ above a certain *threshold* value, lying between 0.1 and 1 but closer to 1, α must also proportionately be *above* some threshold for the frequency ω_s to be a positive number, hence guaranteeing the existence of a limit cycle. Further, the frequency scales proportionately to $\frac{\mu}{\alpha}$, as predicted by formula (4.37). In the case of the joint dependence of ω_s on μ and β, it can be seen from the middle panel that for μ above a certain *threshold* value slightly higher than 10, α must be proportionately *below* some threshold, to guarantee a limit cycle. Finally, in the case of the joint dependence of ω_s on α and β, as depicted in the bottom panel of figure (4.8), limit cycles can not exist if α is very small and β is very large. The quadratic damping should proportionately be *below* a certain threshold so that the two nonlinear damping terms interact optimally and force the trajectory escaping from an initial condition back into a limit cycle.

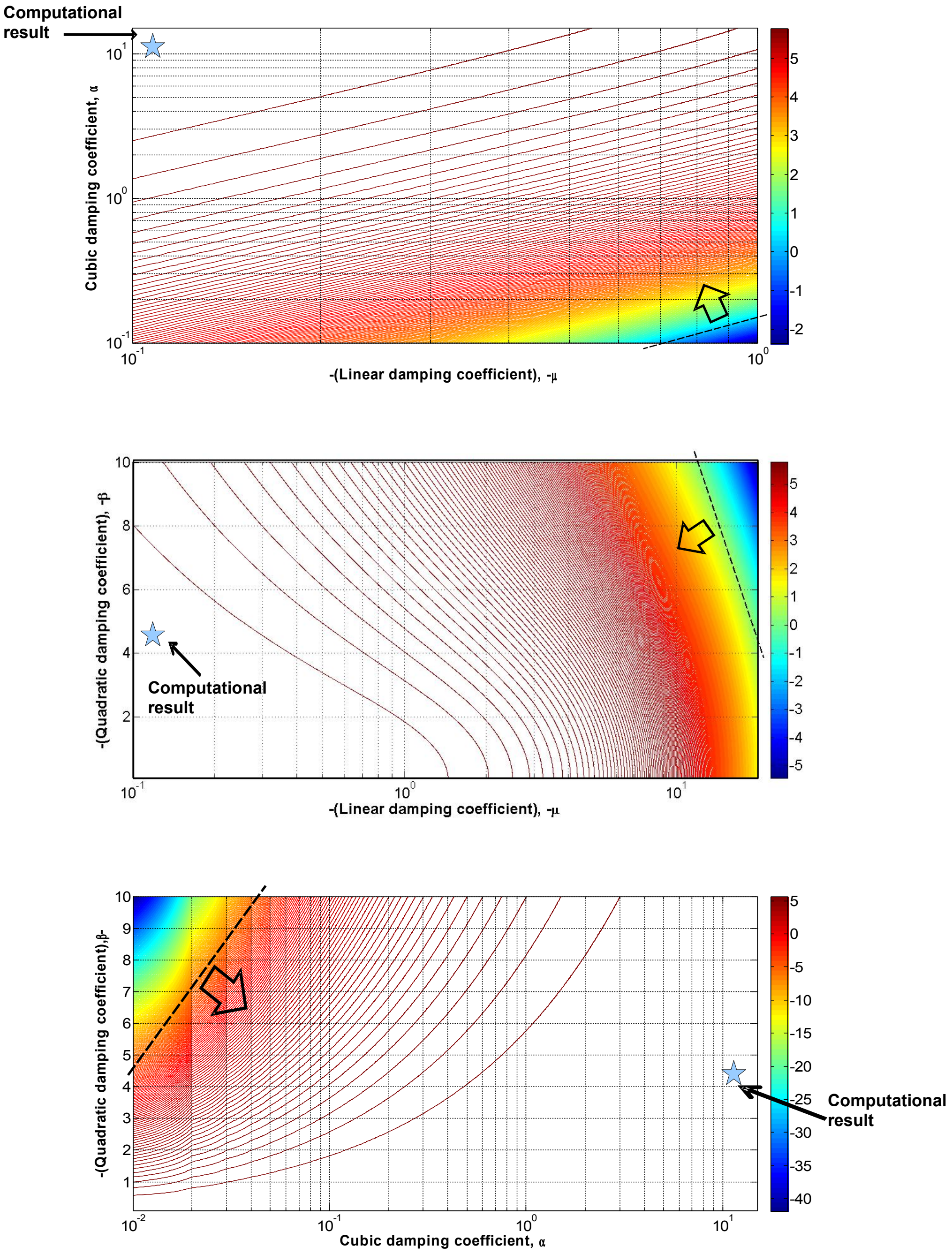

Figure 4.8: Dependence of the frequency of limit cycle ω_s on the damping parameters when the coefficient of restoring force ω is fixed to the value given by equation (4.43). The top, middle and bottom panels show the dependence of ω_s on the linear and cubic damping coefficients μ and α, linear and quadratic damping coefficients μ and β, and, cubic and quadratic damping coefficients α and β, respectively, when β, α and μ are fixed to the values given by equation (4.43), in each of the cases.

4.7 Conclusions

A reduced-order model for vortex-shedding behind an aerofoil at an angle of incidence to the free-stream, such as the cases studied in Chapter 3, has been developed. To achieve this, the characteristics of a globally integrated quantity such as the lift coefficient of the aerofoil (that contains the signature of the characteristics of vortex-shedding at various streamwise locations behind the aerofoil,) are analysed.

When the Fourier spectrum of the lift coefficient for this configuration is analysed, amplitude peaks are noted at a fundamental frequency (which is also the frequency of vortex-shedding) and its higher harmonics, particularly its second and third superharmonic in decreasing order of amplitudes. To account for these features in the dynamics, a non-linear model with exactly one quadratic and one cubic non-linearity each is developed. This is achieved by analysing various possibilities of non-linear models with quadratic and cubic non-linearities, and whether they have trajectories converging to (unique) limit cycles. Once the model is developed, it is noted that it exhibits a Hopf bifurcation as one of its parameters (in particular, the coefficient of linear damping) changes its sign. It is further demonstrated that this model (with fixed model parameters) yields a unique limit cycle (irrespective of the initial condition from which the trajectory is integrated).

For the non-linear model developed for the lift coefficient, a closed-form expression for its limit cycle is derived in terms of generic (unknown) model parameters, using the method of multiple scales. By comparing the various characteristics of this analytical expression for the limit cycle (such as its amplitude at various frequencies and its fundamental frequency) with the characteristics of the periodic solution obtained from simulations, the model parameters are determined in terms of the computational features. The trajectory obtained from this non-linear model with these model parameters is seen to match the trajectory obtained from computations very well, not only in the time domain but also in the frequency domain. Finally, regimes of model parameters which will yield unique limit cycles for this non-linear model are illustrated.

All of the above observations indicate the effectiveness of the reduced-order model.

Chapter 5

Coupled reduced order model for aerofoil with poro-elastic coating

Introduction

The objective of this chapter is to characterise the structural parameters of the poro-elastic layer of feathers, which is used to coat the suction side of the aerofoil as in Chapters 2 and 3, to obtain desired modifications in the aerofoil's aerodynamic performance, carrying forward the work presented in Chapter 4. To achieve this, the reduced-order model for the same aerofoil, this time coated with a poro-elastic layer of compliant feathers, is obtained. This model is realised by coupling the low-order model for a smooth aerofoil with a certain number of linear damped oscillators, a non-linear analog of which was described in §2.7.2. Structure parameters, which should, as well as, should not be used for this passive flow control technique, are rigorously derived.

This chapter begins with a derivation of the closed-form expression for the solution of such a coupled system in §5.1. This is followed by derivations for the model parameters in terms of simulation results in §5.2, along the lines of how this was done in Chapter 4. §5.3 presents an overview of simulations performed, to arrive at the reduced-order model. In order to better understand the physics, the first part of this section presents results from prototype simulations, obtained by considering the flow over a flat plate, both aligned with the free-stream as well as oriented at an incidence angle to it. The second part of this section presents results for the case of the symmetric aerofoil (considered throughout in this thesis) at an angle of attack to the free stream, and correlates the results for the flat plate with those of the aerofoil, thus presenting reasons for developing the specific reduced-order model for the coupled system. §5.4 compares the simulation results for the aerofoil with those obtained from the model (as outlined in §5.1 and §5.2), hence proving its effectiveness.

5.1 Linear reduced-order model with linear coupling: derivation of solution

To follow the simplest approach, we consider the reduced-order model for the feathery coating as a linear spring, denoted by the equation of a linear damped oscillator:

$$\ddot{\theta} + c\dot{\theta} + \omega_1^2\theta = 0 \tag{5.1}$$

where θ denotes the angular displacement of a reference feather (as explained in §2) about its angular mean/equilibrium position θ_{eq}, c is the dissipation constant and ω_1 is the spring constant. When this is coupled with the reduced-order model for vortex-shedding behind a smooth aerofoil (as captured by the reduced-order model for the aerofoil's lift by equation (4.15) in Chapter 4), the coupled system is given by:

$$\ddot{C_L} + \omega^2 C_L - \omega^2 L_{mean} - \mu\dot{C_L} + \alpha(\dot{C_L})^3 - \beta(\dot{C_L})^2 = \rho_1\theta \tag{5.2}$$

$$\ddot{\theta} + c\dot{\theta} + \omega_1^2\theta = \rho_2(C_L - L_{mean}) \tag{5.3}$$

where ρ_1 and ρ_2 are constants for linear coupling between the independent fluid and structure systems.

As done in §4.4.1, this coupled system can also be solved by the method of multiple scales [35,39], to find the general form of the solution, C_L and θ, in terms of the model parameters (similar to equations (4.32)-(4.37)). Conversely, given the form of the solution (for instance from the computational data, as in the present case), it is possible to find the model parameters in terms of the numerical/physical characteristics of the computations (similar to equations (4.38)-(4.41)). In addition, if the fluid model parameters ω^2, μ, α and β are fixed (for flow under certain fixed conditions), as in the present case, it is also possible to compute "optimal" structure model parameters to yield desired behaviour for the solution of the coupled system.

Following the method outlined in §4.4.1, we consider the coupled problem when the damping and nonlinearities for the fluid problem, the damping/dissipation for the structure problem as well as the coupling between the fluid and structure parts are weak; i.e, we take μ, α, β, c, ρ_1 and ρ_2 all to be of $O(\delta)$, where $\delta << 1$ is a bookkeeping parameter. To determine a second-order approximate solution in δ for the lift coefficient and the angular displacement of the reference feather, equations (5.2) and (5.3) are transformed into complex-valued first-order equations by using $C_L(t) = \zeta_1(t) + \bar{\zeta}_1(t)$ subject to the constraint $\dot{C}_L(t) = \iota\omega[\zeta_1(t) - \bar{\zeta}_1(t)]$, and $\theta(t) = \zeta_2(t) + \bar{\zeta}_2(t)$ subject to the constraint $\dot{\theta}(t) = \iota\omega[\zeta_2(t) - \bar{\zeta}_2(t)]$. These equations now respectively take the form:

$$\begin{aligned}\dot{\zeta}_1 = \iota\omega\zeta_1 - \frac{\iota}{2}\omega L_{mean} + \frac{\delta}{2}\mu(\zeta_1 - \bar{\zeta}_1) + \frac{\delta}{2}\alpha\omega^2(\zeta_1^3 - 3\zeta_1^2\bar{\zeta}_1 + 3\zeta_1\bar{\zeta}_1^{\,2} - \bar{\zeta}_1^{\,3}) \\ + \frac{\delta}{2}\beta\iota\omega(\zeta_1^2 - 2\zeta_1\bar{\zeta}_1 + \bar{\zeta}_1^{\,2}) - \frac{\delta}{2\omega}\iota\rho_1(\zeta_2 + \bar{\zeta}_2)\end{aligned} \tag{5.4}$$

$$\dot{\zeta}_2 = \iota\omega_1\zeta_2 - \frac{\delta}{2}c(\zeta_2 - \bar{\zeta}_2) - \frac{\delta}{2\omega}\iota\rho_2(\zeta_1 + \bar{\zeta}_1) + \frac{\delta}{2\omega_1}\iota\rho_2 L_{mean} \tag{5.5}$$

Introducing the fast, slow and slower time scales given by $T_0 = t$, $T_1 = \delta t$, and $T_2 = \delta^2 t$, respectively, using the expansions:

$$\zeta_1 = \Sigma_{j=0}^2 \delta^j \zeta_{1,j}(T_0, T_1, T_2) + O(\delta^3); and \tag{5.6}$$

$$\zeta_2 = \Sigma_{j=0}^2 \delta^j \zeta_{2,j}(T_0, T_1, T_2) + O(\delta^3), \tag{5.7}$$

transforming equations (5.4) and (5.5) in these terms, and separating coefficients of powers of $\delta^0 (= 1)$, δ^1, and δ^2 yields the following three ordinary differential equations for ζ_1:

$$D_0\zeta_{1,0} - \iota\omega\zeta_{1,0} = -\frac{\iota}{2}\omega L_{mean} \tag{5.8}$$

$$
\begin{aligned}
D_0\zeta_{1,1} - \iota\omega\zeta_{1,1} = -D_1\zeta_{1,0} + \frac{\mu}{2}(\zeta_{1,0} - \bar{\zeta}_{1,0}) &+ \frac{\alpha}{2}\omega^2(\zeta_{1,0}^3 - 3\zeta_{1,0}^2\bar{\zeta}_{1,0} + 3\zeta_{1,0}\bar{\zeta}_{1,0}^2 - \bar{\zeta}_{1,0}^3) \\
&+ \frac{\beta}{2}\iota\omega(\zeta_{1,0}^2 - 2\zeta_{1,0}\bar{\zeta}_{1,0} + \bar{\zeta}_{1,0}^2) - \frac{\iota\rho_1}{2\omega}(\zeta_{2,0} + \bar{\zeta}_{2,0})
\end{aligned} \tag{5.9}
$$

$$
\begin{aligned}
D_0\zeta_{1,2} - \iota\omega\zeta_{1,2} = &- D_2\zeta_{1,0} - D_1\zeta_{1,1} + \frac{\mu}{2}(\zeta_{1,1} - \bar{\zeta}_{1,1}) + \frac{3\alpha}{2}\omega^2(\zeta_{1,0}^2\zeta_{1,1} - \zeta_{1,0}^2\bar{\zeta}_{1,1} + \bar{\zeta}_{1,0}^2\zeta_{1,1} - \bar{\zeta}_{1,0}^2\bar{\zeta}_{1,1} \\
&- 2\zeta_{1,0}\bar{\zeta}_{1,0}\zeta_{1,1} + 2\zeta_{1,0}\bar{\zeta}_{1,0}\bar{\zeta}_{1,1}) + \beta\iota\omega(\zeta_{1,0}\zeta_{1,1} - \zeta_{1,0}\bar{\zeta}_{1,1} - \bar{\zeta}_{1,0}\zeta_{1,1} + \bar{\zeta}_{1,0}\bar{\zeta}_{1,1}) \\
&- \frac{\iota\rho_1}{2\omega}(\zeta_{2,1} + \bar{\zeta}_{2,1})
\end{aligned} \tag{5.10}
$$

and the following three ordinary differential equations for ζ_2:

$$
D_0\zeta_{2,0} - \iota\omega_1\zeta_{2,0} = 0 \tag{5.11}
$$

$$
D_0\zeta_{2,1} - \iota\omega_1\zeta_{2,1} = -D_1\zeta_{2,0} - \frac{c}{2}(\zeta_{2,0} - \bar{\zeta}_{2,0}) - \frac{\iota\rho_2}{2\omega_1}(\zeta_{1,0} + \bar{\zeta}_{1,0} - L_{mean}) \tag{5.12}
$$

$$
D_0\zeta_{2,2} - \iota\omega_1\zeta_{2,2} = -D_2\zeta_{2,0} - D_1\zeta_{2,1} - \frac{c}{2}(\zeta_{2,1} - \bar{\zeta}_{2,1}) - \frac{\iota\rho_2}{2\omega_1}(\zeta_{1,1} + \bar{\zeta}_{1,1}) \tag{5.13}
$$

Solving the system of equations (5.8)-(5.10) for ζ_1 (by combining the solutions for $\zeta_{1,0}$, $\zeta_{1,1}$, $\zeta_{1,2}$) and the system (5.11)-(5.13) for ζ_2 (by combining the solutions for $\zeta_{1,0}$, $\zeta_{1,1}$, $\zeta_{1,2}$), as done in §4.4.1, yields:

$$
\begin{aligned}
\zeta_1(T_0, T_1, T_2) = &\frac{L_{mean}}{2} + A_1e^{\iota\omega T_0} + \delta[\beta A_1\bar{A}_1 \ + \frac{\beta}{2}A_1^2e^{2\iota\omega T_0} \ - \ \frac{\iota}{4}\alpha\omega A_1^3e^{3\iota\omega T_0} \\
&+ \left\{\frac{-\iota}{4\omega}\mu\bar{A}_1 + \frac{3\iota}{4}\alpha\omega\bar{A}_1{}^2A_1\right\}e^{-\iota\omega T_0} - \frac{\beta}{6}\bar{A}_1{}^2e^{-2\iota\omega T_0} - \frac{\iota}{8}\alpha\omega\bar{A}_1{}^3e^{-3\iota\omega T_0} \\
&+ \frac{\rho_1}{2\omega}(\frac{A_2}{\omega - \omega_1}e^{\iota\omega_1T_0} + \frac{\bar{A}_2}{\omega + \omega_1}e^{-\iota\omega_1T_0})] + O(\delta^2)
\end{aligned} \tag{5.14}
$$

$$
\zeta_2(T_0, T_1, T_2) = A_2e^{\iota\omega_1T_0} + \delta[\frac{\iota c}{4\omega_1}\bar{A}_2e^{-\iota\omega_1T_0} - \frac{\rho_2}{2\omega_1}(\frac{A_1}{\omega - \omega_1}e^{\iota\omega T_0} - \frac{\bar{A}_1}{\omega + \omega_1}e^{-\iota\omega T_0})] + O(\delta^2) \tag{5.15}
$$

Equations (5.14) and (5.15) can be recast to obtain the analytical expressions for $C_L(t)$ and $\theta(t)$ (as done to obtain equation (4.27) from equation (4.26) in section §4.4.1). In addition, the following solvability conditions are obtained by eliminating the secular terms (that occur in the course of solving for the bounded solutions ζ_1 and ζ_2):

$$
\frac{\partial A_1}{\partial T_1} = \frac{\mu}{2}A_1 - \frac{3\alpha}{2}\omega^2A_1^2\bar{A}_1 \tag{5.16}
$$

$$\frac{\partial A_2}{\partial T_1} = -\frac{c}{2} A_2 \tag{5.17}$$

$$\frac{\partial A_1}{\partial T_2} = -\frac{\iota}{8\omega}\mu^2 A_1 + \left\{\frac{3}{4}\iota\mu\alpha\omega - \frac{2}{3}\iota\beta^2\omega\right\} A_1^2 \bar{A}_1 - \frac{27}{16}\iota\alpha^2\omega^3 A_1^3 \bar{A}_1{}^2 + \frac{\iota\rho_1\rho_2 A_1}{2\omega(\omega-\omega_1)(\omega+\omega_1)} \tag{5.18}$$

$$\frac{\partial A_2}{\partial T_2} = -\frac{\iota}{8\omega_1} c^2 A_2 - \frac{\iota\rho_1\rho_2 A_2}{2\omega_1(\omega-\omega_1)(\omega+\omega_1)} \tag{5.19}$$

Using the polar transformations $A_1(t) = \frac{1}{2}a_1(t)e^{\iota\gamma_1(t)}$ and $A_2(t) = \frac{1}{2}a_2(t)e^{\iota\gamma_2(t)}$ in the expressions for $C_L(t)$ and $\theta(t)$ respectively, one obtains the following closed-form solutions:

$$\begin{aligned} C_L(t) = L_{mean} &+ \frac{\delta\beta}{2}a_1^2(t) + a_1(t)\sqrt{1 + [\frac{3}{16}\delta\alpha\omega a_1^2(t) - \frac{\delta\mu}{4\omega}]^2} sin[\omega t + \gamma_1(t) + \eta_1] \\ &+ \frac{\delta\beta}{6}a_1^2(t) cos(2[\omega t + \gamma_1(t)]) + \frac{\delta\alpha}{32}\omega a_1^3(t) sin(3[\omega t + \gamma_1(t)]) \\ &+ \frac{\delta\rho_1}{(\omega-\omega_1)(\omega+\omega_1)} a_2(t) cos[\omega_1 t + \gamma_2(t)] \end{aligned} \tag{5.20}$$

$$\theta(t) = a_2(t)\sqrt{1 + \frac{\delta^2 c^2}{16\omega_1^2}} sin[\omega_1 t + \gamma_2(t) + \eta_2] - \frac{\delta\rho_2}{(\omega-\omega_1)(\omega+\omega_1)} a_1(t) cos[\omega t + \gamma_1(t)] \tag{5.21}$$

where $\eta_1(t) = tan^{-1}\left\{\frac{16\omega}{\delta(3\alpha\omega^2 a_1^2(t) - 4\mu)}\right\}$ and $\eta_2(t) = tan^{-1}\left\{\frac{4\omega_1}{c}\right\}$.
Combining the solvability conditions (5.16) and (5.18) and using the polar transformation $A_1(t) = \frac{1}{2}a_1(t)e^{\iota\gamma_1(t)}$, we obtain the following modulation equations:

$$\dot{a}_1(t) = \frac{\delta}{2}\left\{\frac{\mu}{2}a_1(t) - \frac{3}{8}\alpha\omega^2 a_1^3(t)\right\} \tag{5.22}$$

$$\dot{\gamma}_1(t) = -\delta^2\left\{\frac{\mu^2}{8\omega} + \frac{3}{16}\mu\alpha\omega a_1^2(t) - \frac{\beta^2}{6}\omega a_1^2(t) - \frac{27}{256}\alpha^2\omega^3 a_1^4(t) - \frac{\rho_1\rho_2}{2\omega(\omega-\omega_1)(\omega+\omega_1)}\right\} \tag{5.23}$$

Similarly, combining the solvability conditions (5.17) and (5.19) and using the polar transformation $A_2(t) = \frac{1}{2}a_2(t)e^{\iota\gamma_2(t)}$, we obtain the following modulation equations:

$$\dot{a}_2(t) = -\frac{\delta}{2} c a_2(t) \tag{5.24}$$

$$\dot{\gamma}_2(t) = -\delta^2\left\{\frac{\iota c^2}{8\omega_1} + \frac{\rho_1\rho_2}{2\omega_1(\omega-\omega_1)(\omega+\omega_1)}\right\} \tag{5.25}$$

Again under the initial assumption that $C_L(t)$ and $\theta(t)$ both have reached their steady states and hence, do not vary with time, equations (5.22) and (5.24) can be solved under steady-state conditions (i.e, $\dot{a_1}(t)$ and $\dot{a_2}(t)$ are both zero.) This results in two possible values of a_1, namely 0 and $\frac{2}{\omega}\sqrt{\frac{\mu}{3\alpha}}$ (exactly as in the calculations in §4.4.1). Further, the only possibilities for steady-state condition for $a_2(t)$ are $c = 0$ or $a_2(t) = 0$. The possibility of *both* $a_1(t) = 0$ and $a_2(t) = 0$ can be ruled out, because if it were true, then it means that the whole coupled system has no dynamics in the steady state. The other three cases are:

Case 1: $a_1(t) = \frac{2}{\omega}\sqrt{\frac{\mu}{3\alpha}}$ **and** $a_2(t) \equiv 0$**.** The possibility of $a_2(t)$ being *identically zero* physically means that the dissipation constant c of the reference feather is allowed to be *arbitrarily large*, and hence, the oscillations of the *independent* structure part die out almost instantly after they begin. As a result, for this case, in the two-way coupled fluid-structure system, the dynamics of the structure part happens exactly at the same frequency as that of the fluid part, this frequency being given by $\omega_{s,1} = \omega + \gamma_1$ (as calculated below).
Also, the non-zero value of a_1 forces the phase angle η_1 to be $\frac{\pi}{2}$, and

$$\dot{\gamma_1}(t) = -\delta^2 \left\{ \frac{\mu^2}{16\omega} - \frac{2\beta^2\mu}{9\alpha\omega} - \frac{\rho_1\rho_2}{2\omega(\omega-\omega_1)(\omega+\omega_1)} \right\} \tag{5.26}$$

Further, as $c \to \infty$, $\eta_2 \to 0$ and $\dot{\gamma_2}(t) \to \infty$. Thus, equation (5.20) *degenerates* to an equation similar in form to (4.33) (but with a different ω_s, as given below), while (5.21) simplifies to:

$$\theta(t) = -\frac{2\delta\rho_2}{\omega(\omega-\omega_1)(\omega+\omega_1)}\sqrt{\frac{\mu}{3\alpha}} cos(\omega_{s,1}t) \tag{5.27}$$

where $\omega_{s,1} = \omega - \frac{(\delta\mu)^2}{16\omega} - \frac{2(\delta\beta)^2\mu}{9\alpha\omega} - \frac{(\delta\rho_1)(\delta\rho_2)}{2\omega(\omega-\omega_1)(\omega+\omega_1)}$.
It must be noted that with such a coating, the lift of the aerofoil $C_L(t)$, under steady-state conditions, displays exactly the same characteristics in its dynamics (such as the presence of second and third super-harmonics of the fundamental frequency $\omega_{s,1}$) as in the case when the aerofoil was not coated with any feathers. However, the angular displacement of the feather $\theta(t)$ exhibits just one frequency, equal to the fundamental frequency $\omega_{s,1}$, in its dynamics.

Case 2: $a_1(t) \equiv 0$ and $c = 0$. In this case, owing to the fact that the dissipation constant c is zero, $a_2(t)$, in its steady state, is allowed to be an *arbitrary* constant C_0, either small or large. This case turns out to be similar to case 1, where the dynamics of the fluid and structure parts happen at the same frequency, now given by $\omega_{s,2} = \omega_1 + \gamma_2$ (as calculated below).

Also, since $a_1(t) \equiv 0$, $\eta_1 = tan^{-1}(\frac{-4\omega}{\delta\mu})$ whose limit is $\frac{\pi}{2}$ as $\delta \to 0$. Further, $\dot{\gamma_1}(t) = -\delta^2\left\{\frac{\mu^2}{8\omega} - \frac{\rho_1\rho_2}{2\omega(\omega-\omega_1)(\omega+\omega_1)}\right\}$. Besides, since $c = 0$, $\eta_2 = \frac{\pi}{2}$ and

$$\dot{\gamma_2}(t) = -\delta^2\left\{\frac{\rho_1\rho_2}{2\omega_1(\omega-\omega_1)(\omega+\omega_1)}\right\} \tag{5.28}$$

Thus, equation (5.20) simplifies to:

$$C_L(t) = L_{mean} + \frac{\delta\rho_1 C_0}{(\omega-\omega_1)(\omega+\omega_1)}cos(\omega_{s,2}t) \tag{5.29}$$

while equation (5.21) simplifies to:

$$\theta(t) = C_0 cos(\omega_{s,2}t) \tag{5.30}$$

where $\omega_{s,2}$ is given by $\omega_1 - \frac{(\delta\rho_1)(\delta\rho_2)}{2\omega_1(\omega-\omega_1)(\omega+\omega_1)}$.

In this case, it must be noted that both the dynamics of the lift $C_L(t)$ as well as angular displacement of the feather $\theta(t)$ exhibit dynamics at the same frequency $\omega_{s,2}$, and *no* superharmonics are observed in either of these dynamics.

Case 3: $a_1(t) = \frac{2}{\omega}\sqrt{\frac{\mu}{3\alpha}}$ and $c = 0$. In this case, equation (5.20) simplifies to:

$$C_L(t) = L_{mean} + \frac{2\delta\beta\mu}{3\alpha\omega^2} + \sqrt{\frac{4\mu}{3\alpha\omega^2}}cos(\omega_{s,1}t) + \frac{2\delta\beta\mu}{9\alpha\omega^2}cos(2\omega_{s,1}t) + \delta\sqrt{\frac{\mu^3}{432\alpha\omega^4}}sin(3\omega_{s,1}t) + \frac{\delta\rho_1 C_0}{(\omega-\omega_1)(\omega+\omega_1)}cos(\omega_{s,2}t) \tag{5.31}$$

while equation (5.21) simplifies to:

$$\theta(t) = C_0 cos(\omega_{s,2}t) - \frac{2\delta\rho_2}{\omega(\omega-\omega_1)(\omega+\omega_1)}\sqrt{\frac{\mu}{3\alpha}}cos(\omega_{s,1}t) \tag{5.32}$$

where $\omega_{s,1}$ and $\omega_{s,2}$ are given as before from cases 1 and 2 respectively.
Here, it can be seen that, in general, $\omega_{s,1}$ and $\omega_{s,2}$ are two *distinct* frequencies. Hence, in this case, the two-way coupled fluid-structure interaction displays very rich dynamics, where for one frequency, super-harmonics can be observed, while for the other, no such super-harmonics can be seen.

In all of the above three cases, we can have the possibilities of at least one of $\omega_{s,1}$ or $\omega_{s,2}$ being zero. It is very important to note that if $\omega_{s,1}$ is zero, then so is $\omega_{s,2}$ and vice-versa. This is because if $\omega_{s,1}$ is zero (in which case, $\omega_s = \dfrac{(\delta\rho_1)(\delta\rho_2)}{2\omega(\omega-\omega_1)(\omega+\omega_1)}$, where it must be recalled that ω_s is the vortex-shedding frequency for the smooth aerofoil), the right-hand side of the above condition must be of $O(1)$, since the left-hand side ω_s is of $O(1)$. This is possible only if $\omega \sim \omega_1$, which is nothing but the *resonant* condition for the coupled fluid-structure system. Under this condition, it can be easily seen that $\omega_{s,2}$ is also zero, since $\omega_1 = \dfrac{(\delta\rho_1)(\delta\rho_2)}{2\omega_1(\omega-\omega_1)(\omega+\omega_1)}$ by similar order of magnitude analysis, as presented above. The other possibility is the *non-resonant* condition, where both $\omega_{s,1}$ or $\omega_{s,2}$ are non-zero.

Case of resonant frequencies, $\omega \sim \omega_1$: In these circumstances, for all of cases 1, 2 and 3, mean lift can be increased by a small amount. In fact, only for cases 2 and 3, this can be achieved by increasing the structure-fluid coupling parameter ρ_1 or, the steady state oscillations of the feather C_0. The *optimal* selection of such an ω_1 will be presented in future work.

Case of non-resonant frequencies: Under these conditions, for case 1, the oscillations can be neither increased nor decreased. For case 2, the oscillations can be decreased if the structure and coupling parameters are selected to satisfy $\dfrac{\delta\rho_1 C_0}{(\omega-\omega_1)(\omega+\omega_1)} < \sqrt{\dfrac{4\mu}{3\alpha\omega^2}}$. For case 3, however, if such a condition is true, then the lift fluctuations about the mean lift is dominated by $\sqrt{\dfrac{4\mu}{3\alpha\omega^2}}$, and therefore, the use of such feathers cannot decrease the lift fluctuations. However, the use of feathers which should *never* be used, in order to avoid increase of lift fluctuations, is governed by the condition $\dfrac{\delta\rho_1 C_0}{(\omega-\omega_1)(\omega+\omega_1)} > \sqrt{\dfrac{4\mu}{3\alpha\omega^2}}$.

5.2 Structure and coupling parameters from simulation results

The calculations in this section are analogous to the calculations done in §4.4.2 (where the model parameters for a smooth aerofoil were derived in terms of the characteristics of the simulation results for the smooth aerofoil). Thus, the aim in this section is to derive the fluid parameters ω, μ, α, β; the structure parameters ω_1 and c; and the fluid-structure coupling parameters ρ_1 and ρ_2; in terms of the characteristics of the simulation results for the poro-elastically coated aerofoil, so that a best possible fit for the numerical data is obtained.

If one considers the most generic analytical form of the solution for the lift coefficient $C_L(t)$ and the angular displacement of the reference feather θ, given by equations (5.20) and (5.21), it can be seen that under steady state assumptions for the amplitudes of $C_L(t)$ and θ, these equations reduce to equations (5.31) and (5.32). Equations (5.31) and (5.32) are now rephrased as:

$$C_L(t) = l_0 + l_1 cos(\omega_{s,1}t) + l_2 cos(2\omega_{s,1}t) + l_3 sin(3\omega_{s,1}t) + l_1^{'} cos(\omega_{s,2}t) \tag{5.33}$$

$$\theta(t) = \theta_1 cos(\omega_{s,2}t) + \theta_1^{'} cos(\omega_{s,1}t) \tag{5.34}$$

where $l_0 \sim L_{mean}$ and l_1, l_2, l_3, $l_1^{'}$, $\omega_{s,1}$, θ_1, $\theta_1^{'}$ and $\omega_{s,2}$ are eight quantities which can be recovered from computational data; and depend on the eight unknown model parameters ω, $\delta\mu$, $\delta\alpha$, $\delta\beta$, $\delta\rho_1$, ω_1, δc (or equivalently C_0) and $\delta\rho_2$. Hence, solving for these unknowns yields the following two coupled quadratic equations for ω and ω_1:

$$(l_1^2 l_3 - 36 l_3^3 - 6 l_2^2 l_3)\omega^2 - l_1^2 l_3 \omega_{s,1}\omega - l_1^2 l_3 \omega_1^2 + l_1^2 l_3 \omega_{s2}\omega_1 = 0 \tag{5.35}$$

$$(2\theta_1 l_1 - l_1^{'}\theta_1^{'})\omega_1^2 - 2\omega_{s,2}\theta_1 l_1 \omega_1 + l_1^{'}\theta_1^{'}\omega^2 = 0\ ; \tag{5.36}$$

and the following six equations for the remaining parameters:

$$\delta\mu = \frac{24 l_3 \omega}{l_1} \tag{5.37}$$

$$\delta\alpha = \frac{32 l_3}{l_1^3 \omega} \tag{5.38}$$

$$\delta\beta = \frac{6 l_2}{l_1^2} \tag{5.39}$$

$$C_0 = \theta_1 \tag{5.40}$$

$$\delta\rho_1 = \frac{(\omega - \omega_1)(\omega + \omega_1) l_1'}{C_0} \tag{5.41}$$

$$\delta\rho_2 = \frac{-\omega(\omega - \omega_1)(\omega + \omega_1)\theta_1'}{2}\sqrt{\frac{3\alpha}{\mu}} \tag{5.42}$$

It must be noted here that equations (5.37) and (5.38) involve ω while equations (5.41) and (5.42) involve both ω as well as ω_1, which can be solved from the coupled system of quadratic equations (5.35) and (5.36).

5.3 Overview of simulations

5.3.1 Prototype simulations: Case of flat plate

Case A: Flat plate aligned with the free-stream

In order to relate the theoretical results obtained in §5.1 and §5.2 to the simulation results for the symmetric aerofoil (presented in the second part of this section), the flow configuration is simplified from the case of flow over an aerofoil, at an angle of incidence to the free-stream, to the case of flow over a flat plate aligned with the free-stream. The flat plate considered for these prototype simulations is shown in figure 5.1. The flat plate simulations developed here provide a good prototype flow for us to understand the mechanisms of lift enhancement or drag reduction. Such a detailed study is being carried out now and will be presented in future work.

A flat plate at zero angle of attack, without any poro-elastic coating has no mean lift (which is also confirmed from simulations), owing to the fact that for such a symmetric configuration, the flow, and hence also the pressure distribution, above and below the flat plate are identical. To see what changes are introduced in the flow by using the poro-elastic coating, the flat plate is coated with such flow-compliant feathers towards the end of its top side, as shown by the schematic diagram in figure 5.1. As explained before in §2.7, since the rigidity moment is taken to dominate the angular dynamics of the feathers, the dimensionless *linear* structure frequency is taken to be the dimensionless *linear* rigidity frequency (non-dimensionalised by the time scale given by the ratio between the free-stream speed and the length of the flat plate, which in this case is 1.65), and is given by $\frac{1}{2\pi \times 1.65}\sqrt{\frac{K_r}{Ml_c^2}}$, where the non-dimensional values for K_r, M and l_c are 8.33, 5.5 and 8.5×10^{-2} respectively. The normalisation procedure followed here is exactly the same as that followed in §3.2 and tables 3.1 and 3.2. In the present case, this dimensionless linear structure frequency f_s is taken to be 0.4594.

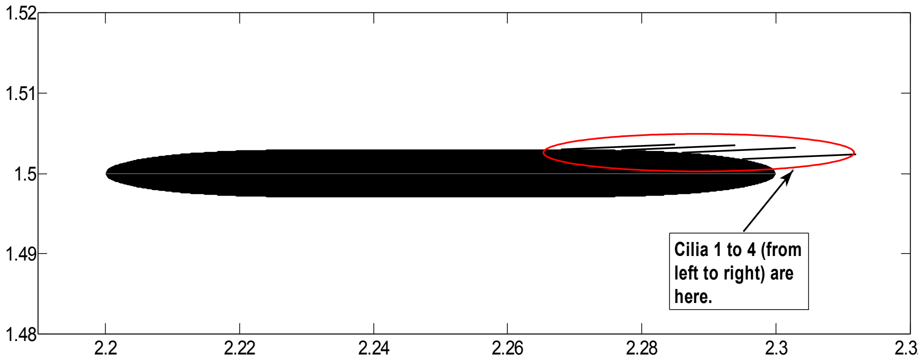

Figure 5.1: Placement of the poro-elastic layer on the horizontal flat plate, depicted by the reference feathers (shown here by the horizontal, black lines towards the end of the top side of the flat plate).

Figures 5.2 and 5.3, respectively, compare the time evolutions of the streamwise velocity at four streamwise locations over this flat plate and in its near wake, in the cases when it does and does not have a poro-elastic coating, and the time evolution of the streamlines over the coated flat plate, at four time instants spread evenly over one cycle of the time evolution of the lift coefficient (shown in figure 5.5).

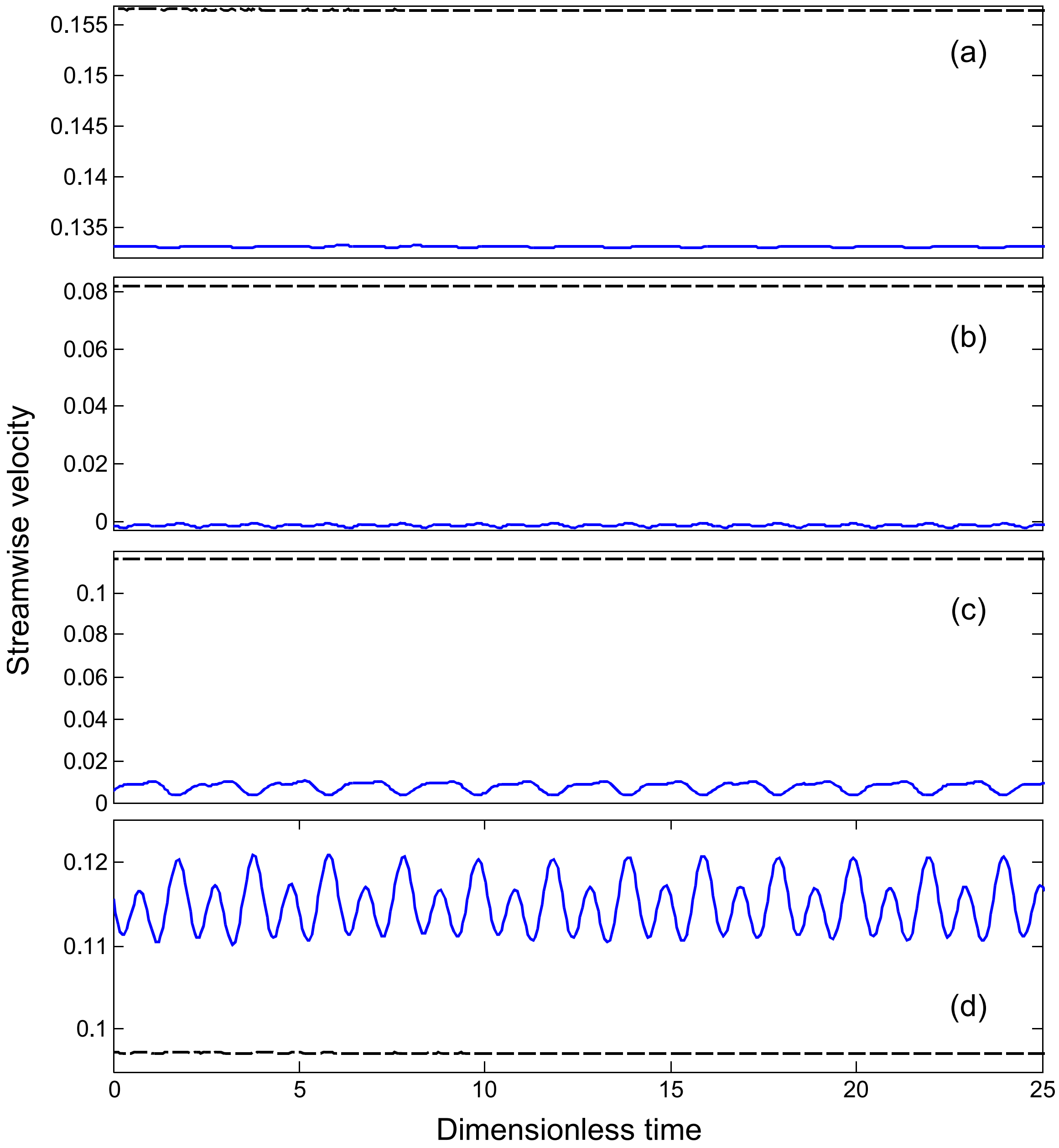

Figure 5.2: Comparison of the time evolutions of the streamwise velocity for the horizontal flat plate without (black, dotted lines) and with (blue, solid lines) a poro-elastic coating on its top side (as shown in figure 5.1), at four streamwise locations over the flat plate and in its near wake, going from left to right.

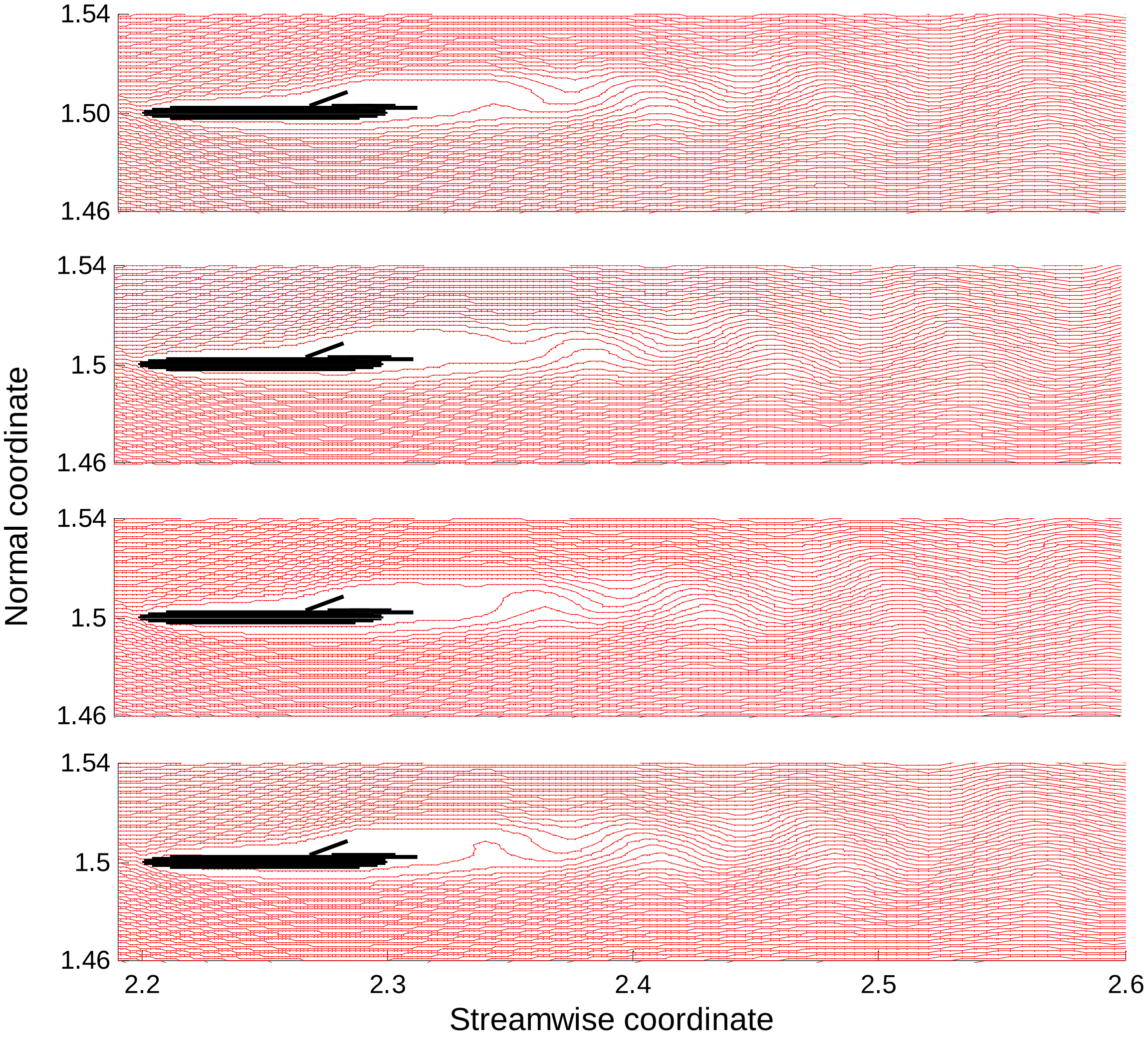

Figure 5.3: Snapshots showing the time evolution of streamlines close to the coated flat plate, as shown by the schematic in figure 5.1. These four time instants are selected uniformly over one cycle of the time signal of lift coefficient.

Figure 5.4 shows a snapshot of the vortex-shedding from the flat plate, introduced by the poro-elastic coating.

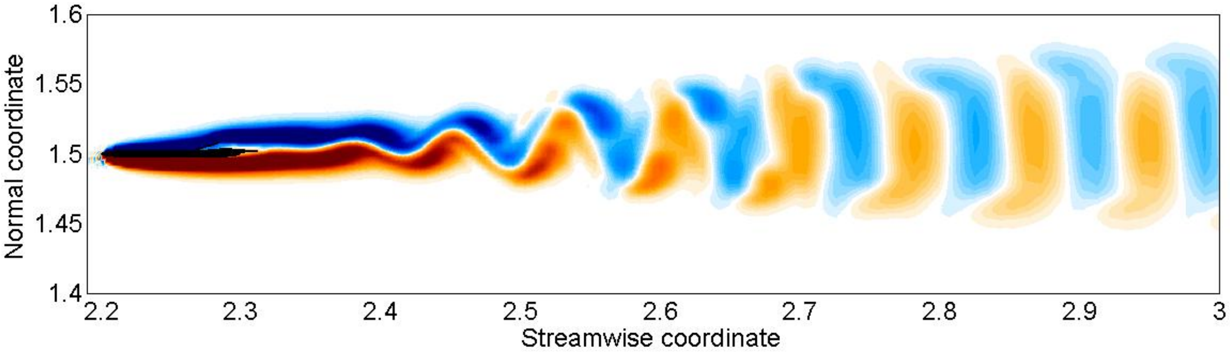

Figure 5.4: Colour plot of instantaneous vortex-shedding from the poro-elastically coated horizontal flat plate, shown in figure 5.1.

Figure 5.5 shows the dynamics of the lift coefficient for this poro-elastically coated flat plate, while figure 5.6 shows the dynamics of the four reference feathers that approximate the dynamics of the coating. Both these figures are shown in the time as well as frequency domains.

From the top sub-figure of figure 5.5, it can be clearly seen that the poro-elastic coating introduces some periodicity in the flow and makes the flow unsteady, by triggering vortex-shedding (as also shown in figures 5.3 and 5.4). From the bottom sub-figure of figure 5.5, it can be seen that the Fourier spectrum has a *unique* fundamental frequency (coinciding with the frequency of vortex-shedding) equal to 0.4947 along with all its super-harmonics.

From the top sub-figure of figure 5.6, it can be seen that the first reference feather (which is closest to the leading edge) has some oscillatory dynamics, while the other three reference feathers are always aligned with the free-stream (which is also set as the initial condition for the angular dynamics of the reference feathers, while running the simulations). Further, from the bottom sub-figure of figure 5.6, it can be seen that the frequency distribution exactly concurs with that shown in figure 5.5. Thus the fluid and the structure parts oscillate with exactly the same frequency equal to 0.4947, which is slightly modified from the inherent structural frequency equal to 0.4594, as calculated before figure 5.1. Hence, the dynamics of the structure part dictates the dynamics this coupled fluid-structure system, for the flow

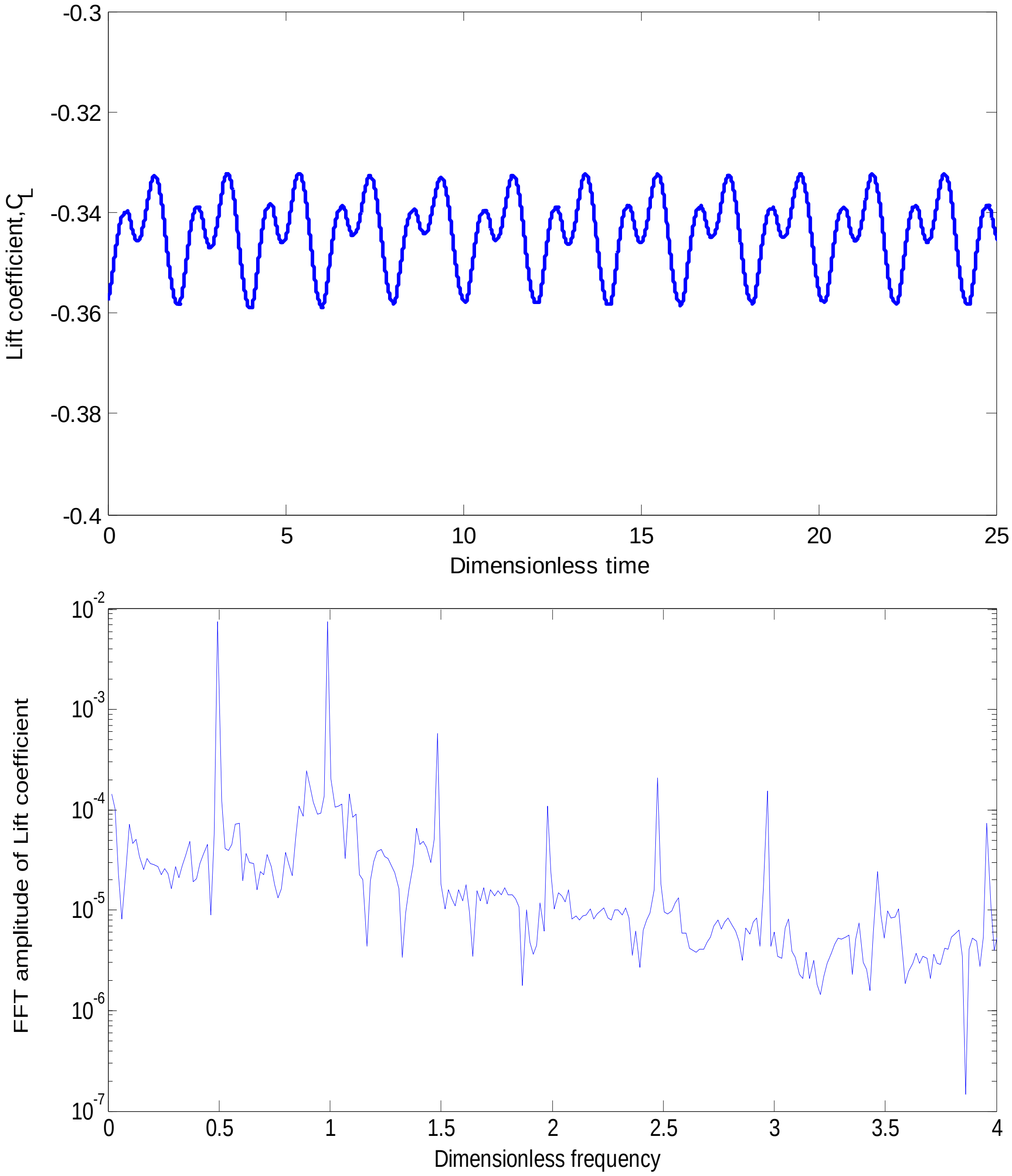

Figure 5.5: (Top) Time evolution of the lift coefficient for the horizontal flat plate with a poro-elastic coating on its top side (as shown in figure 5.1); (bottom) Fourier spectrum of the lift coefficient shown in the top sub-figure.

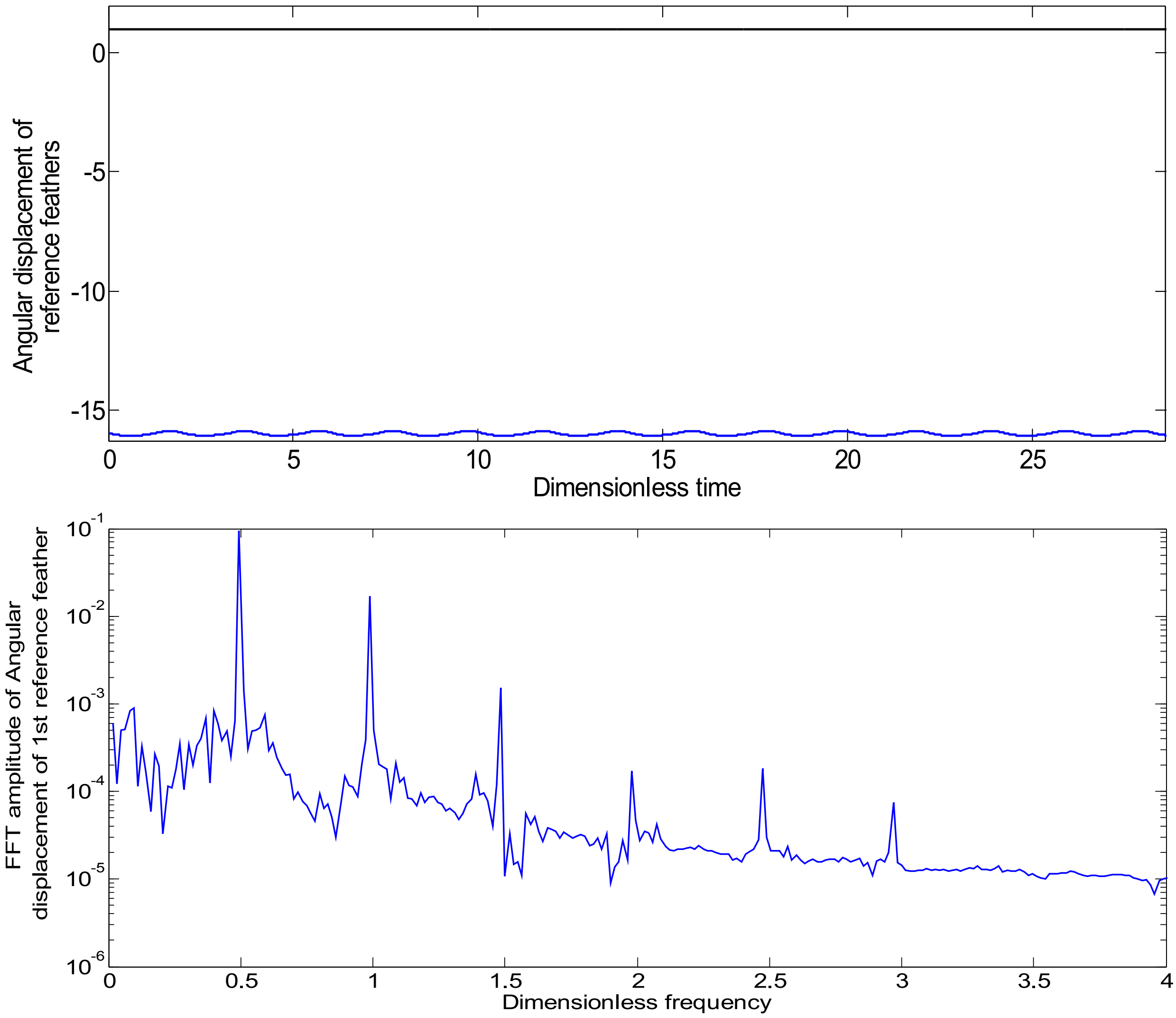

Figure 5.6: (Top) Time evolution of the angular displacement of the reference feathers, corresponding to the case shown in figure 5.5. The blue curve shows the dynamics of cilium 1 while the black curve shows the dynamics of cilia 2, 3, and 4 (as shown in figure 5.1), all of which are seen to be identical; (bottom) Fourier spectrum of the angular displacement of cilium 1.

over a flat plate aligned with the free-stream.

Case B: Flat plate oriented at an angle to the free-stream

Progressing from the simple case of considering the flow over a flat plate (without a coating), a more complex configuration is considered by analysing the flow over a flat plate oriented at an angle to the free-stream. In the present case, the angle of incidence is taken to be 10°. The four sub-figures of figure 5.7 show a comparison of the dynamics of the streamwise velocity at four streamwise locations over this flat plate and in its near wake, without and with coating. The top and bottom sub-figures of figure 5.8 show a comparison of the dynamics of the lift coefficient for this flat plate without and with coating, both in the time as well as frequency domains.

From the black curve in the bottom sub-figure of figure 5.8, it can be seen that the Fourier spectrum has a *unique* fundamental frequency (coinciding with the frequency of vortex-shedding) equal to 0.7831, along with all its super-harmonics. This frequency is unambiguously associated inherently with the characteristics of the flow over the flat plate. Now when this flat plate is coated with a poro-elastic layer (with exactly the same physical and structural parameters as for the case of the horizontal flat plate), it can be seen from the top sub-figure of figure 5.8 as well as figure 5.9, by comparing the blue curve with the black curve, that the lift oscillations have substantially decreased. This can also be seen from the amplitude of the fundamental frequency, as shown by comparing the blue and black curves in the bottom sub-figure of figure 5.8. Further, by analysing the blue curve here, one sees that there is a *unique* fundamental frequency, now equal to 0.7767, along with all its super-harmonics. This frequency is a modification of the frequency equal to 0.7831, obtained from the case of the tilted flat plate without coating. This frequency modification is probably the result of some energy dissipation arising from damping introduced by the coating, analogous to the frequency modification arising due to the linear damping term in

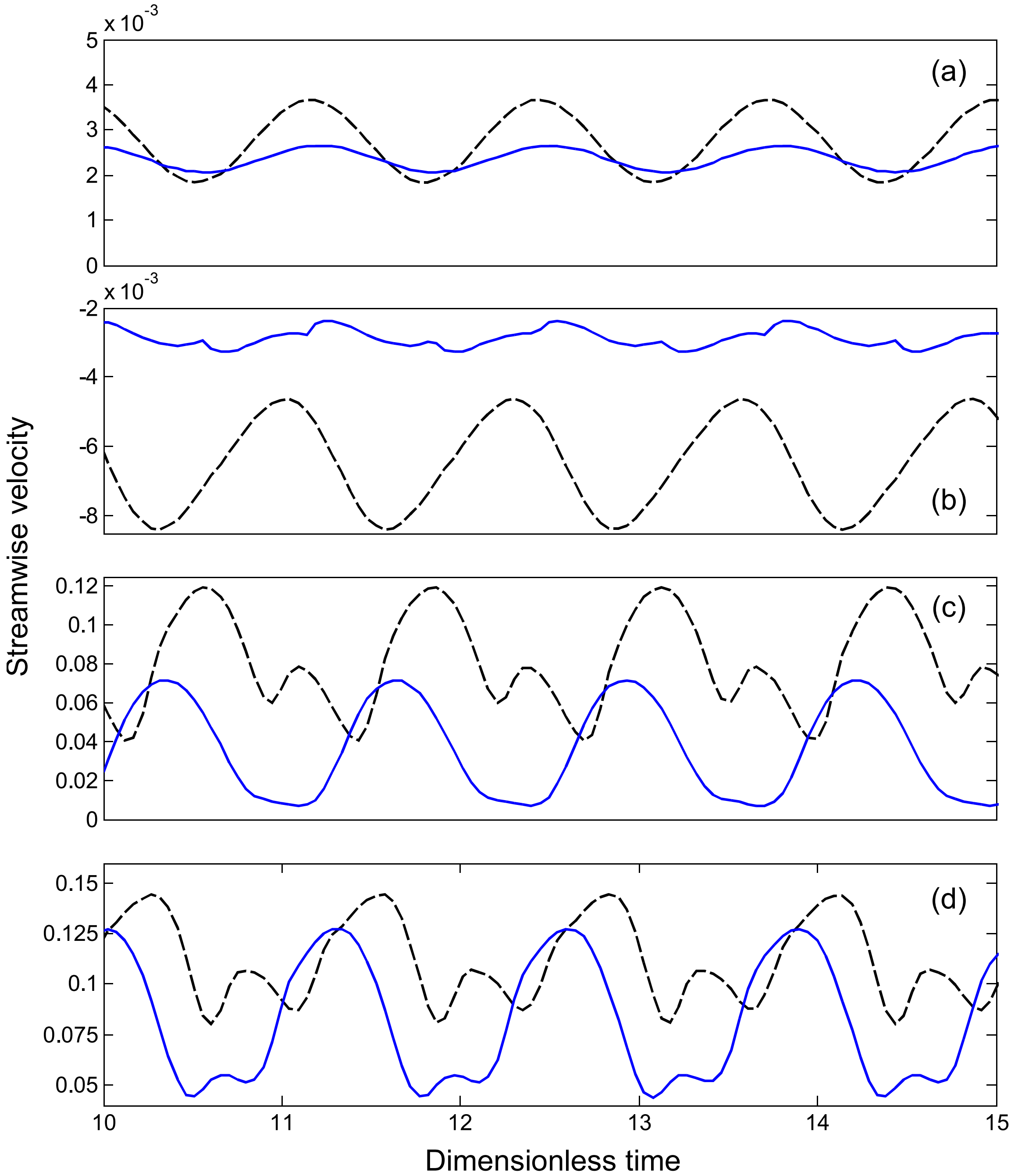

Figure 5.7: Comparison of the time evolutions of the streamwise velocity for the flat plate at an incidence of 10° without (black, dotted lines) and with (blue, solid lines) a poro-elastic coating over the end of its top side, at four streamwise locations over the flat plate and in its near wake, going from left to right.

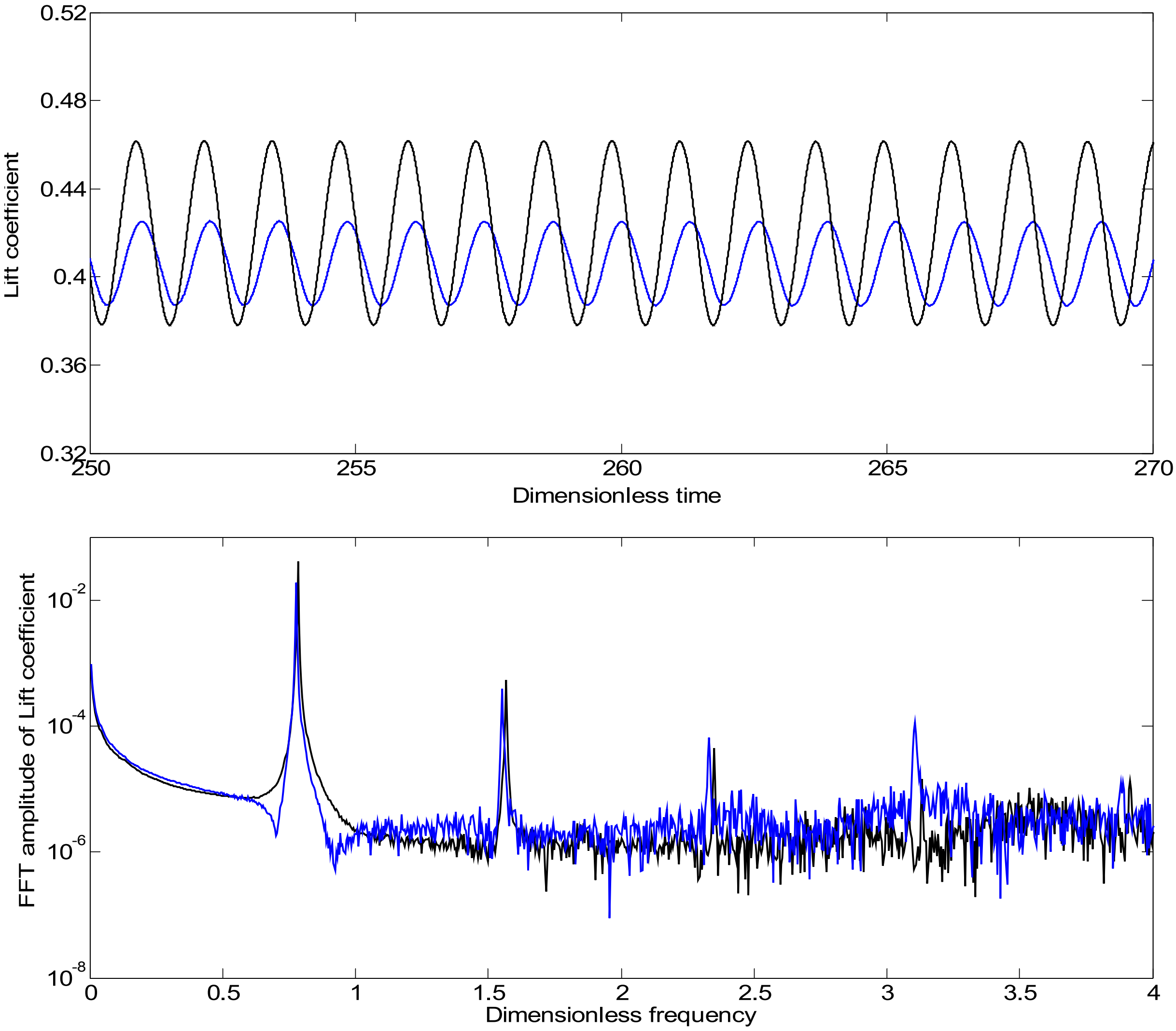

Figure 5.8: (Top) Comparison of the time evolutions of the lift coefficient for the flat plate at an incidence of 10° without (black curve), and with (blue curve), a poro-elastic coating over the end of its top side; (bottom) comparison of the Fourier spectra of the lift coefficients shown in the top sub-figure - the colour codes are same as for the top sub-figure.

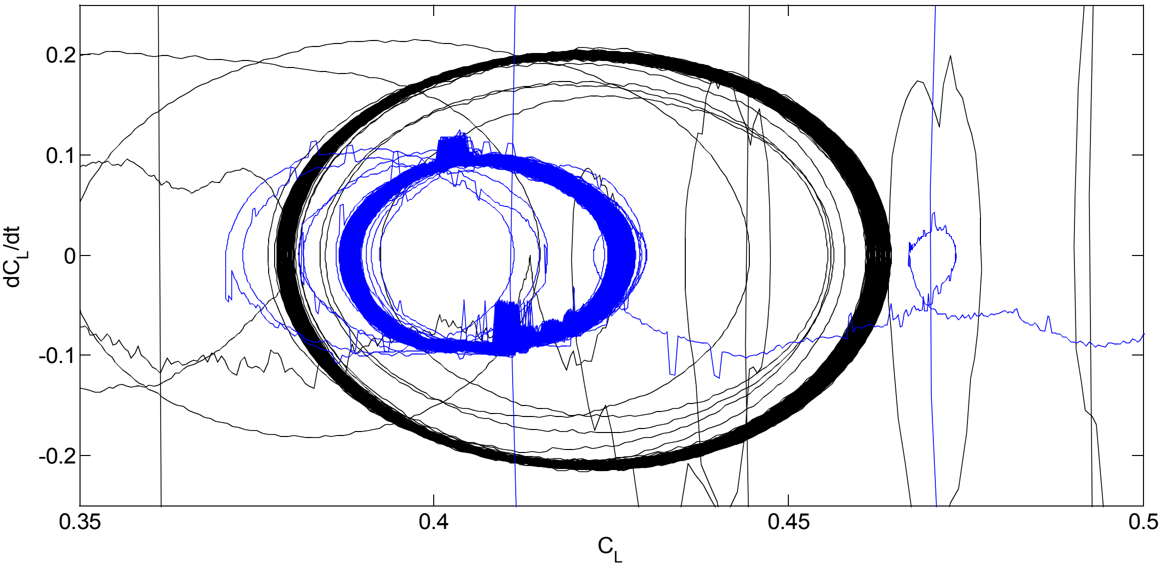

Figure 5.9: Comparison of the limit cycles for the lift coefficient for the flat plate at an incidence of 10° without (black curve), and with (blue curve), a poro-elastic coating over the end of its top side.

a single degree-of-freedom linear harmonic oscillator.

Figure 5.10 shows the dynamics of the four reference feathers approximating the coating, both in the time and frequency domains. From the top sub-figure of figure 5.10, it can be seen that the dynamics of the reference feathers become progressively more violent (that is, more oscillatory in nature) as they approach the end of the top side of the flat plate. This can also be seen from the bottom sub-figure of figure 5.10, which shows the frequency distribution of these angular dynamics. Further, in each of the cases of the four reference feathers, sharp amplitude peaks can be seen at values of 0.7767, followed by smaller peaks at its super-harmonics. This is exactly the same frequency obtained from the Fourier spectrum of the lift coefficient, shown in figure 5.8. Hence, the coating is possibly not strong enough in this case, to influence the dynamics of the coupled fluid-structure interactive system. In other words, the dynamics of this coupled system is governed by that of the fluid part.

That the fluid component governs the dynamics of the coupled system need not always be the case. The magnitude of the effect can vary, essentially with the characteristics of

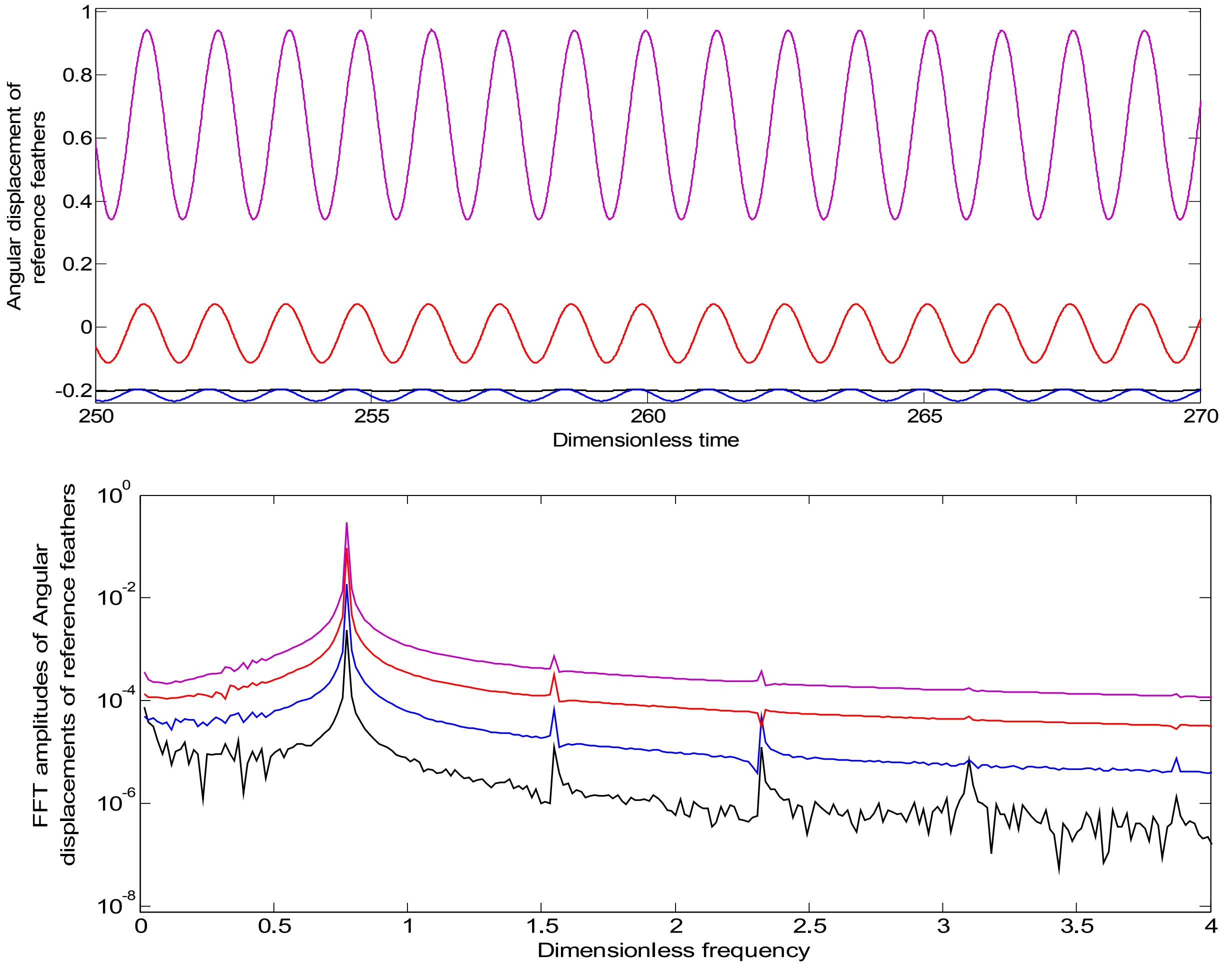

Figure 5.10: (Top) Time evolution of the angular displacement of the reference feathers, corresponding to the case shown in figure 5.8. The black, blue, red and pink curves show the dynamics of cilium 1, 2, 3 and 4, respectively; (bottom) Fourier spectra of the angular displacement of the reference feathers, shown in the top sub-figure - the colour codes are same as for the top sub-figure.

the coating. However, the case considered in the present section gives useful insight into how structure parameters can be selected to modify the dynamics of the coupled system in the ways it is desired. As will be outlined in the next sub-section, which presents results for a poro-elastically coated aerofoil, the influence of the coating can be strong enough to show its presence in both the frequency spectra of the lift coefficient as well as the angular dynamics of the reference feathers (i.e, the dynamics of the fluid part and the structure part), an instance of this being the presence of damped peaks corresponding to the structure frequency.

5.3.2 Case of symmetric aerofoil

Various simulations were performed for a poro-elastically coated aerofoil at 10° angle of incidence to the free-stream, with different structural as well as physical parameters (such as the rigidity frequency, the length of reference cilia, the placement of the coating on the aerofoil etc, as explained in chapter 2). An illustration of the effectiveness of the poro-elastic coating is shown in figure 5.11, where a noteworthy reduction in lift fluctuations can be seen.

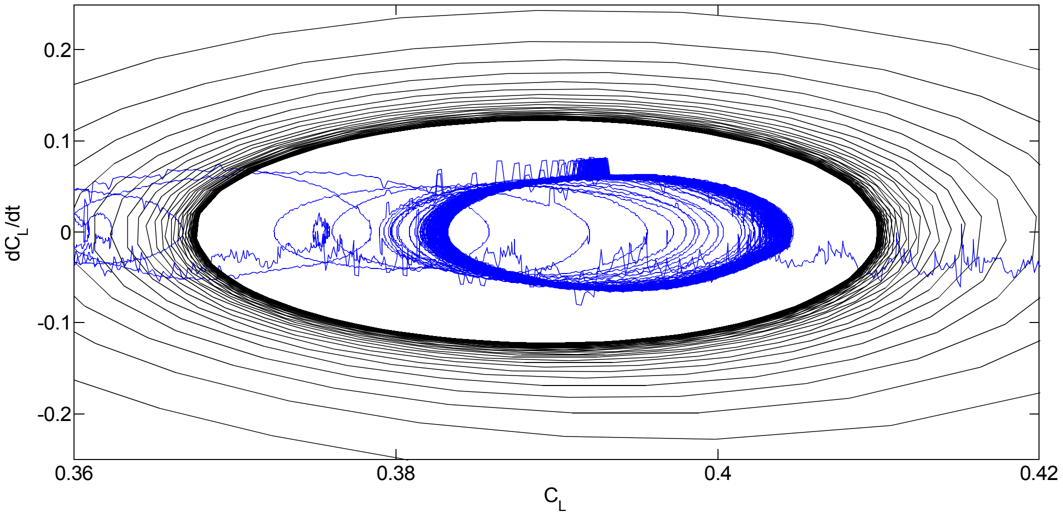

Figure 5.11: Comparison of the limit cycles for the lift coefficient for the aerofoil at an incidence of 10° without (black curve), and with (blue curve), a poro-elastic coating on its top side.

It was observed that in none of these cases, the dynamics of either the fluid or the structure systems (as captured by the quantities $C_L(t)$ and $\theta(t)$) exhibited the characteristics shown in case 2 (as explained in the §5.1). In other words, in none of these cases, the Fourier decomposition of the dynamics showed exactly one frequency $\omega_{s,2}$ without any super-harmonics. Further, all these simulations could be classified into cases 1 and 3 of §5.1. That is, either the case was where the dynamics of the fluid system showed a fundamental frequency $\omega_{s,1}$ and its super-harmonics and the structure system showed the *same* fundamental frequency (such as the coated flat plate case presented in the previous sub-section), or the dynamics of *both* the fluid and structure systems showed two unrelated frequencies $\omega_{s,1}$ and $\omega_{s,2}$ along with super-harmonics of the frequency $\omega_{s,1}$.

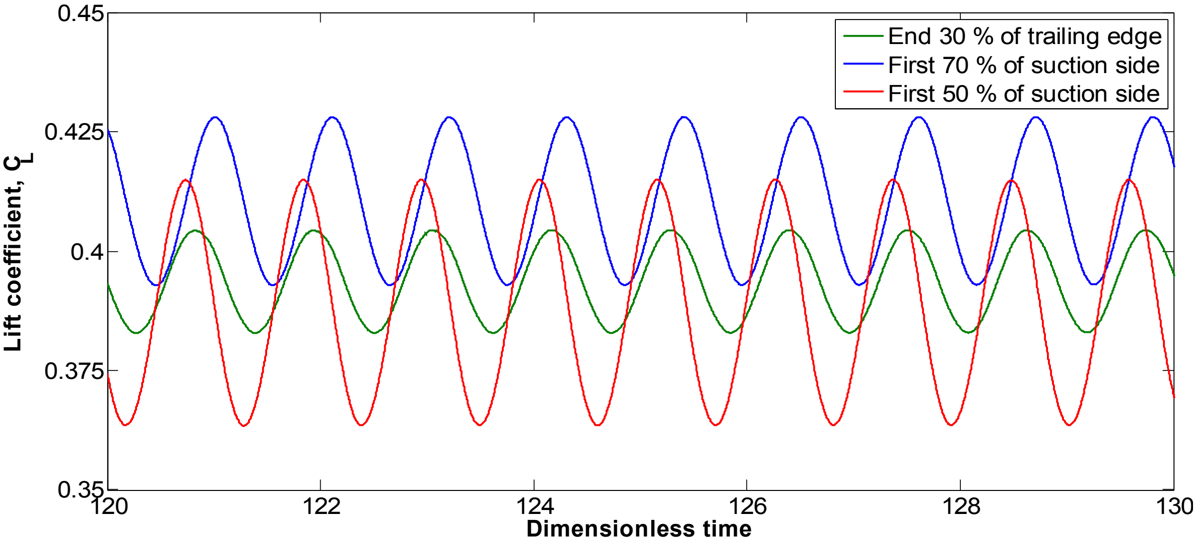

Figure 5.12: Time evolution of the lift coefficient for aerofoil at 10° angle of attack, with poro-elastic coating where the rigidity frequency ω_r is set equal to half the frequency of vortex-shedding, as shown in figure 4.2 (b). This figure shows three cases of placements of the poro-elastic layer on the suction side of the aerofoil: (a) last 30% of the suction side (green); (b) first 70% of the suction side (blue); and (c) first 50% of the suction side.

Figure 5.12 shows the steady-state time evolution of the lift coefficient of the aerofoil $C_L(t)$ for three cases of coatings, for each of which the rigidity frequency ω_r (which is also taken to be the dominant structure frequency, as explained in Chapter 2) is set equal to half of the fundamental frequency in the fluid system ω_f (which is in fact the frequency of vortex-shedding), as shown in figure 4.2 (b). Three cases of placements of the coating have been illustrated here, where the suction side is covered on the first 50%, the first 70%, and the end 30%.

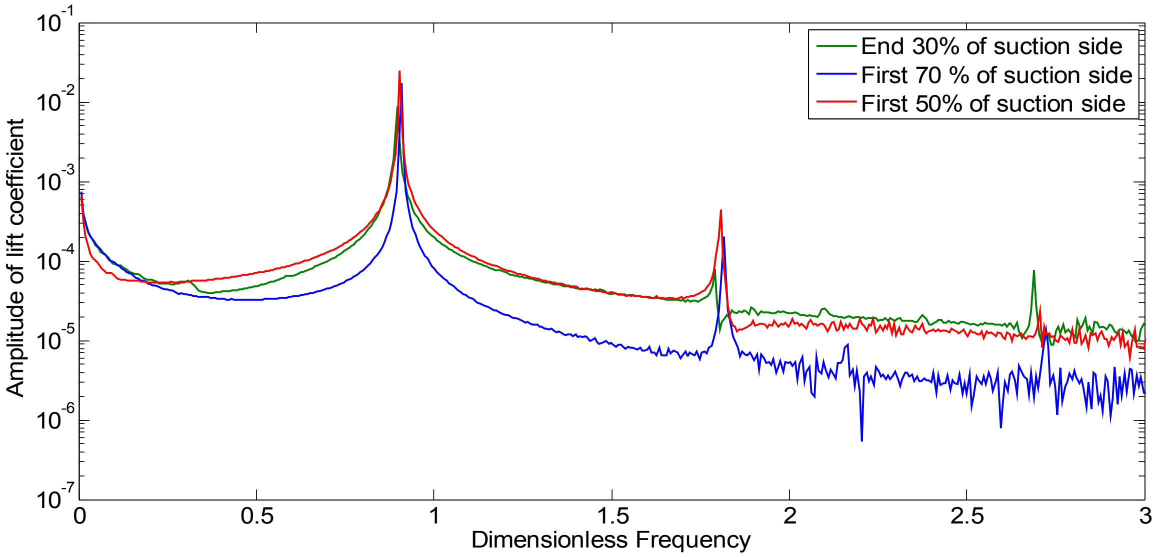

Figure 5.13: Fourier decomposition corresponding to the time signals shown in figure 5.12. This figure plots the amplitudes of the fundamental frequency and its super-harmonics for the coupled fluid-structure system.

Figure 5.13 shows the Fourier decomposition for these three cases. In each of these cases, a sharp peak at certain *unique* frequencies are seen, followed by peaks with amplitude of smaller magnitudes at twice and three times of these frequencies. In addition, for the case in which the end 30% of the aerofoil's suction side is poro-elastically coated (i.e, the green curve), a small *damped* frequency peak can also be seen at another frequency of value equal to 0.3087. Thus, in this case the coating is strong enough to show its presence in the coupled dynamics. Also, this case corresponds to case 3 (i.e, when the dissipation constant of the reference feather c is zero, and the lift has a non-zero steady-state amplitude), while the other two cases correspond to case 1 (i.e, when the reference feather has zero steady-state amplitude for its angular displacement, and the lift has a non-zero steady-state amplitude), both of these explained in detail in §5.1.

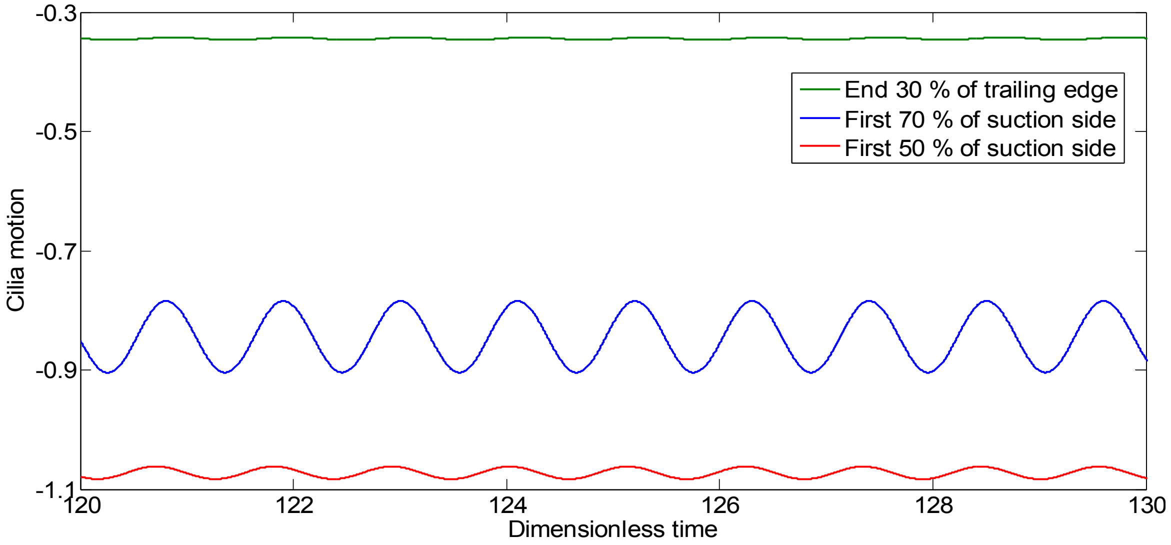

Figure 5.14: Time evolution of the angular displacement of a reference feather near to the middle of the suction side for the cases shown in figure 5.12.

Figures 5.14 and 5.16 show the steady-state time evolution of the angular displacement of a certain reference feather for the three cases of coating shown in figure 5.12. From figures 5.15 and 5.17, which show the Fourier decompositions of figures 5.14 and 5.16 respectively, it can be clearly seen (from the red curve) that, for this rigidity frequency, when the extent of the coating is only over the first half of the suction side (i.e, an area over which there is possibly not much interaction of the poro-elastic layer with the vortex-shedding from the trailing edge), the fluid and the structure systems oscillate at the same *unique* frequency $\omega_{s,1}$. However, when the extent of the coating either crosses or shifts to the later half of the suction side, then the dynamics of both the fluid and structure systems become progressively richer, with the appearance of new frequencies, such as the *damped* frequency peak $\omega_{s,2}$ of value equal to 0.3087, appearing due to the dynamics of the structure part and its coupling with the fluid part of the coupled system.

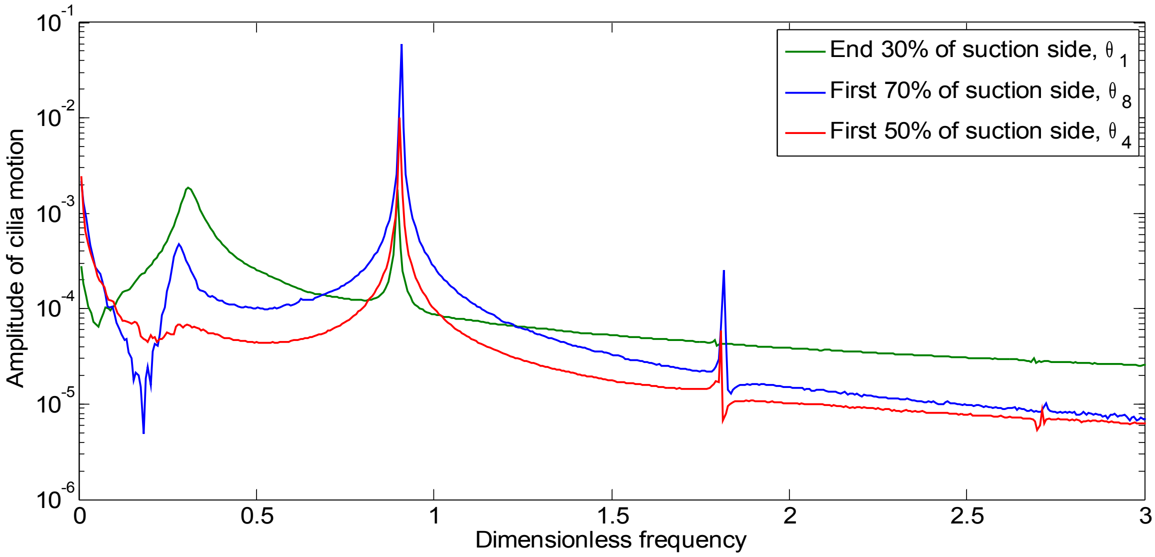

Figure 5.15: Fourier decomposition corresponding to the time signals shown in figure 5.14.

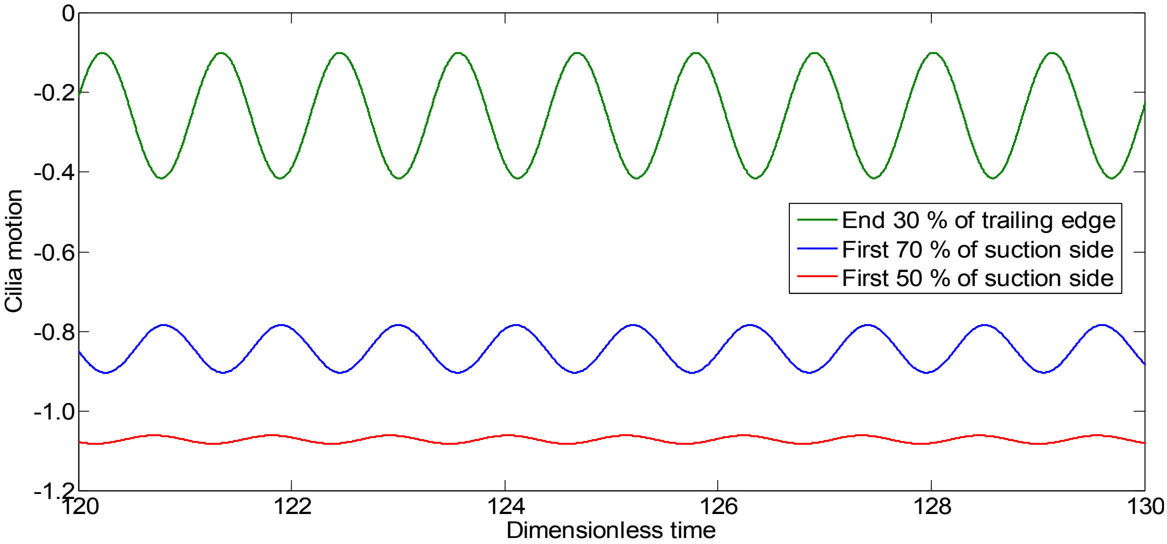

Figure 5.16: Time evolution of the angular displacement of a reference feather nearest to the trailing edge for the cases shown in figure 5.12.

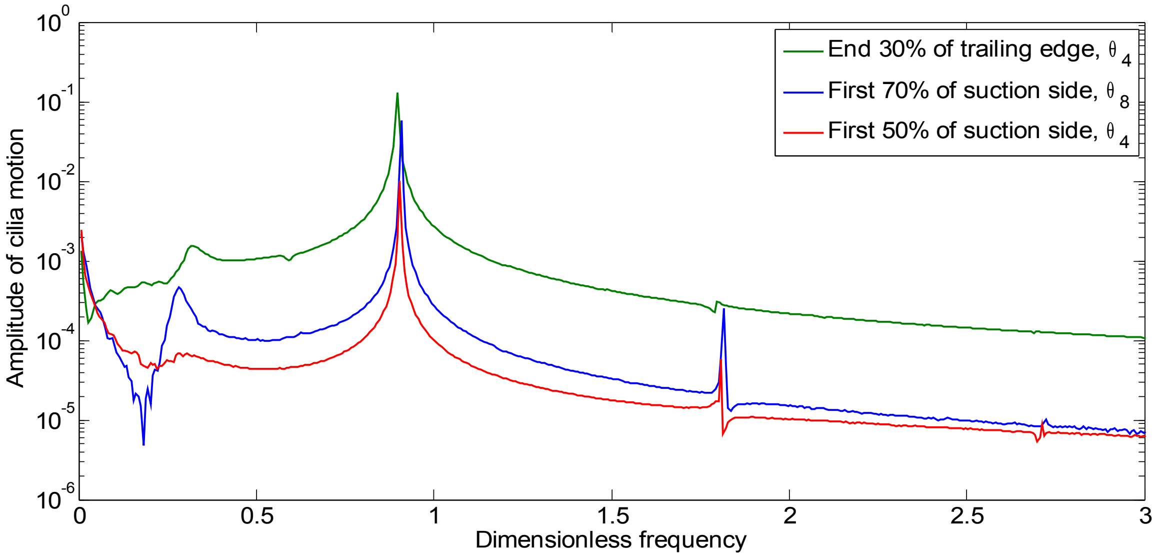

Figure 5.17: Fourier decomposition corresponding to the time signals shown in figure 5.16.

5.4 Comparison with simulation results

From all the simulations performed for the symmetric NACA0012 aerofoil with different characteristics of coating, super-harmonics of some fundamental frequency were seen at least in the time evolution of the lift coefficient. However, only in case 2 presented in section 5.1, it can be clearly seen that the closed-form solution for the lift coefficient does not exhibit any super-harmonics. Hence, for the derivation of the model parameters in terms of the characteristics of simulation results (just as it was done in §4.4.2 and §4.5), an illustrative case that corresponds with case 1 of section 5.1 is selected. In this case, the first half of the suction side of the aerofoil is poro-elastically coated, and various aspects of the simulation results are shown by the red curves in each of the figures 5.12 to 5.17. The position of the reference feathers on the aerofoil is shown in figure 5.18.

A snapshot of the instantaneous vortex-shedding, after it has reached its steady-state, is shown in figure 5.19.

It can be clearly seen from the red curve in figure 5.13 that, for the lift coefficient, after a peak at the fundamental frequency $\omega_{s,1}$ (which is also the *unique* frequency present in the

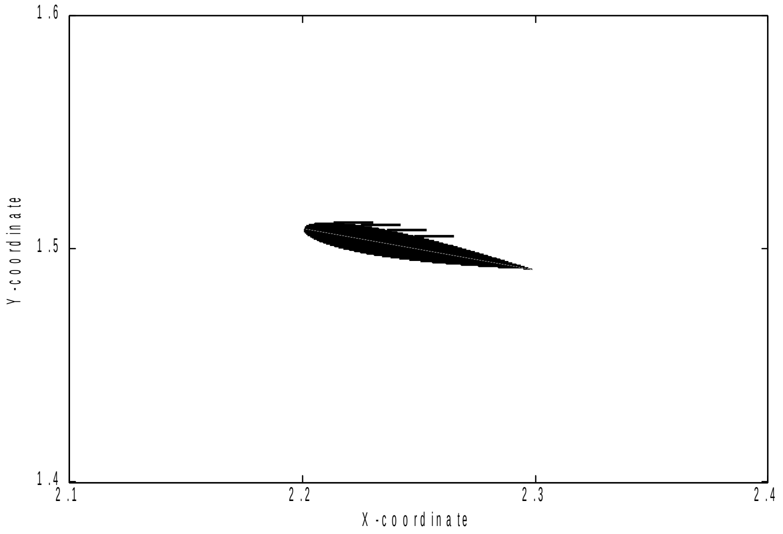

Figure 5.18: Placement of the poro-elastic layer on the aerofoil, depicted by the position of the reference feathers (shown here by the thick, black lines near the leading edge of the aerofoil).

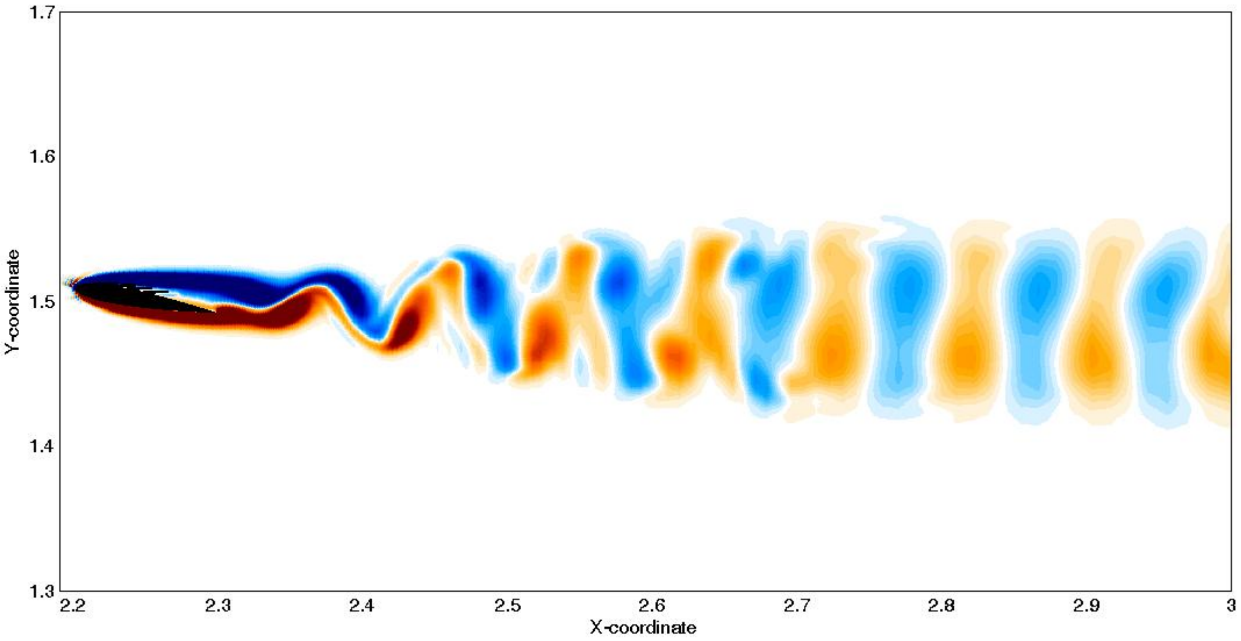

Figure 5.19: Colour plot of instantaneous vortex-shedding from a poro-elastically coated aerofoil at an incidence of 10°.

coupled system), there is a peak with substantial (but smaller) amplitude at $2\omega_{s,1}$ (followed by a further smaller peak at $3\omega_{s,1}$). Hence, as mentioned before, this figure shows a clear correspondence with case 1 explained in §5.1.

From figures 5.13 and 5.17, one gets the following values for the fundamental frequency $\omega_{s,1}$, amplitudes of the lift coefficient corresponding to the fundamental frequency and its second and third super-harmonics l_1, l_2 and l_3 respectively; and amplitude of the angular displacement of the reference feather (closest to the trailing edge) $\theta_1^{'}$ corresponding to the fundamental frequency:

$$\omega_{s,1} = 2\pi \times 0.9039 = 5.6794 \; ; \; l_1 = 0.0245 \; ; \; l_2 = 4.459 \times 10^{-4} \; ; \; l_3 = 8.123 \times 10^{-6} \; ; \; \theta_1^{'} = 0.01003 \tag{5.43}$$

Further, $\omega_{s,2}$, $l_1^{'}$ and θ_1 are all 0. Substituting these values in equations (3)-(10), we get the following values of the parameters for equations (5.2) and (5.3):

$$\omega = 5.6907 \; ; \; \delta\mu = 0.0453 \; ; \; \delta\alpha = 3.106 \; ; \; \delta\beta = 4.4571 \; ; \; \omega_1 = 0 \; ; \; \delta\rho_1 = 0 \; ; \; \delta\rho_2 = -13.255 \tag{5.44}$$

It must be recalled that for this case (which is in accordance with case 1 explained in §5.1), the dissipation constant c of the reference feather was allowed to be arbitrary, and hence can be taken to be arbitrarily large, in line with the physical consideration that the steady-state amplitude a_2 of the reference feather is zero. Thus, substituting the values obtained in equation (5.44) and by numerically solving it, we can compare this solution with the simulation results, as done in figure 5.20.

It can be seen that the simulation results and results from the model agree well with each other.

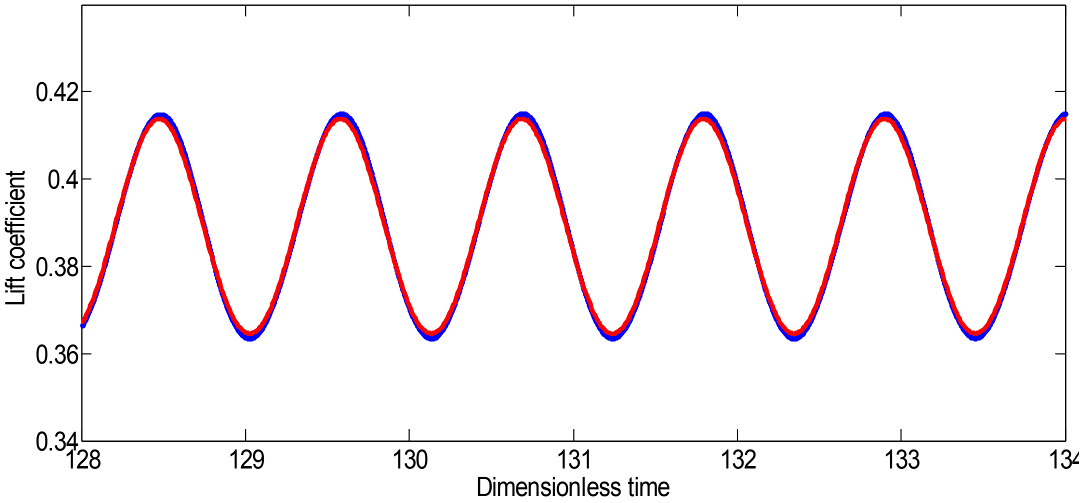

Figure 5.20: Comparison of model and simulation results of lift coefficient - the blue curve shows the simulation results while the red curve shows results from the model.

Further, figures 5.21 and 5.22 show two typical cases of initial conditions, outside and inside the (unique) limit cycle respectively.

It can be seen that in figure 5.21, beginning from a large initial condition far away from the limit cycle, the trajectory ultimately narrows and converges to the limit cycle.

In the case of figure 5.22, a small initial condition gradually expands and reaches the limit cycle as a steady state. Hence the steady-state solution is indeed independent of the initial conditions.

All of these results indicate the effectiveness of the reduced-order model for vortex-shedding behind a poro-elastically coated aerofoil.

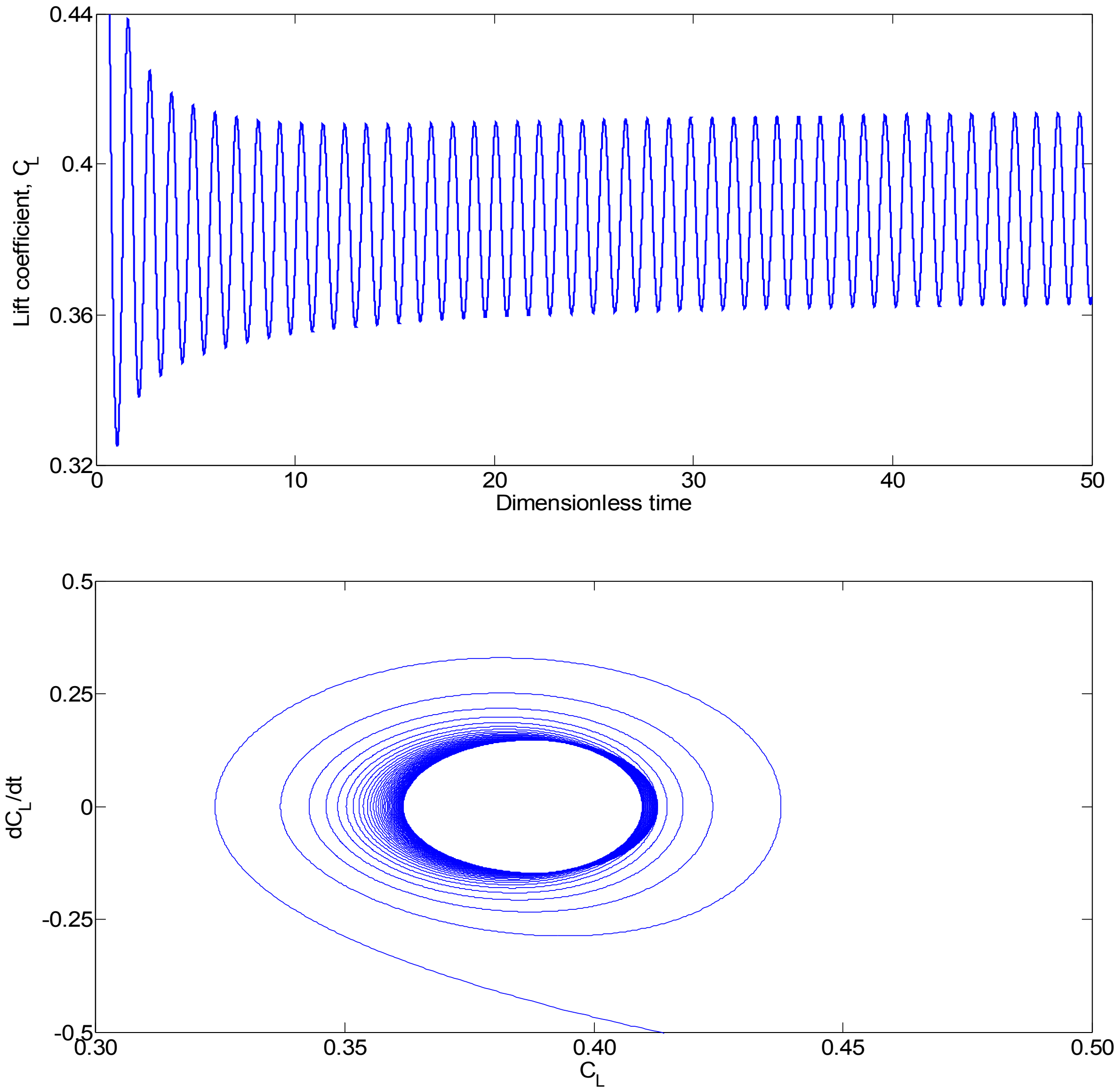

Figure 5.21: Convergence of numerical integration of the model equation from an initial condition **outside** the limit cycle. The top and bottom sub-figures show the time trace and the phase portrait, respectively.

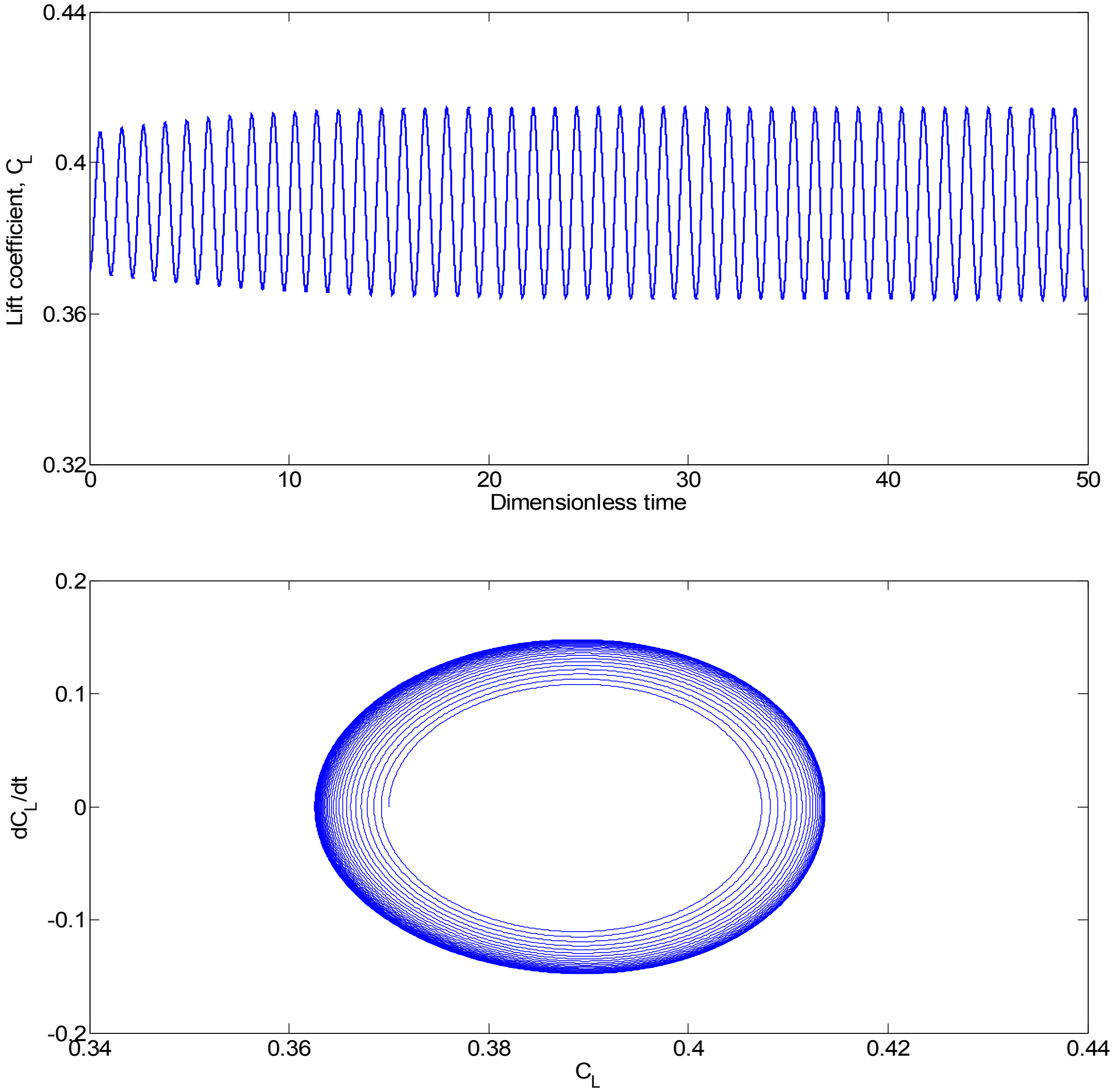

Figure 5.22: Convergence of numerical integration of the model equation from an initial condition **inside** the limit cycle. The top and bottom sub-figures show the time trace and the phase portrait, respectively.

5.5 Conclusions

A reduced-order model for vortex-shedding (investigated as before in terms of the unsteady lift coefficient) behind the aerofoil considered in Chapter 4, but now with a poro-elastic coating on a part of its suction side (such as the cases studied in Chapter 3), has been developed. To achieve this, the reduced-order model for the vortex-shedding behind a smooth aerofoil (obtained from Chapter 4) has been linearly coupled (with non-zero coupling coefficients for fluid-structure as well as structure-fluid interactions) with a linear damped oscillator for the dynamics of the reference feather.

For this coupled non-linear model for the lift coefficient, a closed-form expression for its limit cycle is derived in terms of generic (unknown) structure and coupling parameters (similar to such analysis done in Chapter 4). In the course of this analysis, three physical cases could be segregated based on the possibilities of whether the steady-state amplitudes of the lift coefficient and the angular displacement of the reference feather was non-zero or not, and various permutations of these possibilities. For each of these three cases, the expressions for model parameters in terms of the computational features were derived. These closed-form expressions also give insight into possible selection of structure and coupling parameters that are capable of yielding, for instance, reduced lift fluctuations, as compared to the case of the smooth aerofoil.

Many simulation results for coated aerofoils, with different extents and placements of coating over the suction side, has been presented. All of these simulations are seen to fall in one of the two cases of possible values for steady-state amplitudes. Based on this observation, the various characteristics of the periodic solution obtained from simulations are compared with the corresponding characteristics of the closed-form solution for the limit cycle obtained from the reduced-order model. From this, the structure and coupling parameters, that yield matching of trajectories obtained from the model and simulations, are determined.

All of the above observations indicate the effectiveness of the reduced-order model.

Chapter 6

Summary and Conclusions

This thesis has investigated the effects of a poro-elastic coating on the flow around a configuration, in particular, that of a symmetric aerofoil at an angle of attack. Specifically, extensive computational studies have been performed to see what structural characteristics of such a flow-compliant coating affect the flow topology, vis-a-vis, the process of vortex-shedding and the modification of the pressure field on the side on which coating is present. Next, based on the analysis of the simulation results for the vortex-shedding process for aerofoils, both without as well as with poro-elastic coatings, reduced-order models have been developed that:

(a) capture the key characteristics of results obtained from simulations;

(b) indicate optimal structure as well as fluid-structure interaction parameters that can yield desired modifications in the aerodynamic performance; and

(c) illustrate what parameters should never be selected while practically designing such a coating.

The following sections summarise the specific contributions of this thesis and provide several directions for future work.

6.1 Conclusions

Chapters 2 and 3, respectively, describe the computational method for studying the fluid-structure interaction problem in this thesis, by means of the immersed boundary method, followed by a presentation of the results of the computational parametric studies. Chapters 4 and 5 present the reduced-order models for the vortex-shedding behind aerofoils, both without as well as with the poroelastic coating, respectively. Specific conclusions and recommendations are listed below.

6.1.1 Numerical modeling of flow control via a porous, compliant coating

Flow control using passive actuators, such as in the present case of using a porous flow-compliant coating, or more traditionally of isolated self-actuated movable flaps at optimal streamwise locations, has been a viable alternative to active flow control techniques. This is especially true for MAV-based applications, where due to severe size and payload constraints, as well as the characteristics of low Reynolds number flow regimes, passive flow control is a very promising idea. This has been proved in Chapter 3 by means of extensive computational parametric studies, where it is shown that such a coating, by means of synchronisation of oscillations of the structures onto a frequency comparable to the natural frequency of the fluid system, is able to:

(a) affect the topology of the flow in the proximity of the rear of the aerofoil, by adapting spontaneously to the separated flow;

(b) modify the vortex-shedding process and also positively influence the pressure distribution, hence changing the drag and lift forces as well as their fluctuations (applications of which include, for instance, delaying stall).

Specific instances of how much the mean drag and lift, along with their fluctuations, can be changed, and what selection of structural and physical parameters of the coating is capable of causing these changes, have been detailed.

6.1.2 Reduced-order modeling for laminar flow control via a porous coating of compliant actuators

Since the vortex-shedding phenomenon behind an aerofoil (smooth or coated) is non-linear in general, non-linear reduced-order models have been developed to capture the physics of this phenomenon. An important dynamics characteristic that has been captured by the models includes the occurence of super-harmonics of a fundamental frequency in the standalone fluid system or the coupled fluid-structure system. These models are capable of:

(a) reproducing the dynamics obtained by heavy computational procedures (for instance, such as the one explained in Chapters 2 and 3);

(b) predict "optimal" structure and coupling parameters that can modify the aerodynamic performance in desired ways.

However, since the structure part of the reduced-order model for the coupled system considered till now is linear, this model can be further improved by progressively introducing non-linear terms that can both capture as well as possibly predict richer dynamics, along with better approximations of optimal structure parameters.

6.2 Thesis Contributions

The problem of passive flow control is a field for which a rich body of literature exists, especially over the last decade or so (as surveyed in Chapters 1 and 2). However, a majority of these studies have been experimental in nature, and hence, due to limitations of experimental set-ups, restricted to Reynolds numbers of order 10,000 or more. Chapters 2 and 3 of this thesis have:

(a) *computationally* investigated the regime of low Reynolds number flows, suitable for MAV-based applications;

(b) employed the immersed boundary method for the complex configuration of an aerofoil, both smooth as well as with a porous compliant coating. The use of this method has been particularly found to be useful since a time-invariant Cartesian mesh, that is non-conformal with the shape of the aerofoil, has been employed for moving immersed boundaries (such as those of the reference feathers).

(c) established the fact that the vortex-shedding process and the pressure distribution over the aerofoil can be desirably modified by a synchronisation of the oscillations of the structures onto a frequency which is comparable to the natural frequency of the fluid system.

In chapters 4 and 5, non-linear reduced-order models have been developed for vortex-shedding behind complex configurations such as:

(a) smooth aerofoil making an angle with the free-stream; and

(b) two-way coupled fluid-structure interaction problem for the case of a poro-elastically coated aerofoil,

respectively - i.e, corresponding to the computational studies performed in Chapters 2 and 3. In both these chapters, model parameters have been determined so that the solutions of the reduced-order models match the simulation results. Further, attempts have been made to characterise optimal structure parameters for the porous layer as well as two-way fluid and structure coupling parameters, that for instance, yield decreased lift fluctuations.

6.3 Some Directions for Future Work

During the course of this research, the following problem areas were identified as potential topics for future work:

Computational model for poro-elastic layer

The computational parametric study in Chapter 3 for a porous, compliant coating of feathers is limited to approximating such a layer homogeneously by a certain number of **rigid** beams that can oscillate about their mean positions. An issue with using rigid beams is that, the poro-elastic layer can not be very thick, so that short **non-bending** beams can realistically approximate such a layer. Thus, moving in a direction towards more realistically modeling such a coating, the use of longer "bending" feathers can be explored.

The research in this thesis has been restricted to understanding the physics for static *symmetric* aerofoils in *laminar* flow conditions. Hence, possible extensions can be to:

(a) perform the study on more complex configurations such as asymmetric and/or heaving-pitching aerofoils.

(b) examine the effectiveness of such passive flow control actuators under turbulent conditions, in the context of controlling transition to turbulence - an area which has significant implications in the design of conventional aircrafts.

(c) add a third spatial component, in the context of point (b) above, to the existing two-dimensional computational model, since the Reynolds number will be much higher in turbulent regimes, as compared to what has been studied in this thesis.

Reduced-order model for vortex-shedding behind smooth and coated aerofoils

The reduced-order model for the poro-elastic layer is purely linear, and thus considers the case in which there is either no interaction between neighbouring reference feathers or all reference feathers have identical and synchronous dynamics. Further, the structure-fluid and fluid-structure coupling terms considered here are also linear. Hence, possible extensions can be to formulate progressively non-linear models for the structure and coupling parts, to more realistically approximate such a layer, and the computational model investigated in this thesis in particular.

The mathematical models developed in this research can provide practical insight for the design of passive flow control actuators for optimising aerodynamic performance. The details of the flow profile in the simplified geometry can be used to evaluate both lift enhancement and drag reduction and tailor optimal control. The technical as well as economic feasibility of such passive actuator technologies shows that these, within certain limitations, enable progress in technologies of particularly light-weight aerial applications (such as micro-aerial vehicles), that have serious payload restrictions.

References

1. M. Gad-el-Hak, *Flow Control: Passive, Active, and Reactive Flow Management* (Cambridge University Press, London, United Kingdom, 2000).

2. D.J. Pines and F. Bohorquez, “Challenges facing future micro-air-vehicle development,” AIAA J. Aircraft **43 (2)**, pp. 290-305 (2006).

3. D.W. Bechert, M. Bruse, W. Hage, and R. Meyer, “Biological surfaces and their technological application – laboratory and flight experiments on drag reduction and separation control,” AIAA paper no. 97-1960, 1997.

4. J.B. Anders, “Biomimetic flow control,” AIAA paper no. 2000-2543, 2000.

5. A.C. Carruthers, A.L.R. Thomas, and G.K. Taylor, “Automatic aeroelastic devices in the wings of a steppe eagle *Aquila nipalensis*,” J. Exp. Bio. **210**, pp. 4136-4149 (2007).

6. J.H. McMasters and M.L. Henderson, “Low speed single element airfoil synthesis,” Technical Soaring **2 (2)**, pp. 1-21 (1980).

7. Y. Lian and W. Shyy, “Laminar-turbulent transition of a low Reynolds number: Rigid or Flexible airfoil,” AIAA Journal **45 (7)**, pp. 1501-1513 (2007).

8. J.H.M. Fransson, A. Talamelli, L. Brandt, and C. Cossu, “Delaying transition to turbulence by a passive mechanism,” Phys. Rev. Lett. **96**, paper no. 064501 (2006).

9. D.W. Bechert, M. Bruse, W. Hage, and R. Meyer, “Fluid mechanics of biological surfaces and their technological application,” Naturwissenschaften **87(4)**, pp. 157-171 (2000).

10. O. Doaré, B. Moulia, and E. de Langre, “Effect of plant interaction on wind-induced crop motion,” Trans. ASME J. Biomech. Engng. **126**, pp. 146-151 (2004).

11. C. Py, E. de Langre, and B. Moulia, “A frequency lock-in mechanism in the interaction

between wind and crop canopies," J. Fluid Mech. **568**, pp. 425-449 (2006).

12. E. de Langre, "Effects of Wind on Plants," Ann. Rev. Fluid Mech. **40**, pp. 141-168 (2008).

13. R.D. Mehta, "Aerodynamics of Sports Balls," Ann. Rev. Fluid Mech. **17**, pp. 151-189 (1985).

14. P.W. Bearman and J.K. Harvey, "Golf ball aerodynamics," Aeronaut. Q. **27**, pp. 112-122 (1976).

15. R. Bannasch, E. Maier, J. Schoffer, M. Stache, and I. Rechenberg, "Drag reduction by slotted wing tips in soaring birds," J. Ornithology **135 (1)**, pp. 38-43 (1994).

16. C. Brücker, J. Spatz, and W. Schröder, "Feasibility study of wall shear stress imaging using microstructured surfaces with flexible micropillars," Exp. Fluids **39 (2)**, pp. 464-474 (2005).

17. J.U. Schlüter, "Lift enhancement at low Reynolds numbers using self-activated movable flaps," AIAA J. Aircraft **47 (1)**, pp. 348-351 (2009).

18. N.M. Bakhtian, H. Babinsky, A.L.R. Thomas, and G.K. Taylor, "The low Reynolds number aerodynamics of leading edge flaps," in *Proceedings of the 45th AIAA Aerospace Sciences Meeting and Exhibit, January 8-11 2007, Reno, NV* (published by AIAA, Reston, VA, 2007), ISBN: 978-1-56-347878-9, paper no. 2007-662 , pp. 8018-8030.

19. R. Meyer, W. Hage, D.W. Bechert, M. Schatz, T. Knacke, and F. Thiele, "Separation control by self-activated movable flaps," AIAA Journal **45(1)**, pp. 191-199 (2007).

20. C. Brücker, "Interaction of flexible surface hairs with near-wall turbulence," J. Phys.: Condens. Matter - special issue on Nano- and Microfluidics **23**, paper no. 184120 (2011).

21. D. Venkataraman and A. Bottaro, "Numerical modeling of flow control on a symmetric aerofoil via a porous, compliant coating," Phys. Fluids **24**, paper no. 093601 (2012).

22. D. Venkataraman and A. Bottaro, "Flow separation control on a NACA0012 airfoil via a porous, compliant coating," in *IFMBE Proceedings of the 6th World Congress on Biomechanics, August 1-6 2010, Singapore*, edited by C.T. Lim and J.C.H. Goh (Springer, 2010), volume **31 (1)**, ISBN-10: 3642145140, ISBN-13: 978-3-64-214514-8, pp. 52-55 (DOI: 10.1007/978-3-642-14515-5).

23. J. Favier, A. Dauptain, D. Basso, and A. Bottaro, “Passive separation control using a self-adaptive hairy coating,” J. Fluid Mech. **627**, pp. 451-483 (2009).

24. C.H. Bruneau and I. Mortazavi, “Numerical modelling and passive flow control using porous media,” Comput. & Fluids **37 (5)**, pp. 488-498 (2008).

25. S.M. Han, H. Benaroya, and T. Wei, “Dynamics of transversely vibrating beams using four engineering theories,” J. Sound & Vibr. **225 (5)**, pp. 935-988 (1998).

26. A. Roshko, “On the wake and drag of bluff bodies,” J. Aero. Sci. **22 (2)**, pp. 124-132 (1955).

27. R. Bishop and A. Hassan, “The lift and drag forces on a circular cylinder in flowing fluid,” Proc. R. Soc. London A **277**, pp. 32-50 (1964).

28. R. Hartlen and I. Currie, “Lift-oscillator model of vortex-induced vibration,” J. Engg. Mech. Div. **96**, pp. 577-591 (1970).

29. I. Currie and D. Turnball, “Streamwise oscillations of cylinders near the critical Reynolds number,” J. Fluids Struct. **1 (2)**, pp 185-196 (1987).

30. R. Skop and O. Griffin, “A model for the vortex-excited resonant response of bluff cylinders,” J. Sound Vib. **27 (2)**, pp. 225-233 (1973).

31. W. Iwan and R. Blevins, “A model for vortex-induced oscillation of structures,” ASME J. Appl. Mech. **41 (3)**, pp. 581-586 (1974).

32. A.H. Nayfeh, O.A. Marzouk, H.N. Arafat, and I. Akhtar, “Modeling the transient and steady-state flow over a stationary cylinder, ” in *Proceedings of the 20th ASME Biennial Conference on Mechanical Vibration and Noise, September 25-28 2005, Long Beach, CA* (published by ASME, NY, 2005), ISBN-10: 0-7918-4738-1, paper no. DETC2005-85376, pp. 1513-1523.

33. O.A. Marzouk, A.H. Nayfeh, H.N. Arafat, and I. Akhtar, “Modeling steady-state and transient forces on a cylinder,” J. Vib. Control, **13 (7)**, pp. 1065-1091 (2007).

34. R.H. Rand, *Lecture notes on non-linear vibrations*, available online at *http://www.tam.cornell.edu/randdocs.*

35. S.H. Strogatz, *Nonlinear dynamics and chaos* (Addison-Wesley, Reading, MA, 1994).

36. A.H. Nayfeh, *Perturbation Methods* (John Wiley and Sons, NY, 2000).

37. A.H. Nayfeh, F. Owis, and M.R. Hajj, “A model for the coupled lift and drag on a circular cylinder,” in *Proceedings of the 19th ASME Biennial Conference on Mechanical Vibration and Noise, September 2-6 2003, Chicago, IL* (published by ASME, NY, 2003), ISBN-10: 0-7918-3703-3, paper no. DETC2003/VIB-48455.

38. I. Akhtar, O.A. Marzouk, and A.H. Nayfeh, “A van der Pol-Duffing oscillator model of hydrodynamic forces on canonical structures,” ASME J. Comput. Nonlinear Dyn. **4**, paper no. 041006 (2009).

39. M. Van Dyke, *Perturbation methods in fluid mechanics* (Academic Press, NY, 1964).